Enabling Applications of Templated Nanowires

A THESIS
SUBMITTED TO THE FACULTY OF THE GRADUATE SCHOOL
OF THE UNIVERSITY OF MINNESOTA
BY

Allison Harpel

IN PARTIAL FULFILLMENT OF THE REQUIREMENTS
FOR THE DEGREE OF
DOCTOR OF PHILOSOPHY

Bethanie J. H. Stadler

February, 2026

Acknowledgements

First, I'd like to thank my advisor, Beth Stadler, for her patience and guidance during the last 5 years. Your aid in starting my career and advocating on my behalf after a rough 2020/2021 has been invaluable.

Thank you to my senior students, Joseph Um and Yicong Chen. Even though we did not overlap much in-person, the knowledge you shared with me was incredibly useful. To the current members of the Stadler group: Roman Kolisnyk, Pang-Hsiao Liu, Biazid Kabir Moghal, and Ant Afful. It has been a pleasure working alongside and getting to know you all. You have my best wishes for the future.

Thank you to Dr. Rhonda Franklin, as I learned a lot from our collaborations with you and your group. To the Franklin group members I have had the pleasure of working with - Md Toaha Anas, Alex Wege, Alexander Ulate, Yali Zhang, and Aditya Dave - I am grateful for the productive collaborations and the sometimes less productive, but good, conversation.

Now, on to some more personal notes: I'd like to thank my friends and community that I found here in Minnesota, Emma Pettit, Kristine Loh, Kyle Tien, Jonathan Nguyen, and Zach Cresswell. Craft nights and your company helped make Minneapolis a home. To the friends I found in undergrad: Alec Sanabria, Sam Zaug, Sarah Hua, Walt Panfil, Maddy Earhart, Piper Earhart, and Aidan McKnight. Your friendship and support - especially during the covid years - have been so valuable to me. I am thankful for my fellow GLU members, especially the bargaining committee. The work we did together hopefully made this place safer and more secure for current and future graduates. I met so many wonderful people, and knowing I was doing something useful was motivating during those times when experiments become tedious. Lastly, thank you to my sister, Jessica, who always has been my biggest supporter.

Dedication

This thesis is dedicated to Ms. Kristina Williams. I'm so grateful for all the effort you put into your students. Your mentorship and support for me when I was young has meant so much to me.

Abstract

Ferromagnetic nanowires have been proposed for a broad range of applications as their low dimension and high shape anisotropy introduces novel electrical and magnetic properties. However, in most application spaces, there are significant hurdles that must be addressed before nanowire-based solutions are viable technologies for industry. This work seeks to bridge some of this gap for three different nanowire applications. First, a method for the reliable integration of vertical, templated nanowires is developed and evaluated to determine the controllability, robustness, and applicability of the resulting anodized aluminum oxide films. Second, a nondestructive, ferromagnetic resonance based technique for characterization of templated nanowires is proposed and experimentally validated. This method is shown to be not only feasible, but comparatively advantageous, for the quantification of both saturation magnetization and fill factor, which may be used for quality control of templated magnetic nanowires. Lastly, nanowire coatings were screened and evaluated for stability in cryoprotective agent cocktails. The suspension of magnetic nanowires allows for further study into their use as efficient heaters for cryopreservation application. With templated nanowires as the core technology, this work addresses roadblocks in processing for electronic, magnetic, and biological applications.

Contents

List of Tables

List of Figures

Chapter 1

Introduction

Cylindrical nanowires (NWs) are nanoparticles characterized by their nanoscale diameters, high shape anisotropy, and smooth side walls. The shape of these wires yield useful magnetic and electronic properties. Because of this geometry, when made with ferromagntic materials, there is a strong magnetic shape anisotropy that gives preference to magnetization along the nanowire axis [3, 4], which is advantageous for applications where square hysteresis loops are needed. Additionally, the ability to tune coercivities simply through changes in the material and geometry of the wires [5, 6], provides adaptability. Electronically, the small size scale can be helpful to prevent eddy losses in high frequency applications. Due to their scale and tunability, NWs show promise for applications in a wide variety of environments and have been proposed for use in nanomedicine, magnetic memory, and radio frequency (RF) technologies [7, 8, 9, 10]. However, in many of these applications there are large knowledge gaps that make further development of these technologies either commercially risky or difficult experimentally. This works seeks to address some of the gaps that may inhibit NW from being a feasible commercial product.

The central technology used in this thesis are nanowires and nanowire arrays fabricated through template-assisted electrodeposition. In Chapter 2, the properties unique to nanowires are introduced, and the fabrication and characterization methods are described. Three different applications for nanowires are addressed. For each, the work reported here seeks to enable and improve the feasibility of NW devices in this space. First, in Chapter 3, a process for vertical integration of templated nanowires onto silicon substrates is developed and characterized. Additionally, applications such as embedded magnetic nanowires and vias for high frequency coplanar waveguides were explored. A majority of these results were published in 2022 [11], and expand the capabilities of templated nanowires in silicon-based electronic and magnetic devices. Then, Chapter 4 develops and experimentally verifies a nondestructive method to quantify both the fill factor and saturation magnetization of templated magnetic nanowire arrays. This work seeks to fulfill the need for quick, nondestructive quality control if an application using templated magnetic nanowires (MNWs) is to be scaled up. This work was initially published in 2025 [12], with some of the data also appearing in a different 2025 paper on MNW based ID tags [13]. Chapter 5 develops MNWs for use as efficient nanoheaters for rewarming in cryopreservation applications. Here, coating procedures are developed and evaluated for stability when used with different MNW materials and cryoprotective agents. Producing stable MNW solutions in the solvents used for cryopreservation is significant hurdle to expanding research into the use of MNWs as nanoheaters, which is addressed here. The manuscript containing this work is in preparation. Finally, Chapter 6 summarizes and concludes the contents of this thesis.

Chapter 2

Nanowires and Fabrication

2.1 Nanowires and Notable Properties

The core technology to this thesis is the nanowire, which can also be referred to as a 1D material. The 1D character means that two of the dimensions are at the nanoscale, and one at the micro-scale (or above). Here, we will fabricate cylindrical nanowires, which have the two nanoscale dimensions as the circular cross section, and the axis of the cylinder is the long dimension. Typically, nanowires have a shape anisotropy on the order of 1:1000, but shorter nanowires can be fabricated, sometimes dubbed nanobars, retaining much of the same properties as nanowires. The unique properties of nanowires compared to a bulk or higher dimensional material typically result from a high surface area to volume ratio, the high shape anisotropy, and for the lowest diameter nanowires, quantum confinement effects.

Because of low dimensionality, nanowires have increased surface energy compared to micro and macroscale metallic particles.This increased surface energy results in increased reactivity and potential for aggregation. The surface of metallic nanowires typically sport an oxidized layer less than 3 nm thick once released from a template [14]. This modified surface layer can depend on the release method used to liberate the nanowires from the template. The methods typically used in this work have been shown to produce an oxide layer in Ni, with hydroxide ions adsorbed to the surface [15]. This reactivity also enables surface modifications and coatings of the wire surface. The identity and thickness of the surface layer can effect the mechanical [16], electronic and magnetic [17, 18, 19] properties of the nanowires.

Mechanical properties of nanowires depend on defect density, surface character, crystallinity, and dimensions, so the exact parameters are unknown unless a sample is measured. In general, the fracture strength of a nanowire is significantly greater than that of the bulk [16]. This effect is expected to be due to the decreased number of defects present in the particle that arises simply from lowering the volume of material. This means that for the applications considered here, even when the nanowires are released from their templates, they are most likely to retain their shape and not break under normal conditions. However, the variation in properties with nanowire conditions means that fabrication conditions can change the mechanical behavior. One significant factor is that, depending on the fabrication method and conditions, nanowires can be single crystal or polycrystalline [7]. Nanowires fabricated and used in this work were made using template-assisted electrodeposition, and as a result were typically polycrystalline (as confirmed using x-ray diffraction) and had smooth sidewalls.

The nanowires used in this thesis are all composed of transition metals that display strongly metallic behavior in bulk. However, when the dimensions are reduced, the resistivity will typically increase due to surface effects or once the dimensions are reduced enough, due to quantum confinement effects [20]. Surface effects are increased in nanowires compared to larger structures due to the large surface area to volume ratio, which increases the likelihood of electron scatter off of the surface. Because of this dependence on surface area to volume ratio, as nanowire diameters decrease, the resistivity increases. The quality and roughness of the surface significantly impacts the resistivity of the wires: the rougher the surface, the more scattering occurs and the wires are less conductive. In most electronic devices the increased resistivity is a disadvantage, although sometimes a necessary one in order to fabricate small scale devices. For high frequency devices benefits from the small size scale can potentially outweigh the downsides. Compared to bulk, the small, isolated nanowires reduce losses that result from eddy currents induced by the alternating magnetic field. In devices such as transformer cores, this effect is produced by lamination of the core material [21]. For this reason, in Chapter 3 vertically integrated nanowires are explored as grounding vias for radio frequency devices.

In nanowires, one model for resistivity in cylindrical nanowires that takes into account the surface roughness and diameter is shown in Eq. 2.1 and is known as Fuchs-Sondheimer (or FS) theory [22, 23]. In FS theory, the intrinsic properties of the metal are considered with the bulk resistivity, ρ_o^*, and the path length of an electron in the metal, λ_e. The diameter, D, of a cylindrical nanowire is taken into account, and a scattering factor, p, is included. The scattering factor can range from zero to one, where zero is most diffuse or inelastic scatter, and one is a smooth surface with perfectly elastic scatter. In this model, the resistivity approaches the bulk value when the diameter is sufficiently large such that surface behavior is negligible or the surface is smooth such that elastic scattering takes place (and p approaches 1). The model works in general for nanowires, but it does not take into account changes to the density of states that occur when the diameter is low such that quantum confinement alters the density of states. For this work, nanowires lower than 20 nm were not fabricated or used, so the density of states is not expected to be significantly altered. The resistivity of NWs are estimated in Chapter 3, and this model provides a means to assess the validity of the results.

$$\rho = \rho_o^*[1 + 0.75 \cdot (1 - p)\lambda_e/D] \tag{2.1}$$

When nanowires are made of the ferromagnetic transition metals and their alloys, magnetic nanowires (MNWs) are produced. These wires maintain a net or remnant magnetization, even when no external magnetic field is applied. The defining characteristic of nanowires creates is the high shape anisotropy, and for magnetic materials this creates an energetically preferential direction of magnetization along the long axis of the nanowire when the shape anisotropy dominates over the crystalline anisotropy [3, 4]. This preferred magnetization direction is called the easy axis. Because the shape contributes significantly to the way the wire behaves, this means you can engineer the wires to have behavior that is desirable for your application. One way to characterize the magnetic behavior is by measuring the sample magnetization or magnetic moment as a function of the applied field. For ferromagnetic materials, this produces a hysteresis loop, the area of which is the energy lost during a full reversal cycle. A sample of a hysteresis loop is shown in Fig. 2.1a, where features such as the remnant magnetization (M_R), saturation magnetization (M_S), and the coercivity (H_C) are highlighted.

Fig. 2.1b summarizes the physical changes that can be made to tune the coercivity, saturation magnetization, and hysteresis loop squareness for a magnetic nanowire.

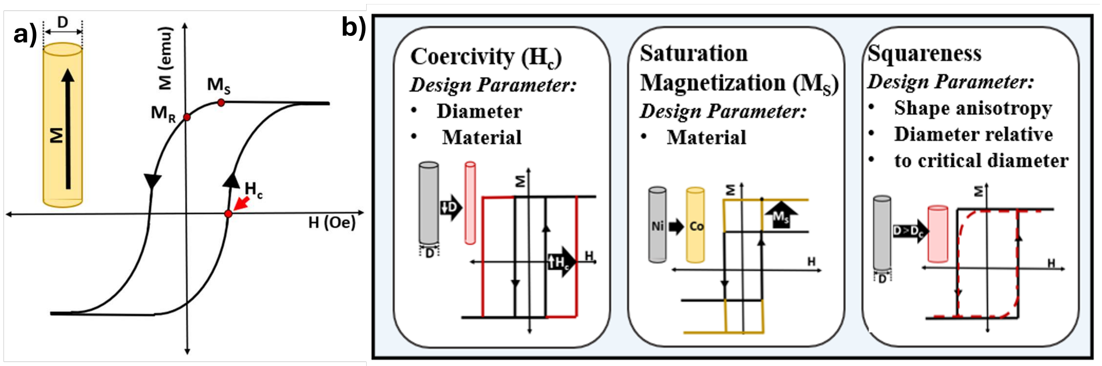

Figure 2.1: a) A sample hysteresis loop highlighting the coercivity (H_C), the saturation magnetization (M_S), and the remnant magnetization (M_R). b) A schematic highlights the design parameters for changing the hysteresis loop for MNWs

The coercivity (H_C), which is the applied field required to switch the magnetization direction of each nanowire, is one of the properties sensitive to the wire diameter [24, 25, 26]. There is an energy barrier to switching the magnetic moment. Much of this energy barrier is due to the demagnetization field, characterized by the tensor N, being much larger in the small dimension than the long axis. This demagnetization field gets larger as the diameter of the wire decreases [27]. As such, lower diameter wires must overcome larger energy barriers to switch magnetization directions than larger diameter wires or spherical nanoparticles. Additionally, different wire diameters have different switching mechanisms [28]. Under a critical diameter, typically around 20-40 nm, transverse domain walls form which lead to a large jump in the wire coercivity. This can change depending on surface quality of the nanowire, where roughness can pin domains, increasing the field required to switch. The change in coercivity with diameter and materials in one of the primary ways the behavior of a MNW can be tuned.

In addition to the diameter of the wire, by changing the metal or structure of the nanowire material, nanowires with different saturation magnetizations can be made. The wires discussed in this thesis are fabricated using electrodeposition, which means that different materials can be deposited, alloyed, or layered as long as a viable electrodeposition reaction has been developed. Sometimes the fabrication conditions or pore size can influence the NW structure, as the pH or confined pore size can introduce strain into the system, which can result in crystal structures not typically stable at room temperature [29]. In addition to the materials having different saturation magnetizations, the crystal structure and - if present - preferred grain orientation can introduce crystalline magnetic anisotropy to the wires. Depending on the direction of the crystalline anisotropy, this can either reinforce or detract from the influence the shape anisotropy of the wire has on the system. When measurements, such as ferromagnetic resonance, are taken, the introduction of anisotropy can influence the apparent saturation magnetization [30]. In general, electrodepositing different NW materials or alloying metals, wires with a range of saturation magnetizations can be produced.

When magnetic nanowires are in arrays the magnetic fields of the nanowires interact. Magnetic fields decay proportionally to r^3, where r is distance from the field source[31]. As such, the spacing of the nanowires has a strong impact on how much the wires' magnetic fields interact. It is more energetically stable to minimize the amount of stray fields required by a give orientation, so there is an energetic preference for adjacent wires to be pointing in opposite directions. When measuring the hysteresis loop of an array of nanowires, some wires switch at fields either lower or higher than their coercivity, depending on how much the surrounding wires are stabilizing the configuration [32]. This phenomena emerges as a shearing of the hysteresis loop. Magnetic interaction also occur when MNWs are freed from the template and solvated [33]. This can lead to particle aggregation and flocculation if the wires are not sufficiently well coated. Changing the density of the wires in an array or layering wires provides a way of tuning the squareness of the hysteresis loop.

2.2 Fabrication and Characterization Methods

2.2.1 Fabrication

Template-assisted electrodeposition was employed to fabricate all MNWs used in this work. This method is excellent for the fabrication of magnetic nanowires especially because it produces arrays of magnetic nanowires with excellent control over the most sensitive dimension - the NW diameter Bograchev. Template-assisted electrodeposition uses an electrolytic reaction, which is where you drive a typically non-spontaneous reaction by applying a voltage to the system [34]. For template-assisted electrodeposition, the electrolytic reaction is the deposition of a metal into the pores of a non-conductive template that has a conductive layer at the base. A typical reaction setup using a rotating disk electrode (RDE) is shown in Fig. 2.2a, where a template and an electrode are immersed in an electrolyte solution and, with the help of a reference electrode, the voltage between the electrode and template is controlled by a power supply or potentiostat. Fig. 2.2b shows a schematic of the RDE and location of the mounted template. Fig. 2.2c shows images of the top and cross section of an anodized aluminum oxide template that would be used for template-assisted electrodeposition. In an electrolytic reaction, if the applied voltage is above the standard reaction potential of the cell, the reaction should be driven. Generally, an overpotential is applied, which increases the rate of reaction to more practical values, but not to the extent where numerous side-reactions are enabled. In addition to the voltage, the reaction rate is influenced by the concentration of reactants in solution and the ability of the ions to get to the interface where the charge is transferred. In this way, the nanopores are infilled with deposited metals such as copper, nickel, cobalt, and iron, producing nanorods or nanowires.

The templates are critical to fabricating nanowires, because the pores control the geometry of the nanowires to which the magnetic and electrical properties are most sensitive. Typically, anodized aluminum oxide (AAO) or track-etched polycarbonate films are used as the templates, with a thin layer of metal sputtered or evaporated onto one side to act as an electrical contact. AAO templates are made using another electrolytic reaction converting aluminum to porous aluminum oxide. The reaction conditions, including which acid is used as the electrolyte [35] determines the pore diameter and density. Pores can be subsequently enlarged via etching. The diameter of pores commercially available or readily made range from 10-200 nm. Track-etched polycarbonate is fabricated by exposing polycarbonate films to an ion beam, and the pore density is determined by the exposure time. Pore sizes are determined by the subsequent etch step. The diameter of pores commercially available for track etched polycarbonate are generally within 50-1000 nm [36]. Notably, the pore density of the track-etched polycarbonate ($10^7 - 10^8\ cm^{-2}$ [36]) is typically much lower than in AAO

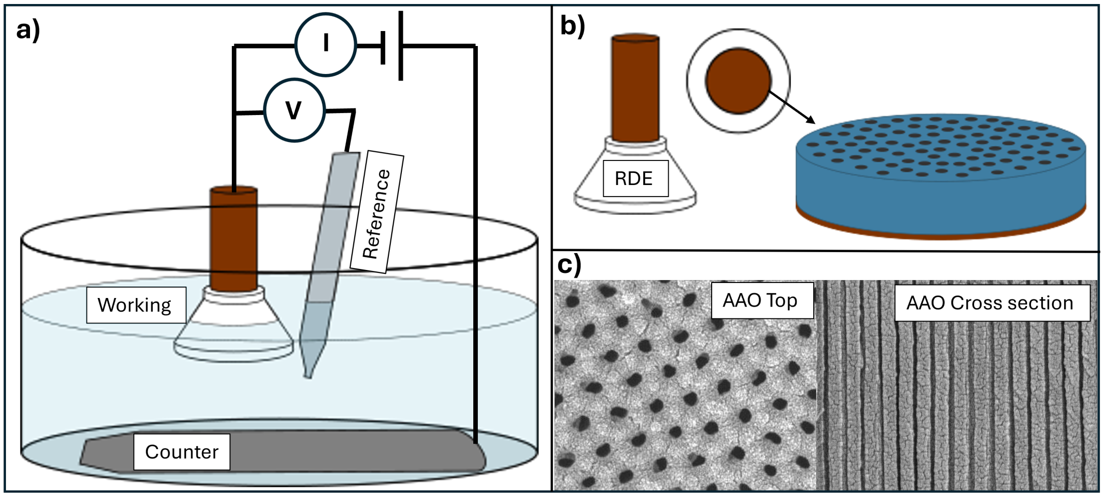

Figure 2.2: a) Schematic of setup for template assisted electrodeposition using a rotating disk electrode with the working, counter, and reference electrodes labeled and either the voltage or the current being controlled. b) A schematic of the rotating disk electrode (RDE) is shown with the anodized aluminum ozide (AAO) c) Images from the manufacturer (InRedox) of an AAO cross section and surface are shown.

($10^8 - 10^{12}$ cm^{-2}[37]) In this work, AAO templates were primarily used due to the high pore density which allows for the fabrication of more NWs at a time and its rigid nature which can make it easier to establish a stable, well-connected back contact during deposition. In Chapter 3, the AAO templates are fabricated as a layer integrated onto a silicon wafer. In Chapters 4 and 5, commercial AAO templates are backed and used to make nanowires.

The electrolyte controls the composition and the quality of the nanowires. Most electrolytes used here are primarily made from the sulfate salts of the metal to provide a source of metal ions, which are subsequently reduced to deposit the desired metal. A buffering agent, such as boric acid (H_3BO_3), is always added to stabilize the pH of the solution throughout deposition, while a strong acid, (H_2SO_4) and/or strong base (NaOH) is typically used to adjust the pH to the needed level. Sometimes, a surfactant such as sodium dodecyl sulfate (SDS) is used to reduce the surface tension and improve mobility of the aqueous solution into the pores [38]. This is especially relevant for pore diameters 20 nm and below in hydrophobic AAO templates. Sometimes, grain refiners, such as saccharin salts are used to reduce the stress in the deposited metal and make the grains smaller [38]. However, the use of grain refiners must be balanced with the magnetic properties desired in the final product, as the addition of grain refiners can reduce the coercivity of the nanowires. For iron depositions, there are additional types of additives used. One, ammonium chloride (NH_4Cl) has been shown to mitigate the air oxidation of Fe^{2+} ion into undesirable Fe^{3+}. Others, namely malonic acid (MA) and ascorbic acid (AA) are added to iron electrolyte so that the ferric hydroxide ($Fe(OH)_3$) is not produced, which would precipitate iron out of solution [39, 40, 38]. Table 2.1 gives the basic electrolyte recipes used in this work to fabricate nanowires. Additionally, experimental recipes for Gold and FeCo are discussed in Chapter 5.

Several variations on the basic electrolyte recipes found in Table 2.1 may be used, depending on the end result desired. To produce multi-layer NWs, you can combine electrolyte recipes and control which metal is deposited by the voltage, which has been used broadly [41, 15, 42, 34, 43]. Alloys can be fabricated by co-depositing the metals. Specifically, in Chapters 4, CoFe alloys were used in efforts to reach the maximum saturation magnetization of room temperature transition metals predicted by the Slater-Pauling curve. For CoFe specifically, the ratio of Co to Fe is determined by the ratio

Table 2.1: Basic Electrolyte Recipes

Metal	Iron	Copper	Nickel	Cobalt
pH	3	3	3	$2 - 6.4$
Ion Source	[0.20] $FeSO_4$	[0.30] $CuSO_4$	[1.00] $NiSO_4$	[1.54] $CoSO_4$
Buffer Agent	[0.40] H_3BO_3	[0.30] H_3BO_3	[0.50] H_3BO_3	[0.47] H_3BO_3
Surfactant	[0.0003] SDS			
Grain Refiner	1 g/L $Saccharin$			
Other	[0.30] NH_4Cl^*			
	[0.001] MA^{**}			
	1 g/L AA^{**}			

*Reduces air oxidation of Fe^{2+} to Fe^{3+}

$^+$Used to mitigate ferric hydroxide precipitation

of the two salts in the electrolyte when the Fe deposition procedure is followed, which is verified in Chapter 5. The wide range in pH values for Co electrolyte given in Table 2.1 is because the crystal structure of the fabricated nanowires is dependent upon the electrolyte pH. ranging from primarily FCC at a pH of 2 to primarily HCP at a pH of 6.4 [29]. This phenomena provides an additional tuning dial in the case of Co, as the different structures have different crystalline magnetic anisotropy. Tweaking the base recipes allows for variations that can enable designs for different applications.

In addition to the electrolyte composition, controlling the voltage is a critical factor in determining the result of the deposition. It is the applied voltage that makes the electrodeposition favorable when at or above the standard reduction potential of the cell. The standard reduction potential is determined by the half reactions of the reduction and oxidation processes occurring in the electrolyte. These potentials need to be determined with respect to the reference electrode that is in use. The amount of voltage applied above the standard reduction potential of the reaction is called the overpotential. When not in an ion mobility controlled regime, the reaction rate -or current- can be controlled by the amount of overpotential applied to the system. However, while the reaction may proceed quickly, potentials too high can enable side reactions and reaction rates that are too high can produce poor quality wires that do not infill the pore well. Lower rates allow for better control over the deposition. A common method to improve the homogeneity and pore filling of depositions are pulsed depositions [44]. In pulsed depositions the voltage is applied using a waveform (typically square) where the amplitude and frequency are tuned to the deposition. This is especially important for the iron and iron cobalt depositions used in this work [45]. For all the NWs fabricated in Chapters 4 and 5, pulsed electrodeposition is employed to improve the deposition quality.

After nanowires have been fabricated, the sample often needs further modification before use. Typically, the metallic back contact needs to be removed. For AAO-templated NWs, 1.0 M Ferric Nitrate ($Fe(NO_3)_3$) is used as an etchant. The template is floated in the etchant until the copper back-contact visibly disappears. If the nanowires are susceptible to etching by ferric nitrate, oftentimes the deposition process will include a thin etch stop layer of a more resistant metal, such as nickel or gold, before the desired nanowires are deposited. This etch-stop increases the final yield of NWs and gives better control over the final length, but comes with the cost of introducing a new material to your sample that is difficult to remove. For samples produced in track-etched polycarbonate, ion milling can remove the back contact without destroying the template. Some applications require the release of MNWs into solution. To release the MNWs from AAO templates, the templates can be dissolved in 1.0 M NaOH and the MNWS collected on a magnetic stand (full procedure given in Appendix B). The NaOH can be pipetted out, and the MNWs re-suspended in the desired solution. This method does convert a surface layer of the MNWs into the metal hydroxide [15], which can be useful in subsequent coating steps. Further discussion of NW coatings and work on developing new coatings for cryopreservation applications is presented in Chapter 5.

While other fabrication methods exist for nanowires and nanobars, they exhibit significant drawbacks which preclude them from being used for the applications here. These include batch reactions using a reverse micelle method and the nanofabrication techniques typically used in semiconductor fabrication. Reverse micelle techniques, while readily scaled up and easy to coat, are limited in their ability to produce high shape anisotropies. Notably, this can be restricted by diameter size [46], depends on the surfactant and reaction time [47] , and modeling has shown the shape anisotropy rarely exceeds 1:10 [48]. Reverse micelle reactions are also restricted to reactions that can be catalyzed or are spontaneous within the micelle [47], and difficult to produce alloys.

Using nanofabrication techniques like wet etches, DRIE, liftoff and photolithography produce results that may be well controlled, but typically have rough side walls, are expensive, and difficult to scale up. As such, template-assisted fabrication gives the best control over the most important geometric features - diameter and wall smoothness - while allowing for reasonably large quantities to be made at a time

The control over the particle geometry and composition and versatility template-assisted deposition can provide make it an essential technique for the production of magnetic nanowires and nanorods. The diameter and shape of the electrodeposited nanoparticles are controlled by the template geometry, and the length is determined by the reaction rate and deposition time. The material composition and structure are controlled by the electrolyte composition and applied potential. These nanowires can be layered, used-in template, or released depending on the needs of the application. Because of these advantages, the work in this thesis focuses on enabling the use of nanowires and nanorods in a range of applications by addressing knowledge gaps specific to templated nanowires.

2.2.2 Characterization

Scanning Electron Microscopy

Scanning Electron Microscopy (SEM) can image samples at feature sizes down to a few nanometers and give some information on sample composition. SEM uses electrons to probe the material, and since electrons have smaller wavelengths than light in the visible region of the spectrum, SEM can take images with much better resolution than optical microscopy [49]. This resolution is important when working with micro- and nano-structured materials to validate the structure of the fabricated sample. Another advantage of this technique is that minimal sample preparation is required and mm scale or larger samples can be measured, which provides the flexibility for SEM to be used as a versatile tool. Three forms of SEM imaging and detection are used to characterize nanowire samples in this work: secondary electron images, backscattered electron images, and energy dispersive x-ray spectra.

Electron scatter from the sample provide different types of contrast, and the mechanism by which the electron scatters provides different information. Secondary electrons

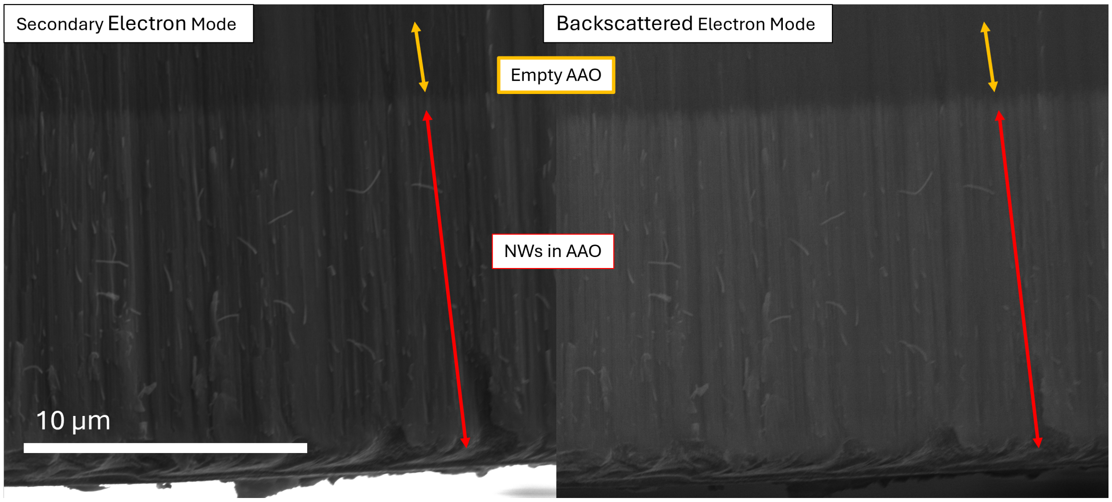

Figure 2.3: SEM images of the same sample section taken in secondary electron mode (left) and backscatter electron mode (right) are compared to show differences in contrast.

(SE) are the lowest energy of the emitted particles and result from inelastic scatter of an outer shell electron by the incoming beam electron. SE images provide information on the surface topology, but little on the material composition. Edges and non-conductive materials will be brighter. In Back-scattered electrons (BSE) imaging contrast is based on the atomic mass of the material. This is because backscattered electrons are beam electrons that have been deflected by the nuclei of the atoms in the material. The heavier the element, the more the electron is deflected, and turned back towards the detector. BSE imaging is exceptionally useful for imaging cross sections of the AAO template with embedded NWs, as the metallic NWs appear brighter than the surrounding AAO. An example comparing the contrast of NWs in an AAO template for SE and BSE mode is given in Fig. 2.3. Because the fracture surface may not be representative of NW sample due to NWs falling out or breaking, BSE imaging allows us not to look at just the surface layer of MNWs, but a the nanowires embedded a layer or two below the surface. Both imaging techniques prove useful as an analytical tool for characterizing the shape and presence of nanowires.

Energy dispersive x-ray spectra, known as EDS or EDX, can give information on precisely which elements are present in the sample [49]. This method requires higher energy electrons than either SE or BSE images, as an inner-shell electron must be ejected.

When a higher energy electron fills the hole, an X-ray is emitted with a wavelength characteristic to that element. Detecting these x-rays allows for the mapping of what elements are present at each point. Because EDX is higher energy that SE or BSE images, the signal can extend deeper into the material, and the penetration depth is dependent on the material. EDX data has a lower resolution because of this, and the mapping of the elements in the sample may not be precise. The exact quantities of the elements have a high error to them [50, 51], and as such this technique is considered semi-quantitative. That said, EDX is a great tool for sample analysis. The spectra of individual points can be found, or line scans and sample maps can be taken which analyzes the composition for broader swaths of the sample. This allows for the presence of elements to be mapped to specific regions of the sample.

SEM is a surface analytical technique, so the sample surface being investigated must be at the surface. In cases where cross-sections must be analyzed, the sample must be fractured, which does not make this an entirely nondestructive technique. Additionally, samples need to be prepared in a way that prevents or mitigates charging of the sample. which occurs when the imaging electrons build up on the sample surface, distorting the image. Therefore, non-conductive samples must be coated with a conductive material such as carbon, and all samples must securely mounted to the SEM stub using a conductive material such as carbon or copper tape. For this work, SEM images of AAO or NWs embedded in AAO needed to be coated with a conductive material to achieve high resolution of the nanowire feature. The need for a good coating was increased when BSE images or EDX spectra were collected, as these techniques require higher accelerating voltages and electron currents to provide sufficient signal and resolution. Because the strong contact with the conductive tape and sample fracture is needed to image the desired portion of the sample, SEM was generally performed last as the sample generally could not be recovered after performing SEM.

X-Ray Diffraction

X-Ray diffraction (XRD) may be used to characterize the composition and crystal structure of templated NWs. This technique uses a beam of X-Rays to detect repeating patterns at the scale of interatomic distances in crystals [52], and therefore determine crystal structures present in a sample. Understanding the structure of the NWs is useful

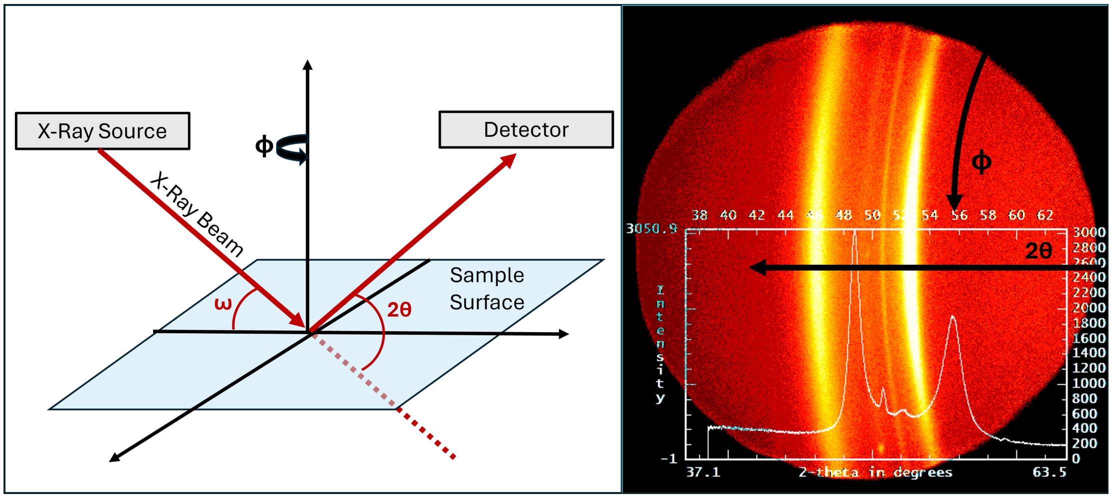

Figure 2.4: A schematic of the sample setup (left) and an example frame of data for 2θ range of $35^o - 65^o$ (right) with the angles labeled.

when characterizing NWs, as the crystal structure and texture can effect the electronic and magnetic properties of the nanowires. Both AAO and polycarbonate NW templates are amorphous and have no significant signal, so NWs do not need to be removed from the template to perform XRD. As for sample preparation, the Cu layer used as the electrical contact during fabrication must be removed, and the sample surface should be cleaned (typically with acetone, then isopropyl alcohol) to help ensure a clean, strong signal. The sample is then mounted with double sided tape to a piece of silicon wafer, as shown in, which can then be mounted in the X-Ray Diffractometer for measurement. A constant wavelength of X-Rays are used and the angle the x-rays are incident on the surface is changed. While the Copper K_α peak is often used for standard XRD measurements, in this work $\lambda = 1.789$ Å, or the Co K_α peak is used. The data can be collected in frames, shown in Fig. 2.4, then integrated over ϕ to yield the XRD spectra that are typically reported as a function of the angle 2θ. XRD spectra for the materials studied here are generally well-understood and well-documented, and as such we can compare the peaks to computed or documented powder diffraction spectra to evaluate if the phase is present and if significant crystal texture or strain is present.

Powder diffraction peaks are the expected peaks when grains of the crystal are randomly oriented in the sample. A sample with randomly oriented crystal grains should have the same peaks at the same ratios as the powder diffraction pattern. Different materials may be differentiated, even if they have the same crystal structure, because the different interatomic spacings will either expand or contract the pattern, with differences being the most clear at large values of 2θ. Crystal texture, or a preference for certain grain orientations in the sample, can be indicated by missing peaks, peaks in ratios significantly different to the powder diffraction pattern, or in peaks where the intensity changes as a function of ϕ. In the example frame in Fig. 2.4, some texture can be seen where the intensity of the bands vary with ϕ. In magnetic materials, with crystalline anisotropy, crystal texture may change the magnetic behavior of the sample. If a single crystal orientation is present, only certain peaks in the diffraction pattern will be present. Therefore, you can determine the sample composition and structure nondestructively using XRD.

Further information on the crystal lattice can be determined by changes in the XRD spectra peaks. Small shifts in the peak location can indicate lattice strain, which is common in nanostructured sample. If this strain is greater in certain lattice directions (indicated by larger peak shifts on some peaks than others) the strain may influence the magnetic properties or reactivity of the sample. Peak broadening can be used to estimate the grain size in a sample, as the peak width is inversely related to the grain size [53, 54]. However, instrument configurations may also lead to broadening in the peaks, so this is an estimate that works best in comparison. In the example frame shown in Fig. 2.4, there is significant broadening of the two most intense bands, which can be contrasted with the thin, faint bands in between. Quantifying these distortions in XRD spectra can give insight into the lattice structure that may help explain the behavior.

Magnetometry

The vibrating sample magnetometer (VSM) is a tool used to measure the magnetic moment of a sample as a constant magnetic field is applied. The magnetic field is applied to the sample using an electromagnet, and the sample is mounted on a fiberglass rod in between two pickup coils. When the sample is vibrated at a set frequency, this change in the magnetic field at the pickup coils induces a measurable voltage in the pickup coils that measures the magnitude of the stray field produced by the sample [21]. By calibrating with a sample with a known geometry and magnetic moment, typically a nickel standard, the magnetic moment is determined from the stray field. If the volume of the sample is known, the magnetization can be computed. Notably, for templated MNWs, the measured magnetic moment of the measured sample will be slightly greater when measuring with the magnetic moment in-plane than out-of-plane due to the difference in geometry from the standard. The two primary measurements made using the VSM are hysteresis loops and first order reversal curves.

Hysteresis loops measure the magnetic moment as a function of the applied field. A major hysteresis loop measures the moment, fully saturating the material in both directions. The measurement of a major hysteresis loop will give a measurement of the saturation magnetic moment, the applied field at saturation, coercivity, and remanent magnetic moment. In addition to these points, the shape of the hysteresis gives insight into the magnetic behavior. The total area enclosed in the hysteresis loop can measure the energy lost in one magnetization cycle. The comparable shearing of the hysteresis loops taken at the same temperature can give insight into the extent of interaction between two particles [31]. Additionally, hysteresis loops with non-standard geometry such as wasp-waists and potbellies can indicate exchange-coupled soft and hard magnetic layers depending on the sign of the exchange parameter and the coercivities [55]. However, to differentiate the mechanisms possible for producing these shapes, further measurements, such as First-Order Reversal Curves (FORC), should be made. Some information on the switching behavior can be collected by taking minor loop measurements. Minor hysteresis loops measure only a portion of the full loop. However, it is worth noting that VSM measurements are a static technique, and cannot necessarily capture the dynamics of switching. This is useful for predicting magnetization behavior and hysteretic losses in applications where saturation is not achieved.

First order reversal curves (FORCs) give more insight into the switching and magnetic behavior of the sample. Specifically, FORCs allow for the computation of a distribution of interaction and coercive fields in a sample [56]. To measure a FORC: the sample is magnetically saturated, a lower reversal field is applied, then the magnetization of the sample is measured as the field is brought back up to saturation. This data is used to compute the FORC parameter as in Eq. 2.2, ρ_{ab}, as a function of the applied field, H_a, and the reversal field, H_b. Generally, this parameter is transformed (Eqs.2.3 and 2.4) to be a function of the coercive field, H_C, and the interaction field,

H_U (Eqs.2.3 and 2.4). A distribution of the FORC parameter is plotted on a map of the coercive field and interaction field. For arrays of magnetic nanowires, these maps give insights into the coercivity distribution of the individual nanowires and the interactions between them [57, 57].

$$\rho_{ab}(H_a, H_b) = -1/(2M_S)\ \partial^2 M(H_a, H_b)/\partial H_a \partial H_b \tag{2.2}$$

$$H_a(H_C, H_U) = (H_U + H_C)/2 \tag{2.3}$$

$$H_b(H_C, H_U) = (H_U - H_C)/2 \tag{2.4}$$

Because full FORC measurements take time to collect and require collecting around tens of thousands of data points, they are not always desirable to perform. The projection method [58], allows for some of the information of interest, such as separating reversible (RSF) and irreversible (ISF) switching field without needing to collect as many data points. The ISF can be calculated by taking the change in magnetization with respect to the change in the reversal field, evaluated for each applied field. Mathematically, this is expressed as Eq. 2.5. Experimentally, this is the slope between two reversal curves end points.

$$ISF = \left.\frac{\partial M(H_a, H_b)}{\partial H_b}\right|_{H_a=H_b} \tag{2.5}$$

The RSF can be calculated by taking the change in magnetization with respect to the change in the applied field, evaluated for the reversal field. Mathematically, this is expressed as Eq. 2.6. Experimentally, this is the slope of $M(H_a)$ at the reversal field for a given FORC.

$$RSF(H_a) = \left.\frac{\partial M(H_a, H_b)}{\partial H_a}\right|_{H_b=H_a} \tag{2.6}$$

The ability to calculate the ISF and RSF can help differentiate the presence of soft and hard components in a magnetic sample. This method is used in Chapter 3 to separate out the behavior of hard and soft layers in the sample.

Chapter 3

Vertically Integrated Nanowires

3.1 Introduction

Today, most electronics are made on and - to some extent - in silicon wafers. Silicon is abundant and most nanofabrication techniques have been built to be used with silicon wafers due to its dominance as a substrate in the semiconductor and electronic device industry. Therefore, in order to enable the use of nanowires in electronic and nanoscale devices, it is advantageous to have a way to stably integrate them onto a silicon wafer. Nanoscale wires and leads oriented horizontally along the wafer surface are common, typically made by using photolithography to pattern a metal thin film. However, for applications where nanowires with high shape anisotropies, smooth sidewalls, and oriented vertically to the wafer surface are desired, more development is needed. Here, a method is demonstrated that stably allows for the integration of a vertically oriented nanowire array into silicon technologies.

Established thin film patterning methods that can produce vertical columns such as a deep-reactive ion etch (DRIE) or Bosch etch produce pillars and other high shape anisotropy geometries. However, the pillars produced by DRIE and Bosch etches are ridged due the cyclic process of plasma etching followed by passivation required to obtain high shape anisotropies [59, 60, 61]. As discussed in Section 2.1, the surface quality of nanowires heavily influences the resistivity and magnetic properties of the wires. In the case of resistivity, textured surfaces increase the resistivity, which results in more energy loss in electrical devices made with these wires. In magnetic nanowires, this can result in domain wall pinning which can effect the reversal behavior of the nanowire. Also, rougher surfaces may affect the ability for electrodeposited material to conform to the pore, making the result less predictable. A version of the Bosch process with a smooth surface has been reported [62]. However, this method produced a maximum shape anisotropy of 28:1, which is significantly less than what is needed for many nanowire applications. In order to get the electrical and magnetic properties desired for some applications, it would be useful to be able to integrate an AAO template vertically onto the surface of a Si wafer, so that template-assisted electrodeposition may be used to fabricate nanowires and integrate them into electronic devices.

The method used to make free AAO templates, which are AAO templates that are not attached to a substrate, is well established with many variations depending on your desired product. To make free AAO, an electrochemical process is used to oxidize aluminum, which results in a substrate that has even, columnar pores instead of the thin native oxide layer that spontaneously forms on the surface of aluminum. The aluminum film serves as the anode, and depending on the reaction conditions, such as applied voltage and the electrolyte, pore sizes may vary from 10-400 nm or even none at all [35]. The organization of the pores can be dependent on surface texture of the aluminum [7]. Once the desired thickness of AAO is achieved, the remaining aluminum can be etched away to free the AAO using an etchant such as copper chloride or mercury dichloride. Once fabricated, the pores should be lightly etched to ensure the base of the pores are open, allowing for electrical contact to the layer below, and to adjust the pore sizes as desired. This is the general method that free AAO templates are fabricated, although the exact process used in purchased templates, such as those used in Chapters 4 and 5, are not fully disclosed.

Variations on the anodization process can change the pore size, regularity of the pores, and even produce 3D networks of pores [35, 7]. One modification used to improve the surface layer and the regularity of the pores is double anodization. This method, developed in 1995, can produce a regular, even honeycomb pattern to the pores [63]. Here, a first anodization is done which, when etched away, produces even divots on the aluminum surface. These divots then become pore nucleation sites for the start of the second anodization. To produce a hexagonal, ordered array an extended first anodization must be performed, which can take more than 10 hours due to slow oxide growth rates and the use of a relatively thick first anodization that just gets etched away [64, 35, 42]. Here, the thickness of aluminum required for using the full process is infeasible. Physical vapor deposition methods like evaporation are capable of making thicker layers, but in shared facilities is discouraged, due to metal buildup and the increased need for equipment maintenance. In order to obtain pores with greater order than the single anodization, but allowable within the fabrication constraints of the physical vapor deposition processes, a modified double anodization process is developed and used in this chapter.

In addition to the need for modifying the aluminum thickness and adjusting processes to accommodate for integration needs, an important factor to consider when making film stacks is strain within and at the interface of the films. As aluminum is anodized, the volume increases, introducing strain in the film. If an adhesion layer is not present between the Al/AAO and the conductive layers below, the AAO will delaminate in order to eliminate the compressive stress on the film. Adhesion layers tested in literature [65, 66], interfaced with expensive metals such as platinum and gold, and the mechanical stability is not verified. In this work, a copper conductive layer is used for deposition and, for the RF devices, as a ground layer. In order to interface the Al/AAO layer with the copper, a thin TiW layer is deposited between the copper and aluminum as an adhesion layer. This adhesion layer used here was developed by a senior student, Joseph Um [67], and used initially in the single anodization process.

In this chapter, two variations of a vertically integrated AAO process were tested. One method, referred to as the "1x anodization process" uses a single-step anodization process utilizing the TiW adhesion layer[67]. The second process, called the "2x anodization process", builds off of the 1x anodization process, but uses a two-step anodization process modified such that it is feasible with the film thickness constraints for this method. Both variations used oxalic acid electrolyte and a 40 V potential to target pore diameters of around 20-30 nm. The resulting material was tested for durability and controllability. Nickel nanowires were deposited into the integrated AAO templates and the magnetic behavior was tested. Cu nanowires were tested for resistivity and performance as grounding vias in high frequency applications. The initial method was developed by a previous student, Joeseph Um. The modified two-step anodization was developed and all sample fabrication and measurements were performed by the author unless otherwise noted. This work demonstrates the benefits and limitations of the single and modified two-step integrated nanowire processes, and is expanded by using vertically integrated nanowires in an application.

3.2 Methods

3.2.1 Sample Fabrication

The full sample fabrication method up to and including nanowire deposition is summarized in Fig. 3.1. Starting with a (100) Si wafer, a metal stack was deposited before anodizing the Al on top. To build the metal stack, sputtering (AJA II Sputterer) was used to deposit 40 nm Ti, 115 nm Cu, and nm $Ti_{0.2}W_{0.8}$. This first stack served as an electrically conductive backing, and an adhesion layer to bind the Cu to the Si wafer and the Al/AAO layer to the Cu. Immediately after sputtering, a layer of Al was evaporated (CHA Evaporator) on top. This aluminum will be transformed during anodization to form the porous AAO template.

In both the 1x and 2x anodization process, the top layer of Al was anodized in a 0.3 M oxalic acid at 40 $V_{Ag/AgCl}$, chilled to 16 °C using a circulating water bath. In the 1x process, the Al was anodized until the Cu layer was reached. For the 2x process, the Al was anodized for 1.5 minutes before etching back the surface AAO with 1.6 wt% H_2CrO_4/6 wt% H_3PO_4. The remaining Al was then anodized through until the metal contact layer was reached. The point when the metal back contact was reached was determined when the current began to rapidly increase after having reached a minimum value. This took about 11 minutes after beginning the anodization process for an 850 nm thick layer of Al. After anodization, pores were widened using 5 wt% H_3PO_4 etchant. After the desired pore size was achieved, the Si-integrated AAO template was either filled with NWs or patterned using a photolithography process then filled with NWs.

To assess the magnetic properties of MNWs in Si-integrated AAO templates, Ni nanowires were deposited into a template made using the 2x anodization process. Double-sided copper tape was used to make electrical contact with the electrode stack. Vinyl tape was used to isolate regions of the wafer where electrolyte contact was undesirable and nanowires were not to be deposited. The electrical potential used to deposit the MNWs into the template was controlled by a power supply (Arbin Battery Tester),

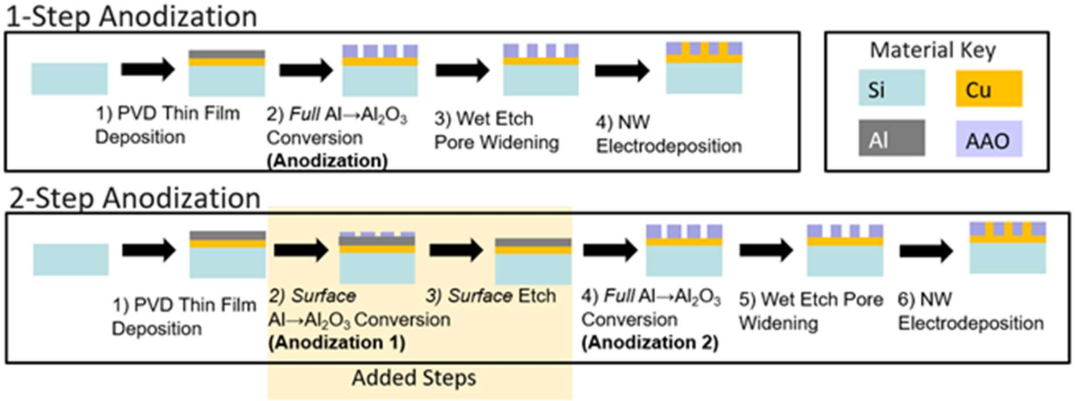

Figure 3.1: Schematics summarize the process flow used to fabricate the integrated NWs.

and a 3-electrode setup with a Ag/AgCl reference probe was used. A constant voltage of 90 mV$_{\mathrm{Ag/AgCl}}$ was applied in a Ni electrolyte (0.3 M $NiSO_4$, 0.3 M H_3BO_3, pH 3). The pH was adjusted using H_2SO_4 and/or NaOH as needed. The copper was deposited into the pores in 3-5 minute intervals, wiping off overgrowth (excess metal that has grown out of the pores) between each deposition. Wiping off the overgrowth was performed to create a more uniformly filled template by removing overgrowth that may block the openings of - and therefore inhibit deposition in - nearby pores.

To fabricate coplanar waveguides with NW interconnects [68, 1], templates were fabricated using using the 1x anodization process integrated onto a high resistivity silicon wafer ($\rho > 5k\Omega - cm, \epsilon_r = 11.7$, thickness $525 \pm 25\mu m$). To infill the pores with Cu NWs, a constant voltage of 50 mV was applied in a Cu electrolyte (0.3 M $CuSO_4$, 0.3 M H_3BO_3, pH 3). Otherwise, the deposition method was identical to Ni. Once the Cu was electrodeposited into the pores, Cu was sputtered on the AAO-NW surface. The wafer was then patterned using photoresist, etching back the AAO layers with 10 wt% NaOH to make the waveguides for testing. A narrow coplanar waveguide was made for the low frequency (10 MHz - 40 GHz) measurements, while a wider coplanar wavguide device was made to measure on the 10 MHz - 110 GHz and 140 -180 GHz setup. After the nanowires were deposited, the samples were handed off to Aditya Dave in Prof. Rhonda Franklin's lab to finish the fabrication of the coplanar waveguide.

These samples were used for high frequency device testing.

3.2.2 Mechanical Performance

The mechanical performance of the vertically integrated AAO films on silicon were tested on wafer quarters without the inclusion of electrodeposited wires. To evaluate if the adhesion of the AAO layer to the wafer was robust, the method described in ASTM D3359 "Standard Test Methods for Measuring Adhesion by Tape Test" [69] was used. More extensive testing was done by targeting the AAO-metal interface with tweezers, then a chisel and mallet. Thermal stability was determined by heating wafer pieces with vertically integrated AAO in a tube furnace. The temperature was increased by intervals of 50 ^oC, starting at 100 ^oC and continued until delamination. At each interval, the samples were heated in the furnace for 10 min once the desired temperature was achieved. Between steps, the samples was cooled and removed for testing. The mechanical tests were used to evaluate the stability of the assembly and determine the thermal processing constraints after the aluminum layer is anodized.

3.2.3 Fabrication Confirmation and Pore Sizes

SEM (Scanning Electron Microscopy) was used to confirm the layers and evaluate the pore sizes of the anodized templates. To confirm the fabrication and dimensions of the vertical AAO layer and integrated NWs, samples were cleaved and the fracture surface - which was a cross section - was mounted and evaluated using SEM, EDX, and BSE imaging. To characterize the size of the pores, samples without any NWs deposited into the pores were used. Wafer sections were made and mounted surface side up, coated with 5.0 nm of conductive carbon, and SEM images were collected for the surfaces.

To collect data on the pore areas of the Si-integrated AAO templates, ImageJ [70] was used to determine the pore areas using a pixel counting method. Diameter calculations were made with the assumption of circular pores. ImageJ's Analyze Particles function was used to count pixels in each pore. First, the scale of pixels:nm was set to the scale bar located at the bottom of each SEM image. The pixels are then converted to nanometers for all measurements. After scaling the measurements, the threshold was set manually so that most of the points were outlined, but few of the gray dimples were

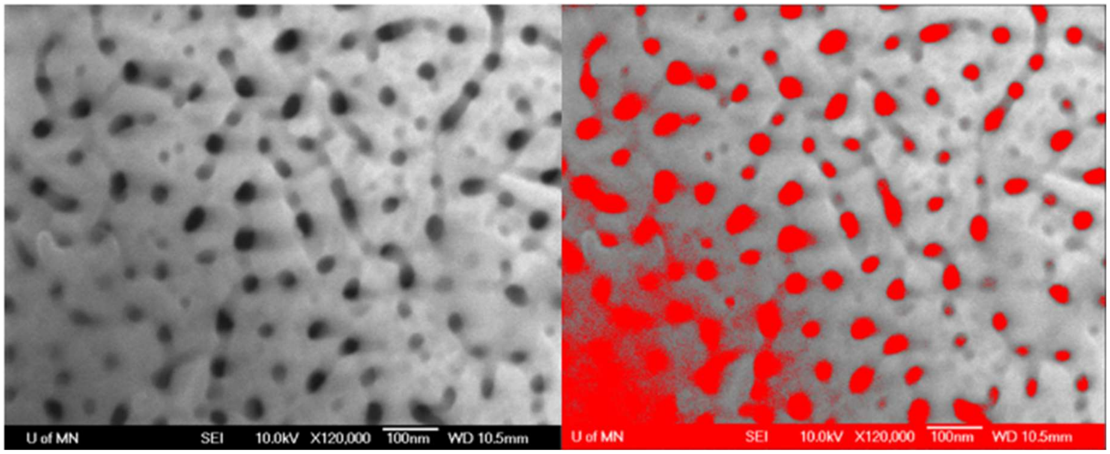

Figure 3.2: A sample SEM image (left) used to determine pore size distribution is shown. Right is the overlay of the pores detected by the program in red.

included. This must be done manually, as contrast varies between SEM images. Fig. 3.2 shows the overlay where a 59.5% threshold was set (right) compared to the original image. Once the threshold was set, the analyze particles tool was used with a standard circularity threshold of 0.15, and a minimum area of 30 nm^2. The minimum was set to exclude points that were smaller than the pore sizes. A labeled image, list of points and areas is generated. The labeled image is used to exclude points that do not meet the selection criteria. For the example shown in Fig. 3.3, the labeled image is compared to the overlay and original.

Data points were only discarded if they did not match up well to the image of the pore. These discarded points fell into two categories:

1. Multiple pores merged into one, or a wide/ambiguous pore mouth was included in the measurement (shown in Fig. 3.4).
2. Points appearing much larger or smaller due to significant contrast differences from the rest of the image.

The reason for point rejection in the example (Fig. 3.3) are all due to criteria 2, contrast differences. For the example image, the contrast in bottom left corner was poor, such that points merged together and tiny isolated patches were picked out by the analyze

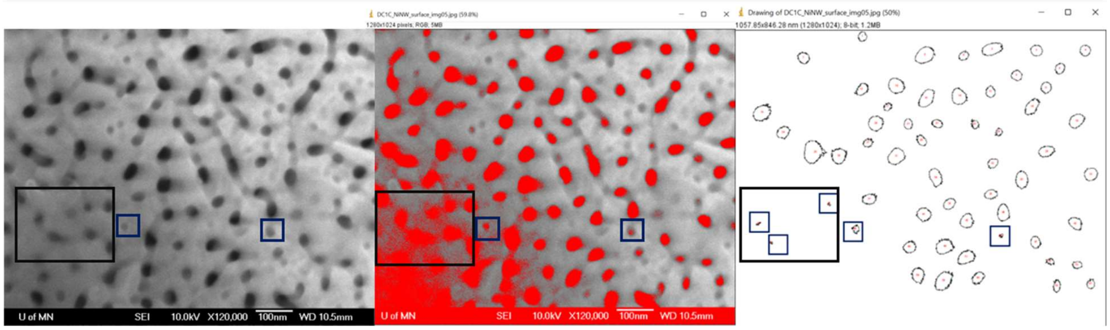

Figure 3.3: The original (left), red overlay (center), and numbered outlines (right) images of the pores is shown. Black boxes indicate where pore measurements were thrown out manually due to not meeting the criteria.

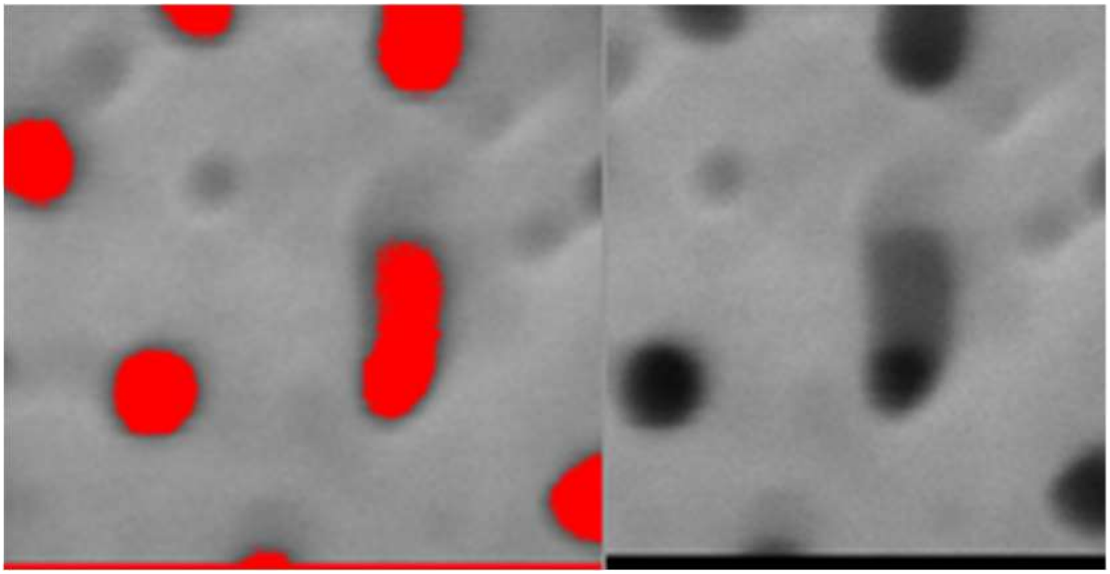

Figure 3.4: The overlay (left) and original image (right) for a pore with an ambiguous bean-shaped mouth is shown.

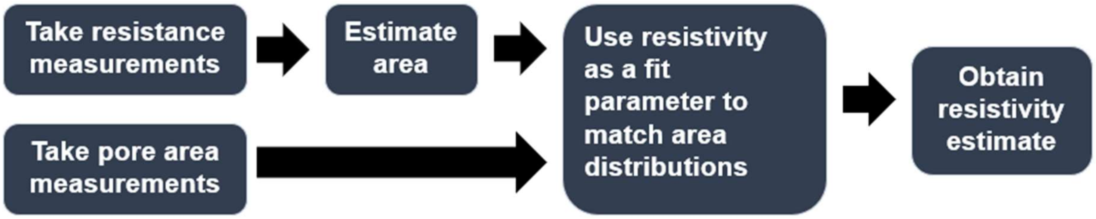

Figure 3.5: The work flow for the resistivity estimate is shown.

particle function as points. These points included in the black box (Fig. 3.3 could not be traced to any identifiable pore.

3.2.4 Resistivity Estimate

Wafer quarters with copper nanowires electrodeposited into the integrated AAO were used to estimate the the average resistivity of copper wires in-template. Resistivity is an indirect measurement, typically determined using resistance measurements and the geometry of a sample. However, it is not feasible to measure a single nanowire in-template with the available equipment due to size and visibility constraints. Out of template, the etchant required to release the NWs from the template will alter the surface of the wires, as no etchant is perfectly selective. As such, a method to develop an estimate is employed which uses resistivity as a fit parameter to match measured area and resistance distributions. This method used both area measurements, as described in section 3.2.3 and resistance measurements, described below to estimate resistivity. A summary of the work flow to determine an estimate is shown in Fig. 3.5.

The resistance of nanowires was measured using a 4-wire resistance measurement from the wafer surface, contacting nanowires that emerge from the top of the pores. In a 4-wire setup, there are only 2 sample contacts, but the leads split. Two leads are used to measure the current and the other two measure the voltage. Ohm's law is then used to determine the resistance. A schematic of the measurement setup is shown in Fig. 3.6a. The measured resistance is composed of multiple resistances in series, namely: the system resistance (R_{sys}), probe to nanowire contact resistance ($R_{contact}$), and the resistance of the wires (Eq. 3.2). R_{system} was verified every 50 resistance measurements in order to ensure the value does not drift too much due to probe heating as the setup is used. The wire resistance is composed of all the wires to which electrical contact is made in parallel (Eq. 3.2).

Because the probe tip used to contact the nanowires has a tip diameter of 25-100 nm, one, two, or three nanowires can be contacted at a time unless the probe tip touches a mushroom that contacts many more nanowires. Fig. 3.6b demonstrates maximum probe tip areas relative to the surface of a template where some wires have been electrodeposited. The probability of mushroom contact was reduced for measurements by lightly sanding down the surface of the AAO but was not done on the SEM sample pictured in figure 10. Resistances were measured across the exposed surface of the wafer to acquire a minimum of 350 data points. More data points may be desired to delineate the curves associated with hitting more than one nanowire. Previous work by Joseph Um [71] demonstrated that when there is a small distribution of nanowire sizes, there are three different gaussians for 1, 2, and 3 contacted nanowires. However, his work was performed using commercial templates with a small pore size distribution and longer nanowires. While in this work, enough data points have not been taken to clearly differentiate the multiple nanowire peaks, it is expected that reducing the spread of the diameter distribution of the wires more will allow resolution between the 1, 2, and 3 nanowire peaks. This increased resolution will allow for a more accurate, and likely larger, estimate of resistivity.

$$R_{meas} = R_{contact} + R_{sys} + R_{Wires} \tag{3.1}$$

$$R_{wires} = (1/R_1 + ... + 1/R_n)^{-1},\ where\ n = \#\ wires\ contacted \tag{3.2}$$

Hundreds of data points were taken for both area (Section 3.2.3) and resistance, producing statistical distributions of each due to the spread in areas produced by anodization and potential variation in topography of the nanowires themselves. After the distributions were collected, the process summarized in Fig. 3.5 was applied to estimate the resistivity, using resistivity as a fit parameter to relate the area and resistance distributions. The equation used to relate the geometric parameters -area (A) and length (l) - and resistance (R) of the wires to the resistivity (ρ) is shown in Eq. 3.3. Variables with significant statistical distributions when measured are indicated to be functions of

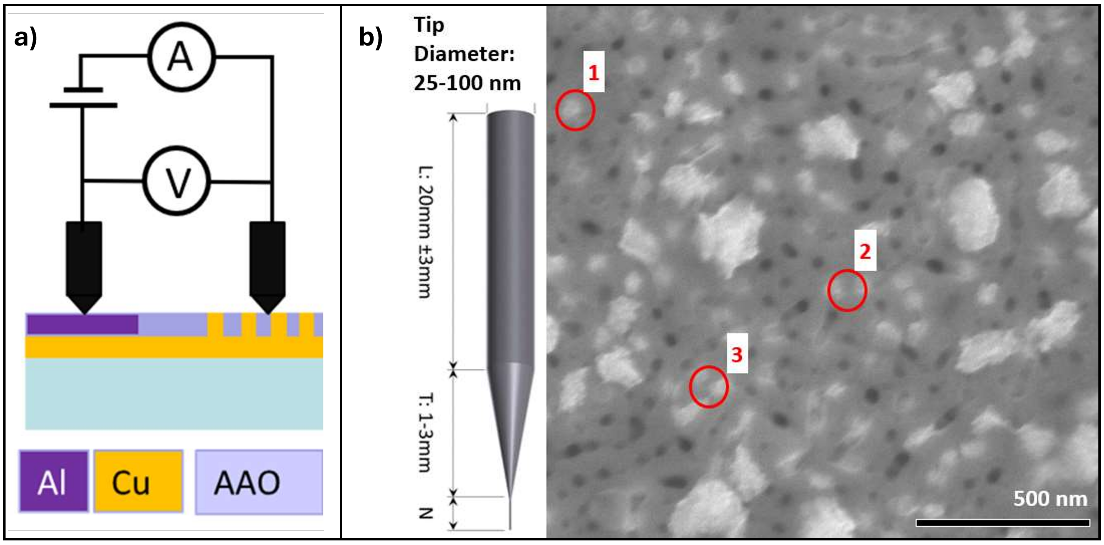

Figure 3.6: a) A schematic of the 4-wire resistance measurements used to measure NW resistance. b) Red outlines demonstrate possible contact areas of the probe tip on an AAO template that has nanowires deposited into the pores. Cases are marked where the probe tip hits one, two, or three nanowires.

the mean (μ) and standard deviation (σ). The estimated resistivity was calculated after matching area distributions using Eq. 3.3, with the mean area and resistance values derived from the gaussian fits, and the length determined from SEM images of the AAO cross section. The MATLAB code written and used to perform the curve fits and estimate the resistivity is in Appendix C. This method was performed on samples prepared using the 1x and 2x anodization process and compared to evaluate differences in process control. The error associated with the resistivity value was determined using a partial differential error propagation method, a sample calculation of which is demonstrated in Appendix D.

$$A(\mu_{AR}, \sigma_{AR}) = \rho \cdot l / R(\mu_R, \sigma_R) \tag{3.3}$$

3.2.5 Magnetic Response

The magnetic response of vertically integrated Ni nanowires fabricated using the 2x anodization method was measured using a VSM (Princeton Micromag). Hysteresis loops were measured both parallel and perpendicular to the nanowire axis, and FORCs were collected with the magnetic field parallel to the wire axis. The projection method discussed in Chapter 2.2.2 was applied to extract the hysteresis loops for the hard and soft magnetic components.

In addition to the measured values, simulations performed by Yicong Chen were used in the analysis. The switching dynamics of a single nanowire was simultated in OOMMF (Object-Oriented MicroMagnetics Framework) [72] at 0K. The 30 nm diameter, 1 μm long wire was set to have an exchange parameter (A) of $9 \cdot 10^{-12} J/m$ and a saturation magnetization of $490 kA/m$. The switching field oriented along the wire was determined and used to evaluate the validity of the experimental measurements.

3.2.6 High Frequency Performance

In order to measure a broad range of frequencies, multiple measurement setups were used. For the 10 MHz to 40 GHz test on the narrow coplanar waveguides, the S-parameters were measured using a 37369D Anritsu Vector Network Analyzer (VNA). To interface with the device, GSG probes (Formfactor ACP50) with a pitch of 150 μm

was used to contact the coplanar waveguide on a probe station (Cascade RF1). The wide coplanar waveguide designs were tested over the frequency ranges 10 MHz -110 GHz and 140-180 GHz, and for both ranges the S-parameters were measured using an E8361C Keysight VNA. For the 10 MHz-110 GHz range, GSG probes (Infinity I110A) with a pitch of 100 μm on a probe station (Cascade M150) were used to contact the device. For the 140-180 GHz range, GSG probes (Infinity I220T) with a pitch of 50 μm. The S_21 of the devices was plotted with respect to the frequency to compare the performance to a traditional coplanar waveguide. All high frequency measurements described in this section were performed by Aditya Dave in Prof. Rhonda Franklin's Group (if $f \leq 40\ GHz$) or Nikita Mahjabeen in Prof. Rashaunda Henderson's Group (if $f > 40\ GHz$).

3.3 Results

3.3.1 Mechanical Stability of Si-Integrated AAO

When tested for film adhesion at room temperature, the Si-integrated AAO layer did not delaminate from the Si wafer during the tape test or when tweezers were used to try to remove the AAO layer. The chisel and mallet broke the silicon wafer before the AAO would separate from the surface. Additionally, the AAO layer did not delaminate in subsequent processing steps used to deposit nanowires and fabricate coplanar waveguides. These steps included electrochemical reactions, application and removal of vinyl tape, sputtering, wet etches and photolithography. The absence of delamination during these steps indicates that the adhesion of the AAO to the metal stack adhering to the Si wafer is robust enough to allow for device integration.

When the template was heated, the film remained adhered to the wafer until the 400^oC data point, where delamination became evident after a tape test. Above 800^oC, free AAO templates crystallize, which sets a hard cap on the viable processing temperatures after AAO conversion. Table 3.1 summarizes the known adhesion behavior of the AAO to the wafer surface at different temperature ranges. This may limit the processing steps that may be performed after the aluminum is anodized to low-temperature processes, excluding processes such as: annealing, diffusion doping, and dopant drive-in.

Table 3.1: Thermal Processing Capabilities After Anodization

Temp. Range (^oC)	AAO Film Adhesion
$16 - 350$	Safe processing zone with no measured delamination
$350 - 800$	Delamination seen on heated AAO, may be mitigated
> 800	AAO Crystallization causes the film to crack

3.3.2 Geometric Control

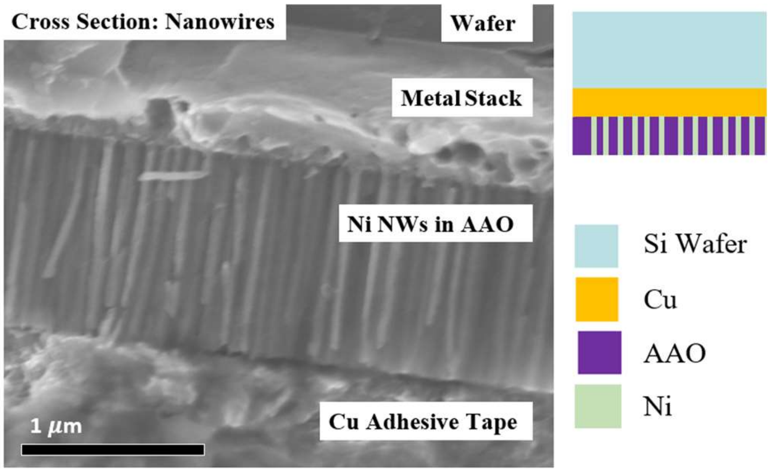

Figure 3.7: A cross section of the AAO layer (left) filled with NWs is shown and compared to a schematic (right).

Cross-sections (Fig. 3.7) showed the AAO thickness for the 1x process to be $1.05 \pm 0.01\mu m$ and $1.3 \pm 0.1\mu m$ for the modified 2x process. Because the 2x process has a wet etch step, there is more variability in the final thickness of the AAO layer between samples, and results in less control over the nanowire length compared to the 1x anodization process. Measurements of the wire diameter at the base, middle, and tip were within standard error of the measurement for a majority of the wires, which supports the use of the surface pore areas as a measure of wire diameter. Fig. 3.8 demonstrates the differences in pore regularity and circularity between the processes. Visually, the circularity is improved at the surface with the 2x anodization method compared to

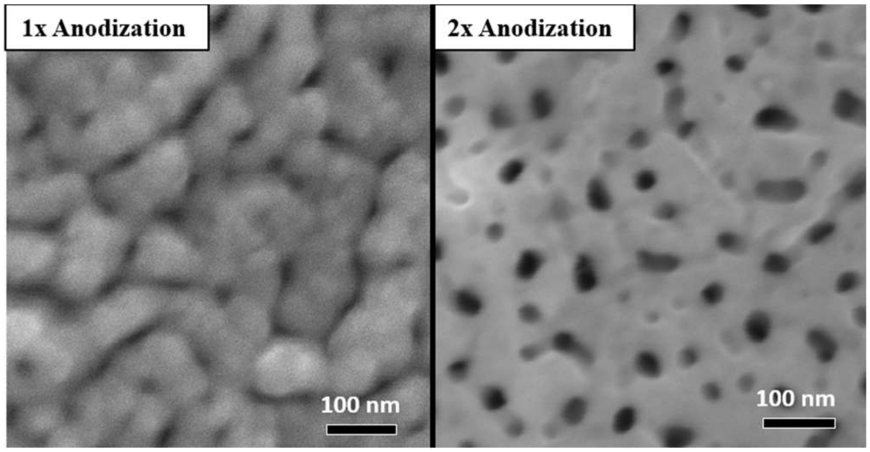

Figure 3.8: SEM images of the AAO surfaces are shown for the 1x anodization process (left), and the 2x anodization process (right).

the 1x method. For applications sensitive to the wire resistance improvement in circularity is important, because increased surface area and roughness increases resistivity significantly in 1D materials such as nanowires.

Table 3.2: Mean Pore Dimensions

Process	Area (nm^2)	Calculated Diameter (nm)
1x Anodization	880 ± 120	34 ± 12
2x Anodization	646 ± 30	29 ± 6

The 2x process demonstrated a tighter distribution of pore areas under anodization and etch conditions that were otherwise the same. The measured distributions are shown in Fig. 3.9. The spread of the fitted gaussians for each pore area distribution was 506 ± 73 nm^2 and 277 ± 20 nm^2 for the 1x and modified 2x processes respectively, demonstrating the reduced spread in areas for the 2x process. Mean pore dimensions based on the fits are given in Table 3.2. It is expected that the eccentricity of the nanowires in the 1x sample contributes to the increased average area compared to the 2x anodization. As NWs magnetic properties strongly depend on the diameter of the wire, the finer control over diameter compared to thickness is a distinct advantage of the 2x anodization process.

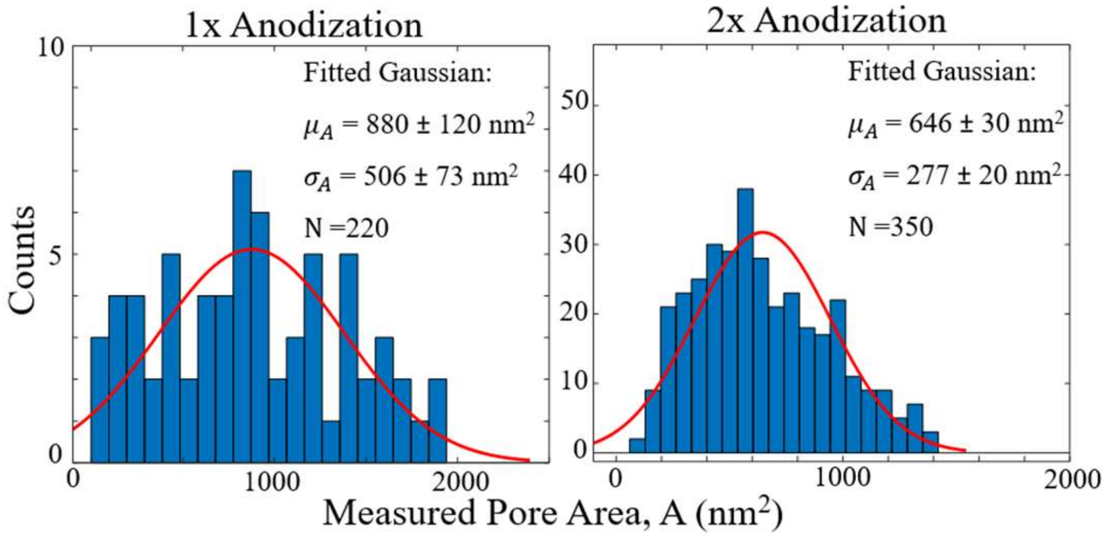

Figure 3.9: Distributions of pore areas are shown for the 1x anodization process (left), and the 2x anodization process (right).

3.3.3 DC Resistivity of In-Template NWs

Because of equipment and sample constraints, this study is limited to obtaining an estimate for the mean resistivity for a given sample. This can be used in situation where you need to provide an average value, such as what you would use in simulation. In order to estimate the resistivity of copper nanowires in Si-integrated templates, hundreds of pore areas and wire resistances were measured for both the 1x and 2x process. Resistivity was then used as a fit parameter to match the resulting two distributions, using Eq. 3.3. For the resistance measurements, the R_{system} was $2.5 \pm 0.4\ \Omega$, and was subtracted out from all resistance measurements in the distribution. When performing the resistivity fit, the initial guess for resistivity was determined by inputting the measured mean values for diameter into Eq. 2.1 and using literature values for $\rho_o^* = 1.46\ \mu\Omega - cm$ and $\lambda_e = 39.9nm$ [73]. The results of the fits, along with the original resistance data are shown in Fig. 3.10, and Table 3.3 summarizes the results of the resistivity estimates with uncertainty contributions from the different variables.

For the 1x andodization, an estimated resistivity of $36 \pm 26\ \mu\Omega - cm$ at a mean pore size of $880 \pm 120\ nm^2$ (for a circular pore, this produces an average diameter of

Table 3.3: Resistivity Estimate Results

Data Set	1x Anodization	2x Anodization
Area (nm^2)	880 ± 120	646 ± 31
Resistance (Ω)	699 ± 291	700 ± 290
Length (nm)	1030 ± 10	1110 ± 20
Resistivity ($\mu\Omega - cm$)	36 ± 26	25 ± 17

34 ± 12 nm). For the 2x anodization, an estimated resistivity of 25 ± 17 $\mu\Omega - cm$ at a mean pore size of 646 ± 31 nm^2 (for a circular pore, this produces an average diameter of 28.7 ± 6 nm). Some variation in the resistivities is to be expected between the two methods, but it would be reasonable to consider the 2x anodization method a more trustworthy estimate. This is because, as was observed in Section 3.3.2, the geometry of the nanowires was observed to be much more circular for the 2x process than the 1x process. As circular pores were assumed for the resistivity calculation, this is a significant factor. Additionally, the 1x process may produce pore openings that are more tortuous or irregular than the entirety of the pores, which means the measurements for the pore area may not be as accurate as for the 1x process. Lastly, the 2x method produced tighter area and resistance measurement distributions, significantly lowering the error in determining the mean values. This allowed for comparable standard deviations (overlapping values within error) when matching the calculated area and measured area distribution curves. All these factors increase confidence in the 2x resistivity estimate compared to the 1x resistivity estimate.

To understand the sources of error, the partial differential error propagation method was used to break down how each measured term contributes to the error of the calculated resistivity value. This method is described in Appendix D. The breakdown of the error contributions for both the 1x and 2x anodization calculations are given in Table 3.4. For both processes, the resistance data contributes the greatest error by an order of magnitude. If this method is to be used for further estimates,enough data should be collected such that different peaks for contacting 1, 2, or 3 wires in parallel could be differentiated. Separating out the 1-wire peak and using it for the resistivity estimation method would improve the accuracy. The second greatest contribution to the error was from error in the mean measured area. There was a significant difference between the

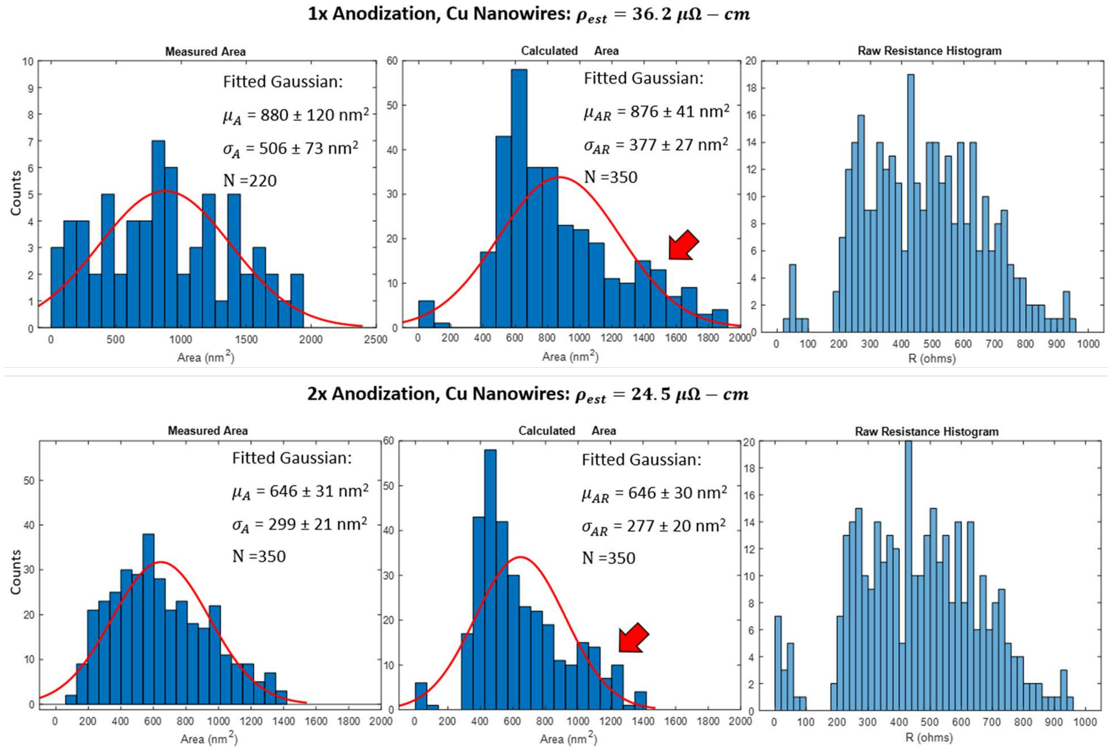

Figure 3.10: This panel shows the measured area and final calculated area distribution alongside the resistance histograms for used for the calculated area. The 1x and 2x anodization process are shown on top and bottom respectively. Red arrows in the calculated area histograms point out what could be a peak that indicates the resistance data contains points for which multiple nanowires were measured.

two processes, as the area contribution to error for the 2x process was about a quarter of 1x process. This is due to improved regularity of pore area leading to a tighter area distribution with a better gaussian fit. Further improvements to pore size control would continue to lower the error. The error analysis presented here points to some of the first tweaks to be made in order to make more robust measurements of resistivity.

Table 3.4: Resistivity Estimate Contributions to Error

Fabrication Process	1x Anodization	2x Anodization
Area Contribution $(\Omega - nm)^2$	81.4	19.5
Resistance Contribution $(\Omega - nm)^2$	249	169
Length Contribution $(\Omega - nm)^2$	5.8	7.3
Calculated Resistivity $(\mu\Omega - cm)$	36 ± 26	25 ± 17

The resistivities estimated are much higher than the bulk resistivity of copper at 1.46 $\mu\Omega - cm$. To some extent, this is expected due to the polycrystallinity of the nanowires and the low diameter. Additionally, the contact resistance is included in these calculations, and this would increase the measured value compared to a real value. Still, the estimated resistivity is much larger than what is expected using FS theory, which would be 4.5 $\mu\Omega - cm$, when the values used for the initial values calculations were used. There are other theories that may be closer to the experimental value that generally produce higher resistivities by taking into account the quantum behavior at the nanowire edge [20]. However, to use these other theories, the scattering type must be known to determine the mean free path. Further improvements to this method are discussed in the future work.

3.3.4 Behavior of Integrated Magnetic Nanowires

Hysteresis curves of the in-template wires (Fig. 3.11) were measured parallel and perpendicular to the applied magnetic field. For a porosity of about 12% about 210 μg of Ni NWs were estimated to be present in the sample. Because the magnetic anisotropy of the nanowires is parallel to the long axis of the wire, the coercivity is expected to be larger when the applied field is parallel to the axis compared to perpendicular. The coercivity of the NWs measured the the applied field parallel to the wires w 38.8 mT

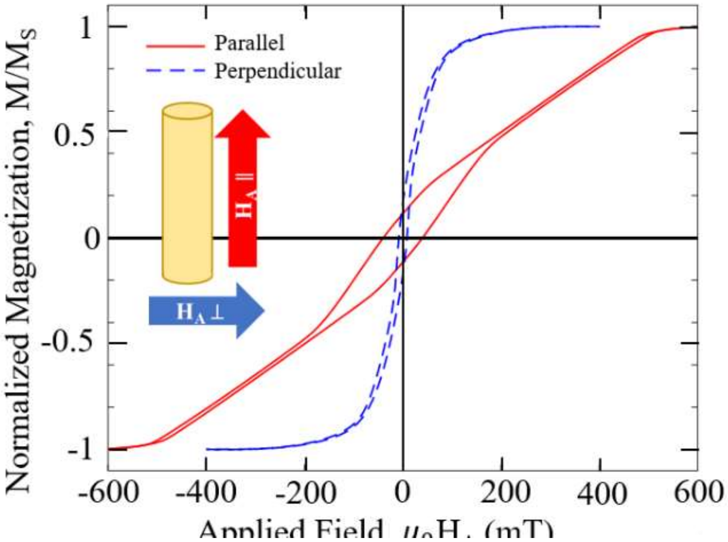

Figure 3.11: The hysteresis loops of vertically integrated NI nanowires with the field applied parallel (red, solid) and perpendicular (blue, dashed) to the long axis of the MNWs is shown.

and perpendicular was 8.3 mT, which matched the expectation. However, there was a surprising amount of in-plane anisotropy (perpendicular to the vertically oriented nanowires), which can be seen in the comparatively lower slope of the parallel curve to the perpendicular curve in Fig. 3.11.

It is likely that the source of the in-plane anisotropy is a layer of Ni overgrowth or "mushrooms" present on the wafer surface. An example of the Ni mushrooms is shown in Fig. 3.12. The overgrowth is likely acting as a soft magnetic layer. In metals that are less mechanically hard than Ni, like the Cu used in the resistivity estimates, outgrowth can be easily wiped off. However, if overgrowth is to be removed for Ni NWs, milling, sanding, or wet etching may be needed. The outgrowth can be approximated by a porous film, which has an in-plane anisotropy. The irreversible switching field and the reversible switching field from the FORC data were integrated to extract hysteresis loops for the hard and soft components using the projection method [58], the results of which are shown in Fig. 3.13. The hysteresis loop for the hard component is more reflective of the NWs in the template, because some of the influence of the softer thin film has been removed.

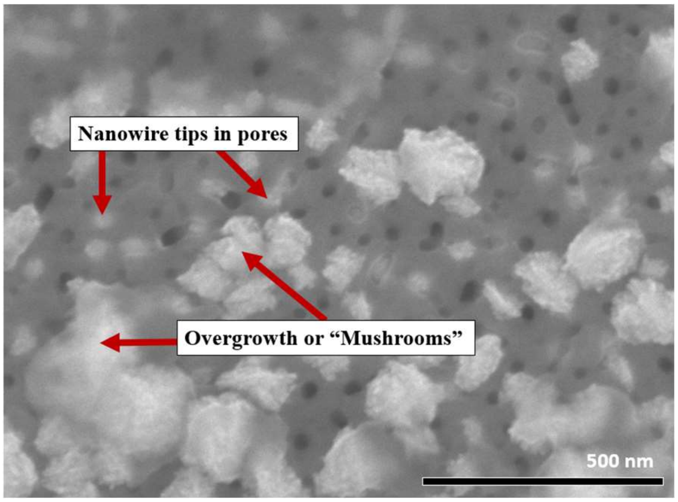

Figure 3.12: The porous AAO surface of the measured Ni NW sample is shown, highlighting regions where you can see the nanowire tip and overgrowth.

For comparison, an isolated Ni NW was simulated using a diameter near the mean measured diameter of the experimental Ni sample. The nanowire simulated in OOMMF (Object Oriented MicroMagnetics Framework) [72] specified a 1 μm long, 30 nm diameter cylindrical wire at a temperature of 0 K. The exchange parameter (A) was $9 \cdot 10^{-}12$ J/m, and a saturation magnetization of 490 kA/m. When the magnetic field was applied along the long axis, the resulting simulation demonstrated transverse domain wall propagation toward the center of the wire from the ends upon switching, and a coercivity of 118 mT. The simulation is shown in Fig. 3.14 for comparison with the measured major hysteresis loop and the integrated irreversible switching field.

When the measured major hysteresis loop is compared to the simulation and hard component hysteresis from the FORC data, it suggests that the interaction between the overgrowth and the nanowires significantly effects the magnetization and coercivity of the system. The coercivity of the full NW and overgrowth system was 80 mT less than the simulated value, compared to the 24 mT of the hard component which is much more likely to be largely explained by the experimental conditions and sample irregularities. The measured array of wires is expected to have shear due to NW interactions and the coercivity is expected to be lower due to thermal effects and polydispersity of the

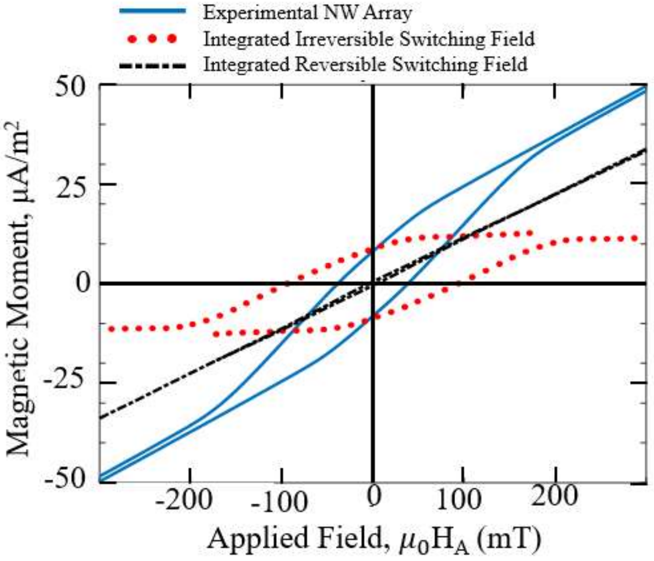

Figure 3.13: The major hysteresis loop (blue, solid), the hard component hysteresis loop extracted from the FORC data (red, points), and the soft component hysteresis loop extracted from the FORC data (black, dashed) are plotted.

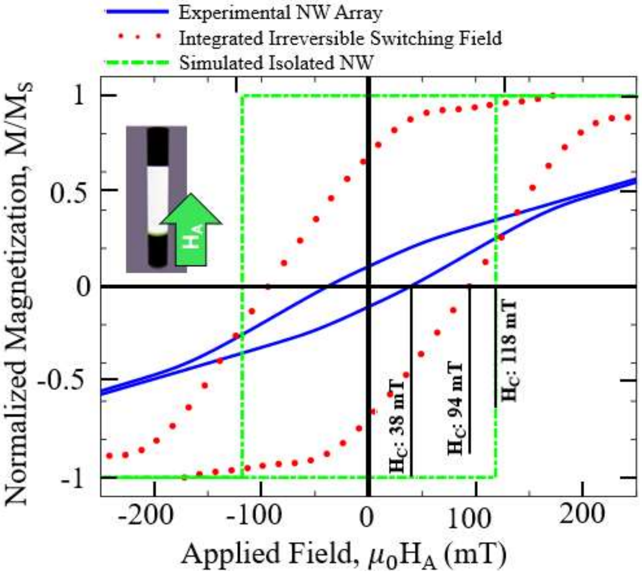

Figure 3.14: Simulation results are shown for an isolated 30 nm diameter, 1 μm long Ni NW (green, dashed). This is compared to the measured NW array of Ni NWs with a mean diameter of $28.7 \pm 6nm$ and a length of 1.3 ± 0.1 μm and the experimental integrated irreversible switching field (red, points). Inset is an image of the simulated domain wall propagation in the direction of the applied field.

NWs within the sample. With those experimental effects in mind, the hard component hysteresis is very similar to what you would expect from an array of nanowires of a size near 30 nm in diameter, as compared to Fig. 3.14, which is supported by the pore size measurements. Additionally, these findings emphasize that having overgrowth significantly affects the in-template wire properties, and should be etched back if you would like the system to retain behavior typical of MNW arrays.

3.3.5 Performace as Vias

The integrated Cu NWs were tested in high frequency coplanar waveguides for use as vias due to the potential for lower loss with less material required. Not only did the nanowires function as vias, but at some frequency ranges, coplanar waveguides with nanowires had less loss than the conventional copper via. Fig. 3.15 shows measured loss compared to a conventional waveguide spanning 10 MHz to 180 GHZ. For low frequencies, the waveguides featuring nanowire vias were comparable in loss performance to a standard waveguide. At frequencies above 60 GHz, the experimental waveguides were less lossy than the standard. During testing, there were no reported stability issues regarding the circuits with integrated nanowires. These results demonstrate potential for the use of Si-integrate vertical nanowires in high frequency devices.

3.4 Conclusions

It was demonstrated that vertical nanowires were stably integrated on silicon. Two variations of the AAO integration process were used, which came with different advantages. The 1x anodiziation process produces consistent lengths and has less process steps. However, to get finer control of the diameter and circularity of the nanowires, the modified 2x method is advantageous despite the increased number of process steps and poorer length control. When tested, not only was the AAO layer mechanically robust in its adhesion to the wafer, but it retained magnetic behavior of nanowires. If wire overgrowth is not removed, interactions between the wires and overgrowth layer produce a major hysteresis loop with reduced coercivity and a fat waist compared to a simple array of nanowires. The integrated NWs were able to be processed using standard wafer processing techniques after the nanowires were fabricated. These techniques include

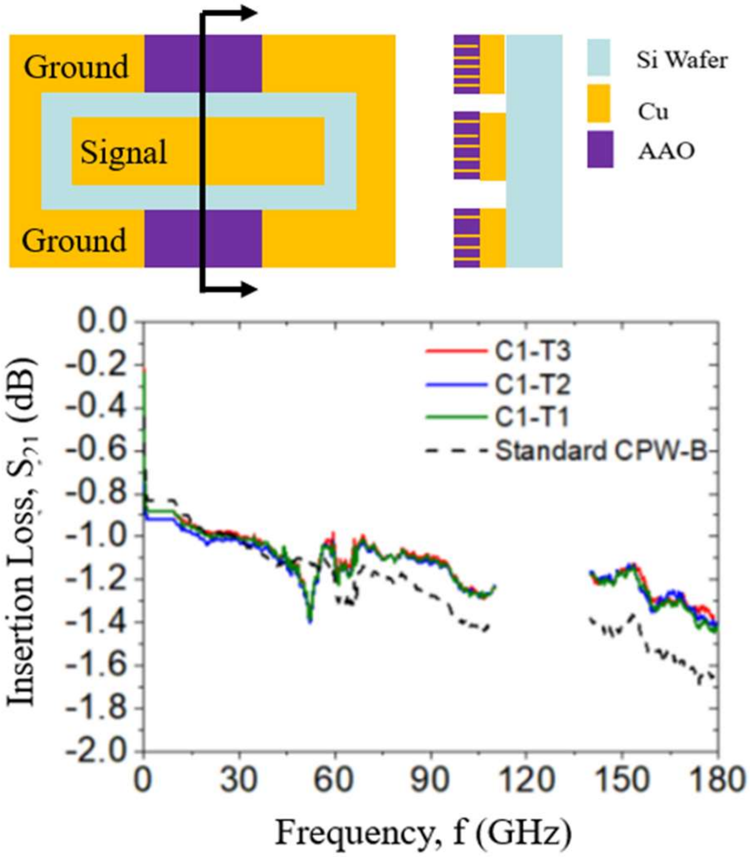

Figure 3.15: A schematic of the waveguide containing nanowires is shown (top). For the standard coplanar waveguide, the AAO/nanowire region is just copper. The insertion loss of the coplanar waveguide using NW interconnects is shown compared to a standard coplanar waveguide (bottom). Adapted from Dave, et. al [1]

photolithography, sputtering, and etching. The results presented here demonstrate and improve the ability for vertical nanowires to be used in silicon technologies.

3.5 Future Work

3.5.1 Processing and Geometric Control

In the future, expanding the dimensional range, improving control, and long range ordering of the wires are areas that are promising to explore. To expand the range of possible pore diameters, different anodization electrolytes and voltages should be tested. Improving the control of the 2x anodization method by altering the first anodization step and exploring imprinting patterns may be able to produce integrated AAO templates with long range ordering. For processing, further study is needed to firmly establish the temperature regime in which delamination will occur, and explore the possibility that surface modifications, slower ramp times, or the deposition of NWs will help inhibit delamination of the AAO at elevated temperatures. Furthermore, the fabrication of more devices can be attempted. All of this work could improve the versatility and processing capabilities of Si-integrated AAO.

3.5.2 Improved Resistivity Estimates

The method used to estimate the resistivity of the nanowires in-template has a large error associated with it. While improvements in pore size distribution will improve the precision of the resistivity estimates, there are other methods that should be explored. First, to improve understanding of and reduce the contribution the contact resistance makes to the resistance measurements, longer nanowires and nanowires with different oxide layer thicknesses should be measured. Longer nanowires would increase the contribution of the wire resistance to the total resistance, reducing the proportion of resistance from the contacts to the total. If this method is repeated with several wire lengths, a value for the contact resistance can be estimated. Different materials will also have different native oxide thicknesses, which will change the contact resistance. For example, the expected natural oxide layer of nickel is 3 nm [14], which is significantly less than copper's 10 nm [74] thick native oxide. After mitigating the contract resistance's contribution to the resistivity estimates, the next step to improving the accuracy is to collect enough data such that the peak for contacting only one wire can be separated out. As the peaks were beginning to separate at around 350 measurements, this may take a total of 400-600 individual resistance measurements. Making these measurements more precise will allow for more accurate simulation for high frequency applications and contribute to a better understanding of nanowire properties in-template.

Chapter 4

Ferromagnetic Resonance (FMR) Process Validation

4.1 Ferromagnetic Resonance Background

Ferromagnetic Resonance (FMR) is one of the phenomena where the geometry of MNWs contributes to a unique response. FMR occurs in ferromagnetic materials when an external, AC electromagnetic field is applied to the material at the same frequency at which the magnetic moment precesses about the axis of the magnetic field. This frequency is called the Larmor frequency [30]. The Larmor frequency is described by equation 4.1, where ω_L is the angular Larmor frequency, γ is the gyromagnetic ratio, and B is the magnetic flux density. The factors that most strongly effect the Larmor frequency are the g-factor, which is controlled largely by the material identity and quality [75], and the external magnetic field which contains both the applied magnetic field and the effective magnetic field which can change with shape and magnetic crystalline anisotropy. For an arbitrary shape, the FMR frequency v. applied field relationship is complex to calculate when all factors are taken into account, due to the complexity of B which is dependent upon the demagnetization factor (N), which is a tensor and a function of the sample shape.

$$\omega_L = \gamma \tilde{\mathbf{B}} \tag{4.1}$$

However, when working with thin films, spheres, or cylindrical nanowires, the demagnetization factor is reduced, allowing for a simpler, or at least analytically calculable, relationship for the resonance frequency. In this work, the nanowires take center stage, which - at sufficiently high shape anisotropy - can be modeled as an infinite circular cylinder. For the relevant applications, we are interested in an array of magnetic nanowires. Equation 4.2 [76] is an expression of the resonance frequency as a function of field for an array of MNWs, taking into account interactions between the nanowires, shape anisotropy, and crystalline anisotropy. Here, H_A and θ_H are the magnitude of the applied magnetic field and the angle of the field from the nanowire axis respectively, θ is the angle between the nanowire axis and the magnetization of the wire, and H_{eff} is the effective anisotropy field. It is H_{eff} (Eq. 4.3) [76] which takes into account most of the material parameters: this includes the saturation magnetization of the magnetic material (M_S), the fill factor of the wires in the template (FF), and the uniaxial crystalline anisotropy constant (K_u). When FMR experiments are performed with MNW arrays, generally the geometry and the applied field are controlled and γ values can be found in literature. Most of the interesting data lies within the H_{eff} term.

$$(\omega_0/\gamma)^2 = [H_A\ cos(\theta - \theta_H) + H_{eff}\ cos^2\theta] \cdot [H_A\ cos(\theta - \theta_H) + H_{eff}\ cos(2\theta)] \tag{4.2}$$

$$H_{eff} = 2\pi M_S(1 - 3 \cdot FF) + 2K_U/M_S \tag{4.3}$$

Using some assumptions, we can simplify these equations for the cases relevant to this work, which enables the H_{eff} term to be isolated. For the case where a magnetic field is applied parallel to the MNW axis, or in the out-of-plane (OP) orientation (shown in Fig. 4.1b), θ_H is set to 0. Because of the high shape anisotropy of the wires, you can also safely assume that the magnetization direction of the MNWs ($\tilde{\mathbf{M}}$) lies along the NW axis, which sets θ to 0 as well. Therefore, for the OP orientation, the Kittel equation simplifies to Eq. 4.4, where the frequency is a linear function of applied field and the H_{eff} term is contained within the y-intercept. If θ_H is at a low angle to the MNW axis, in most cases is still a reasonable assumption that $\tilde{\mathbf{M}}$ lies along the axis. This assumption is reasonable due to the unique shape of MNWs. Their shape creates a strong energetic preference for $\tilde{\mathbf{M}}$ to lie on the long axis, and this is typically only broken

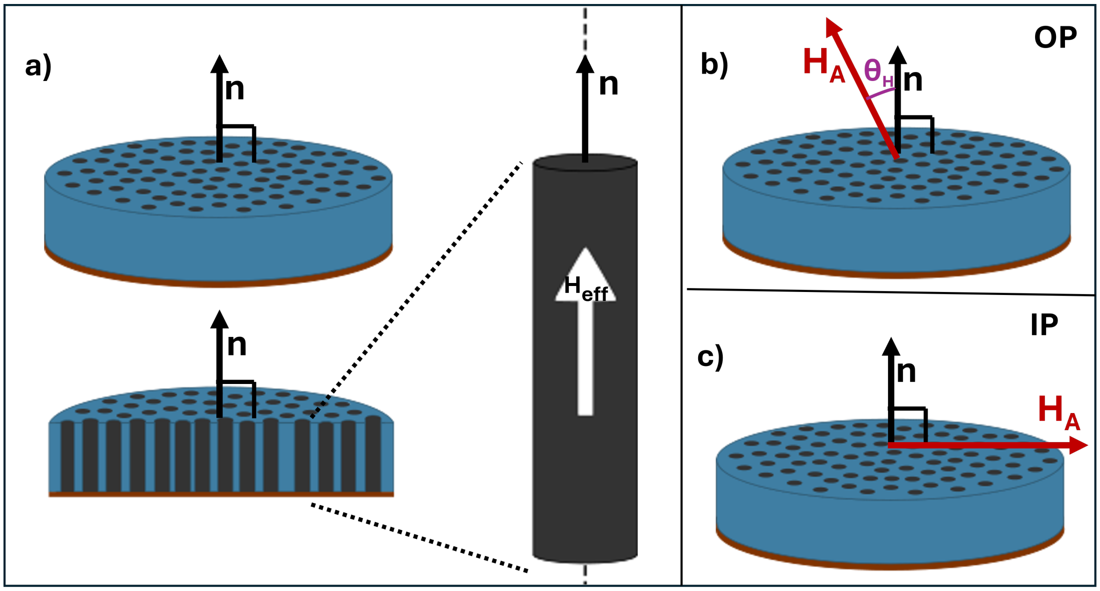

Figure 4.1: a) The vector normal to the template surface and parallel to the NW axis is shown for the template, template cross section, and lone wire. For most cases H_{eff} is along the wire axis. b) The vector orientation underlying Eqs. 4.4 and 4.5 are shown. c) The vector orientation for Eq. 4.6 is shown.

when there is a strong field component perpendicular to the wires or if there is significant crystalline anisotropy that makes other orientations more favorable. The applicability of this form of the Kittel equation has been demonstrated extensively in the literature [77]. In this work, a majority of measurements are made in the OP orientation due to both: the simplicity of the theoretical frequency-field relationship and the strength of the assumptions used to generate this relationship.

$$(\omega_0/\gamma) = H_A + H_{eff} \tag{4.4}$$

$$(\omega_0/\gamma) = H_A\ cos(\theta_H) + H_{eff} \tag{4.5}$$

The H_{eff} term may also be isolated when the field is applied perpendicular to the NW axis or in an In-Plane (IP) orientation (Fig. 4.1c). In this orientation, θ_H is $\pi/2$. When a low field is applied, the anisotropy field dominates, keeping the field along the NW axis. Therefore, when $H_A < H_{eff}$, it is a reasonable assumption that $\theta \approx 0$. Once the applied field exceeds the anisotropy field, it is only then that $\tilde{\mathbf{M}}$ will lie perpendicular to the NW axis, and $\theta \approx \pi/2$. The simplified form for both cases in the IP orientation is given in Eq. 4.6. When measuring the relationship of the frequency and field, H_{eff} should be the field where the FMR frequency approaches zero. While the assumptions regarding the direction of $\tilde{\mathbf{M}}$ are not as strong as in the OP orientation, experimental results demonstrate this relationship. However, the experimental results are less clear at low fields in the OP orientation than measurements in the IP orientation [78]. As such, the OP orientation was selected for measurements performed here.

$$(\omega_0/\gamma)^2 = \begin{cases} H_A^2 + H_{eff}^2 & H_A < H_{eff} \\ H_A(H_A - H_{eff}) & H_A > H_{eff} \end{cases} \tag{4.6}$$

As such, ferromagnetic resonance has been often used to measure the g-factor of new materials when in a simple shape [79, 80]. There are two general methods to measure ferromagnetic resonance. One is to place the sample in a resonant cavity, which measures the response at a single frequency. Then the applied magnetic field is varied to find the field at which the sample absorbs at the cavity frequency [79, 81, 82, 83, 84]. The other method is to mount the sample on or within coplanar waveguides or striplines, to which an external magnetic field is applied [85, 86, 87]. Either the frequency or the applied field is swept to determine the resonant frequencies [88]. In this work, the coplanar waveguide method was selected due to equipment availability and the ability to sweep the frequency.

FMR is a characterization tool to evaluate the quality of fabricated MNW arrays. Kittel theory is used to develop a theoretical basis that allows for both FF and M_S to be measured. In Kittel theory, arrays of magnetic nanowires, with an applied field aligned along the long axis, there is a linear relationship between the frequency and magnetic field, where the y-intercept contains most of the material parameters. This relationship can be measured using the coplanar waveguide measurement method, which is used and slightly modified to ensure that the template can be characterized entirely nondestructively. These relationships have been used to create an alternative means for process validation of MNW arrays, which can enable the quality control of scaled up MNW technologies.

4.2 Ferromagnetic Resonance for Process Validation

4.2.1 Introduction

One of the challenges when working to bridge the gap from laboratory to a manufacturable product is the ability to control the quality of the product. To produce a project reliably, you must be able to evaluate the fabricated product for compliance to your product tolerances reliably, quickly, and relatively cheaply. This is especially a challenge when working with nanotechnology, due to the scale of the devices. For nanowires, in Chapter 5, the tunability of magnetic nanowire properties was discussed as an advantage when it comes to designing MNWs to suit the needs of a given application. However, the same sensitivity that makes MNWs versatile also makes them sensitive to variation in processing. Therefore, applications that take advantage of the tunable nature of MNWs, also require tight production tolerances and good process control.

The process used to fabricate MNWs in this work, template-assisted electrodeposition, was selected due to its ability to control the MNW sidewalls and circular cylinder geometry, even when you make wires with a shape anisotropy that can exceed a long

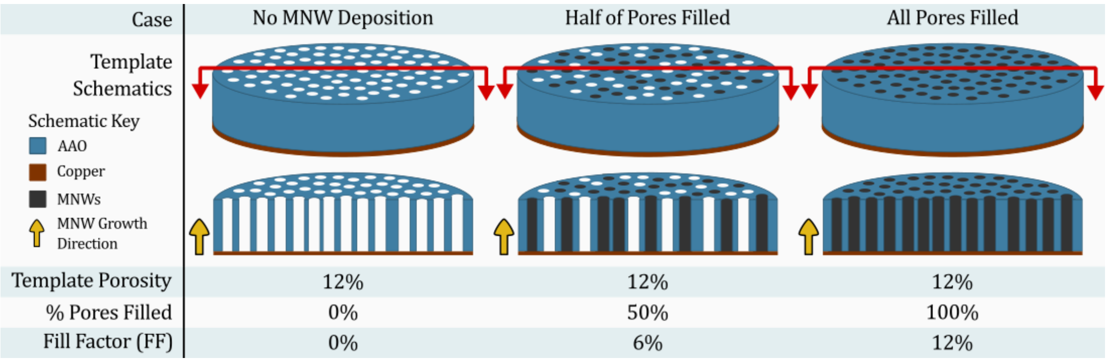

Case	No MNW Deposition	Half of Pores Filled	All Pores Filled
Template Porosity	12%	12%	12%
% Pores Filled	0%	50%	100%
Fill Factor (FF)	0%	6%	12%

Figure 4.2: Schematics show the relationship between template porosity, pore filling, and fill factor for the cases of 0, 50, and 100% pore filling.

axis to diameter ratio of 1000:1. This is not the case for techniques such as lithography/etching and performing synthesis in a micellear solution. This control over the circular cross section, wire diameter, and surface smoothness is critical to the performance of the MNWs, especially in applications that are sensitive to the NW resistivity, coercivity, and reactivity. However, drawbacks of this method can include uncertain lengths and fill factor (FF) within the pores. Fill factor is the porosity of the template multiplied by the percent of the pores that are filled, which is visually described in Fig. 4.2. Notably, uncertain FF can make it difficult to determine the yield and saturation magnetization of the MNWs grown in the template. This is an issue when it comes to scale up, because to measure M_S you need to know the volume of materials. The calculation of saturation magnetization (M_S), using the saturation magnetic moment (m_s), volume of NW material (V) is given in Eq. 4.7, and volume is further broken down into deposition area (A), mean wire length ($\bar{l}$), and fill factor (FF). Because M_S is a critical magnetic parameter that indicates both the quality of material and dictates the magnetic behavior of the sample, the inability to accurately determine its value makes it difficult to achieve the rigorous quality control needed for some applications.

$$M_S = m_s/V = m_s/(A \cdot \bar{l} \cdot FF) \tag{4.7}$$

Current methods to assess FF are typically qualitative or what may be considered semi-quantitative, because while quantitative measurement is possible, the cost of measuring FF accurately is high: in time, in money, and in the destruction or modification of samples. For example, you could etch back the template, and then take SEM images of small sections until you formed a representative sample of images, then use image processing to evaluate the percentage of pores filled. However, the etch modifies the sample - sometimes in a way that could be considered destructive for the application. Additionally, with the magnification required to resolve the pores, it takes a large number of images to form a representative sample, which is time consuming to take. The time consideration is amplified by the fact that imaging magnetic materials in an SEM requires adjustment of the astigmatism at each location due to the local magnetic fields. As an alternative, some works have assumed a given saturation magnetization and nanowire length, and used FMR measurements to estimate the FF. Sometimes, the FF is assumed to match the porosity of the template, which is understood to be an overestimate, and used to estimate the saturation magnetization [89, 90, 78]. Both these FMR methods are making strong assumptions about either the material properties or the quality and uniformity of the deposition.

Here, an analysis method is proposed in Section 4.2.2, which uses FMR, NW length, deposition area, and saturation magnetic moment measurements to quantitatively determine both FF and M_S. This method does not have to make the risky assumptions of the saturation magnetization matching the bulk or that all of the template pores were filled during fabrication. The analysis method is experimentally verified using two test cases. For the first test case, two FCC Cobalt MNW array with different FFs are compared. Once has been fabricated with a copper seed layer that improves FF, while the other was made without a seed layer. The FMR results for the two samples are then compared to qualitative and semi-quantitative methods of measuring FF, including EDX and FORC. For the second test case, a sample containing $\mathrm{Co_xFe_{1\text{-}x}}$ alloyed MNWs was tested to see if saturation magnetization from the FMR method was within error of the saturation magnetization predicted by the measured composition. The agreement of these results are used to assess the validity of the proposed analysis method.

4.2.2 Methods

Analysis to Experimentally Determine FF and M_S

Here, the Kittel relationships for templated MNWs detailed in section 4.1 are used to derive a relationship that allows for the measurement of FF and M_S without employing any destructive techniques. Measurements are taken with MNWs in the Out-of-Plane (OP) orientation, with the applied magnetic field oriented along the long axis of the MNWs, and therefore Eq. 4.4 is used as the starting point. In Eq. 4.8, Eq. 4.3 is substituted in for H_{eff}, and the relationship is put into point-slope notation. For clarity, the units of the saturation magnetization are included in square brackets.

$$f_{FMR} = (\gamma/2\pi)(H) + (\gamma/2\pi)(2\pi M_S[kA/m](1-3\cdot FF) + 2K_U/(M_S[kA/m])) \quad (4.8)$$

To simplify this relationship, it is assumed that the crystalline anisotropy contribution is insignificant compared to the geometric contribution, such that the term $2K_U/(M_S[kA/m])$ is negligible within H_{eff}. This is an assumption that is valid for typical allotropes of Ni and Fe, and primarily FCC Co, and gives Eq. 4.9.

$$f_{FMR} = (\gamma/2\pi)(H) + (\gamma/2\pi)(2\pi M_S[kA/m](1-3\cdot FF)) \quad (4.9)$$

Eq. 4.9 is a linear function between frequency and the applied field. The slope (m) of this relationship is $m = \gamma/2\pi$, which is constant for a given material and well known for the ferromagnetic transition metals. The intercept (b) of this relationship is $b = m\cdot 2\pi M_S[kA/m])(1-3FF)$., which contains the material parameters of interest: M_S and FF. We can simplify this and pull FF out of the parenthesis to get Eq. 4.10.

$$b = \gamma\ [FF\cdot M_S[kA/m]](FF^{-1}-3) \quad (4.10)$$

For templated MNWs, the value of $[FF\cdot M_S]$ can be experimentally determined, even if both FF and M_S are unknown. M_S is the saturation magnetic moment (m_S), normalized by the volume of magnetic material (V). For MNWs in a template, V can be estimated by $V = A\cdot\bar{l}\cdot FF$, where A is the area of the template in which nanowires were deposited, and $\bar{l}$ is the mean length of the MNWs. Substituting in the m_S/V for M_S is definitional, and the estimate for volume used, the expression for $[FF\cdot M_S]$ becomes Eq. 4.11, which can be reduced to Eq. 4.12.

$$[FF \cdot M_S[kA/m]] = FF \cdot m_S/A \cdot \bar{l} \cdot FF \tag{4.11}$$

$$[FF \cdot M_S[kA/m]] = m_S/A \cdot \bar{l} \tag{4.12}$$

All the values in the right hand side of Eq. 4.12 are experimentally measurable without the need to alter the MNW template and relatively quickly. The area can be controlled with a template and measured precisely using image processing. The saturation magnetic moment can be measured using a vibrating sample magnetometer (VSM). The mean length can be determined in a few ways. The nondestructive method would be to measure the total charge transferred during deposition, and convert that to the amount of material deposited. Theoretically, this computes directly, but in practice a calibration curve is typically required to determine a charge efficiency for the deposition conditions. For a more precise method, SEM/EDX can be used to measure the length of the nanowires and compute a mean value for the length. Understanding that we can measure $[FF \cdot M_S[kA/m]]$, and treating it as a known value, we can solve Eq. 4.10 for FF to yeild Eq/ 4.13.

$$FF = [b/(\gamma[FF \cdot M_S]) + 3]^{-1} = [b/(\gamma m_S/A \cdot \bar{l} + 3]^{-1} \tag{4.13}$$

Using Eqs. 4.12 and 4.13, you can determine M_S and FF experimentally, without having to rely on assumptions about either or modify the sample. All of these measurements have to ability to be automated and/or performed relatively quickly, which is a major advantage in a manufacturing setting.

In this study, b was determined using FMR (Section 4.2.2. m_S was taken from hysteresis loop measurements (Section 4.2.2). A was determined by the hole punch size (Section 4.2.2. $\bar{l}$ was determined using SEM/EDX, described in Section 4.2.2. Error values for M_S and FF were determined using the partial differential error propagation method and the errors in the measured values.

Nanowire Fabrication

For the test case using fill factor, two arrays of Co MNWs in AAO templates were produced for the process validation portion of this thesis. The process to make each sample was identical, except the "seeded" sample had an additional step before electrodeposition of the Co MNWs that deposited a thin Cu "seed" layer. A schematic of the seed layer is shown in Fig. 4.3. This seed layer was expected to increase the FF of the seeded sample compared to the sample without the seed layer. AAO (InRedox, Lot# 1853EP) with a nominal pore diameter of 40 ± 4 nm and a porosity of $12 \pm 2\%$ were used as templates. To prepare templates for electrodepositon, an electrical contact consisting of 7 nm Ti and 402 nm Cu were sputtered onto the templates. Before deposition, prepared templates were mounted to a rotating disk electrode using vinyl tape and the AAO surface was soaked in ethanol. A hollow hole punch with diameter of 10.2 ± 0.2 mm was used punch the hole in the mounting tape and control the area of the AAO template in which MNWs were deposited.

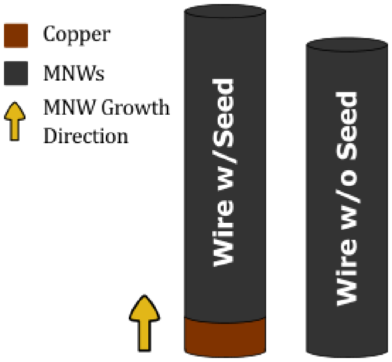

Figure 4.3: A schematic of a wire with (left) and without (right) a copper seed layer is shown.

The electrical potential used to deposit the MNWs into the template was controlled by a potentiostat (Gamry Interface 1010E), using cyclic amperometry settings. Each cycle consisted of a 1 s pulse each of a high and low voltage. For the sample with a Cu seed layer, a small layer of Cu was electrodeposited before the Co NWs. Only Co NWs were deposited on the other sample. The Cu seed was deposited by applying 60 cycles of -0.03/-0.08 $V_{Ag/AgCl}$ in a Cu electrolyte(0.3 M $CuSO_4$, 0.3 M H_3BO_3, pH 4). Co MNWs were deposited by applying 2600 cycles of -0.80/-0.85 $V_{Ag/AgCl}$ in a Co electrolyte (0.3 M $CoSO_4$, 0.3 M H_3BO_3, pH 2). For all electrolyte solutions, the pH was adjusted using H_2SO_4 and/or NaOH as needed. The pH of the Co electrolyte was specifically targeted to minimize magnetic crystalline anisotropy. Once electrodeposition was complete, the electrical contact was removed by floating the sample in 1.0 M $Fe(NO_3)_3$ etchant.

For the test case using composition, a sample with an unknown alloy composition fabricated by a prior student - Joseph Um - was used. The MNWs were electrodeposited into an AAO template with a nominal porosity of 12±2% and 40±4 nm diameter pores. A FeCo alloy was co-deposited into the pores in an unknown ratio. The reported length of the sample was 28.2 μm [89]. The MNW sample had been formed into a 6.2 x 1.4 x 0.55 mm chip. This chip consisted of the MNWs templated in AAO, (which was 50 μm thick), backed by 300 nm sputtered copper the side opposite the NW growth direction (which served the same function as our replaceable ground plane), and a 500 μm thick resin layer for stability. Because this sample had an unknown composition, which determines M_S, the FMR characterization method tested here was cross checked with a EDS data on composition to determine the validly of the results.

SEM/EDX

For the fill factor test, SEM/EDX was used to confirm the presence and geometry of the MNWs, validate composition, estimate the relative FF of the samples using composition ratios, and determine the mean length of the MNWs. Samples were prepared for SEM by mounting fracture surfaces on the cross section of the AAO template, then coating with 5.0 nm of carbon. Secondary electron and back-scattered electron images were taken at an accelerating voltage of 15.0 kV and a 0.35 nA current (Thermo Apreo 2S Lo-Vac SEM). EDX line scans were taken perpendicular and parallel to the nanowires with data collected at 100 nm intervals along the lines scan.

To determine the mean composition ratios and validate the MNW composition, perpendicular line scans were taken to determine the mean composition rations where nanowires were present (2 scans/site, at 4 sites). The concentration of Co was compared between samples to evaluate if there was a difference in FF between samples. The ratio of Al:O was compared at each site to evaluate if significant Co oxidation took place. To determine the mean length of the MNWs, line scan parallel to the MNW length were used (3 scans/site, at 4 sites) The length for each parallel scan was evaluated by taking the mean composition of Co determined by the perpendicular line scans, then finding the full width at half the mean composition. The average length of the MNWs is reported as the mean across all sites, presented with standard error.

For the composition test, SEM/EDX was used to determine the ratio of Co to Fe in the CoFe alloy sample. The surface of the chip where the MNWs were near the surface was measured using EDX. Spectra were taken at five points. At each point the atomic percent of Co and Fe were evaulated and the ratio of each compared to the sum was computed. Reported composition values are the sum mean values of the percent (need to re-phrase), reported with standard error.

Magnetometry

Hysteresis loops were measured to determine the saturation magnetic moment and evaluate the FF qualitatively for each sample. All measurements were performed using a vibrating sample magnetometer (VSM, Princeton MicroMag) at room temperature, calibrated using a Ni sphere. For each MNW array, hysteresis loops were measured at in the orientations where the field was parallel to the wire axis (OP orientation) and perpendicular (IP orientation), after the sample was saturated. OP hysteresis loops were measured using a step size of 0.400 kA/m (0.503 mT), a maximum applied field of 475 kA/m (597 mT), and an averaging time of 200 ms. IP hysteresis loops were measured using a step size of 0.750 kA/m (0.942 mT), a maximum applied field of 700 kA/m (880 mT), and an averaging time of 300 ms.

First-order reversal curves (FORCs) were collected for each sample to use as a qualitative evaluation of FF and sample quality. FORCs were measured using a VSM (Princeton MicroMag), with the sample mounted in the OP orientation. For each sample, 183 FORCs were taken, using and averaging time of 400 ms with a 500 ms pause time at the reversal field. FORC distributions were plotted using FORCinel [91] with slope correction, lower branch subtraction, and a smoothing factor of 4.

X-Ray Diffraction

X-Ray Diffraction (XRD) was used to confirm the material identity of the sample and to evaluate the validity of the assumption that no significant magnetic crystalline anisotropy is present. A diffractometer (Bruker D8 Discover) with a Co source ($K_\alpha \lambda = 1.789$ Å) was used to measure the samples, mounted on a Si wafer such that the template side where the growth originated was nearest to the measurement surface. For each sample, a coupled scan with three frames was performed. Frames were centered at 2θ values of $44.5^o, 64.5^o$,and 84.5^o with ω values of $22.25^o, 32.25^o$,and 42.25^o, respectively. Each frame had width of 20^o 2θ and were measured for 1200 s. During analysis, frame scans were integrated over a constant angle ($\chi = 18.4^o$), then merged, taking the maximum intensity value at overlapping points. To identify peaks, data were compared to the powder diffraction patterns in cif file numbers 9008492 (HCP Co), 9008466 (FCC Co), and 4105040 (FCC Cu) from the Crystallography Open Database [92].

Ferromagnetic Resonance

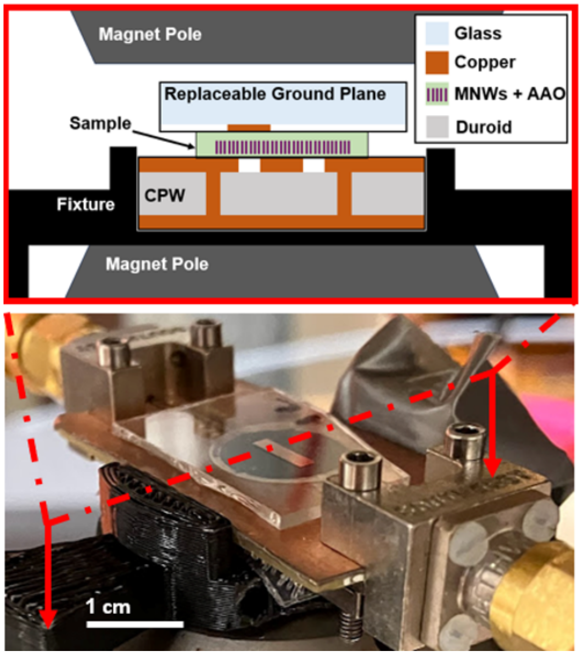

Figure 4.4: An image of the FMR measurement setup is shown (below). A schematic of the cross section (above) shows the relative location and materials of the sample, replaceable ground plane, and co-planar waveguide.

FMR measurements in this section were taken collaboratively with Alex Wege and/or Md Toaha Anas from Dr. Rhonda Franklin's group for the fill factor test case. Measurements taken for the composition test case were taken by Md Toaha Anas. Data analysis was done by the author.

The FMR response of a MNWs array was measured using a coplanar waveguide.

The common method of modifying the sample or embedding the MNWs in the coplanar waveguide was not used. Instead, a replaceable Cu ground plane was fabricated and placed on top of the MNWs, over the gap. This replaceable ground plane was fabricated by sputtering a 200 nm thick Cu film onto a glass slide, with tape used as a mask for handling. The glass was scribed and cut so that the Cu region was restricted to a 1.5 x 6 mm strip. The measurement setup is shown in fig. 4.4, and has the advantage of being nondestructive to the sample and not requiring additional processing steps to take the measurement. More precisely, MNW samples (fabrication detailed in section 4.2.2) was placed across the striplines of a two-port grounded coplanar waveguide, and the replacable ground plane was set on top of the MNW array. Non-magnetic cables (Cinch Connectivity Solutions) and 2.4 mm connectors (Southwest Microwave) were used to connect the waveguide to the vector network analyzer (VNA).

Data were collected at constant DC field vaules while the frequency of the applied AC - or excitation - field was swept. The DC magnetic field was applied in the OP orientation by an electromagnet, for approximate values of $4\pi H_{DC}$ at 0.40, 0.35, 0.30, 0.25, 0.20, 0.15, 0.10 T, and with the electromagnet power off. To ensure reproducibility, data points were taken after saturating the MNWs in a high magnetic field, and taking data points from highest field to lowest field. More precise magnetic field values used during analysis were determined using a calibration curve relating the applied current to the applied field, created for the pole gap used and measured using a gaussmeter. The excitation field was applied using the VNA (Anritsu 3769D), which also measured the S parameters as the frequency was swept from 10-40 GHz. Four data sets were measured for each sample, with the position of the replaceable ground plane changed slightly each time.

The resulting S_{21} data were imported into MATLAB, normalized to the zero-current measurement, and scaled to find the FMR frequency at each applied field. Data points too near a resonance from the measurement setup were excluded. After plotting the frequency-field relationship for each trial, a linear regression was performed to determine the slope and intercept. Mean intercept values for each sample are reported with the calculated standard error.

Additional data were collected by Anas for a chip containing CoFe that was fabricated by Joseph Um. The same measurement set-up was used as the Co MNW arrays, except that the replaceable ground plane was not needed, due to the presence of a deposited copper layer on the sample itself. Data collected for a range of $4\pi H_{DC}$ at 0.20, 0.15, 0.10, 0.05, 0.005 T, with one measurement at each data point. Data collected here was analyzed according to the method described in Section 4.2.2. To evaluate the validity of the method, the $\mathrm{M_S}$ from FMR was compared to the $\mathrm{M_S}$ determined using the composition from EDS and a phase diagram [2] of $\mathrm{Co_{1\text{-}x}Fe_x}$.

4.2.3 Results

Test Case: Fill Factor

For this test, the samples measured were both FCC Co MNWs in an AAO template, made under identical conditions except that the sample with a seed had a layer of Cu deposited before the Co. The seed layer was excepted to increase the FF of the MNWs in the template, which created a test case to see if the method in section 4.2.2 was precise enough to detect a difference in the samples. More data was collected than required to determine FF and M_S from the FMR data. Additional measurements were made to validate the geometry and composition of the MNWs, to ensure that the assumptions made to derive Eqs. 4.12 and 4.13 were reasonable. Lastly, a wide array of qualitative or semi-quantitative measurements were used to evaluate the relative FF of the samples in order to confirm - or reject - the validity of the FMR results. In this way, we determined the validity of this nondestructive method to evaluate FF and M_S of a MNW sample.

SEM and EDX data were collected as described in section 4.2.2. Back-scattered Electron (BSE) images, along with EDX, verified the mean length of the MNWs from template fracture surfaces (Fig. 4.5a). The average length of the Co MNWs, excluding the Cu, was determined to be 13.5 ± 0.1 μm and 12.6 ± 0.1 μm for the samples with and without the seed layer, respectively. BSE images show that the seeded sample has a more irregular fringe at the top of the nanowires (or end opposite the origin of growth). The irregular fringe was confirmed by the EDX measurements along the length of the MNWs (Fig. 4.5b), which show a longer drop off in the Co composition for the seeded sample than the sample without the seed. The dropoff in composition at the end of the wires measured at 2.3 ± 0.2 μm and 0.98 ± 0.2 μm for the sample with and without the seed respectively. The increased length range of the seeded sample is below the length

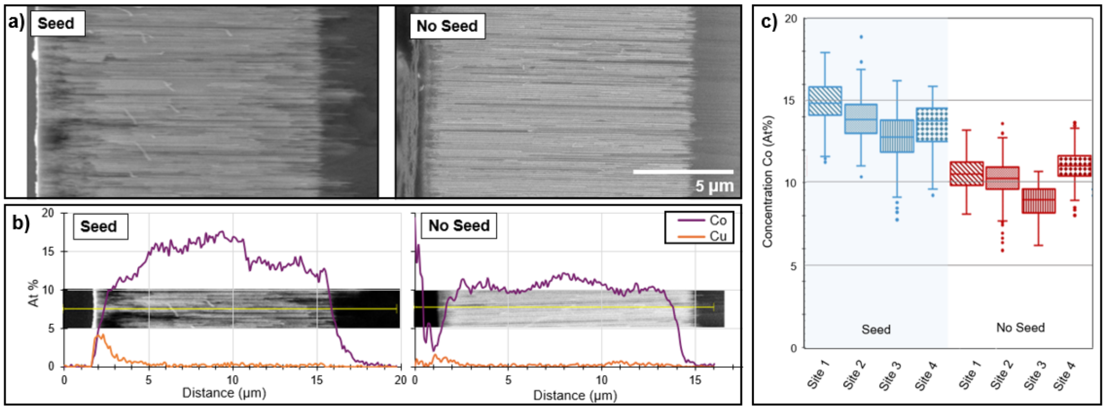

Figure 4.5: (a) BSE images of fracture surfaces are shown for the sample with (left) and without (right) a seed layer, oriented such that MNW growth originated on the left hand side and grew towards the right. (b) Sample EDS line scans are shown for the two locations shown in the background. (c) Box and Whisker plot show the distribution of measure Co concentration for each site.

range of the Cu seed (up to 1.98 ± 0.05 μm. From this, it is likely that the increased dispersion in total length is due to pores being seeded with variable lengths of Cu, with some containing little to no Cu, and not due to a significant change in the spread of Co MNW lengths compared to the sample without the seed. Additionally, EDX data from the sample without the seed showed a thin Co layer at the back contact, indicating electrolyte etching of the pack contact with subsequent deposition of Co perpendicular to the MNWs.

The mean composition of each site was found using EDS data collected perpendicular to the MNW axis. The atomic ratio of AL:O was measured to be 2:3 at all sites measured, validating that no significant Co oxidation took place. The lack of Co oxidation supports that the value of $4\pi M_S$ should be near the known value for Co, 1.68-1.73 [93]. The Co composition at each site (Fig. 4.5c) demonstrates that the concentration of Co was higher for the seeded sample. However, while EDS is a good method for comparison and confirmation, when it comes to the composition of complex sample such as nonconductive templates containing nanoparticles, the values reported should be considered semi-quantitative. Meaning, these results support that the seeded sample has a higher concentration - and therefore FF- of Co in the template, the values do not accurately measure the real concentration, just the relative concentration.

Another way we can use the data collected using SEM/EDX to evaluate the relative fill factor is to compare the measured length ($\bar{l}$) to the length predicted based on the charge transferred during deposition for the nominal template porosity($\bar{1}_{est}$). The length efficiency ($\bar{l}/\bar{1}_{est}$) was 0.41 and 0.50 for the sample with and without the seed. If you assume that the real efficiencies were the same (because reaction conditions were identical) and that the discrepancy in efficiencies comes solely from the difference in FF, and that the FF of the seeded sample is near the nominal template porosity (12%), you can compute an estimate for the FF for the sample without the seed at 9.8%. 9.8% is likely an overestimate for the fill factor of the sample without a seed due to the thin layer of Co found to be deposited perpendicular to the wires on the sample without a seed. While assumptions had to be made that make these numbers quantitatively unreliable, the efficiency values do provide additional support that the sample with the seed has a larger fill factor than the ample without the seed.

Measured magnetic parameters corroborate the FF estimate from lengths by indicating there is a difference in the samples that demonstrably affects the magnetic behavior of the templates. Measured hysteresis loops are shown in Fig. 4.6. Normalized curves (Fig. 4.6a) allow for a comparison of coercivities and loop shape, while the curves in Fig. 4.6b allow for a comparison of the saturation magnetic moment (m_S), the value of which is needed to calculate the porosity from the FMR data. Coercivities (H_C), remanent magnetic moment (m_R), and m_s are given in Table 4.1. Note that the difference between saturation magnetic moments ($\bar{m}_S$) of the samples is $57\mu A \cdot m^2$, with the larger $\bar{m}_S$ (177 ± 15 $\mu A \cdot m^2$) measured in the seeded sample. Since it was verified by EDS that neither sample is significantly oxidized, this indicates that more magnetic material is present in the seeded sample, likely resulting from increased length of the nanowires and/or increased FF.

FORC plots (Fig. 4.7) provide qualitative information on the distribution of coercivities and the the interactions between MNWs in a template. The spread of the interaction fields ranges from over $\pm 250mT$ on the seeded sample, while the other sample ranged nearer to $\pm 200mT$. The decrease in MNW interaction points to a lower FF without the seed layer, because wires further apart interact less. Additionally, the range of coercivities on the wires is similar in both samples: from just over 100 mT

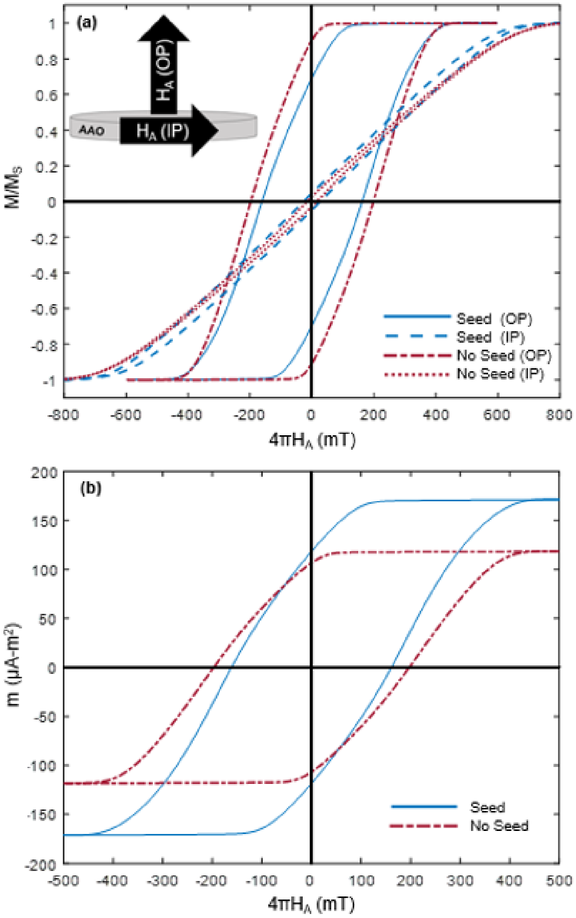

Figure 4.6: (a) Normalized hysteresis loops for both samples are shown int he IP and OP orientations, with orientations described in the schematic. (b) Hysteresis loops are compared for the OP orientation with the measured magnetization.

to about 450 mT, indicating the wires themselves are not drastically different. FORC results are generally considered semi-quantitative, with some known artifacts in vertical MNW arrays [94][57][95][96], but agreement among different techniques - SEM/EDX, hysteresis measurements, FORC, and XRD - lends credibility to the results.

XRD spectra (Fig. 4.8) were used to determine if the the assumptions made in section 4.2.2 of negligible magnetic crystalline anisotropy were reasonable and to determine if any differences in the crystal structure arise when a seed layer is used during fabrication. Both samples were found to have the same peaks present, excluding the addition

Table 4.1: Magnetic parameters obtained from hysteresis loops

Sample	Seed		No Seed	
Orientation	OP	IP	OP	IP
$4\pi H_C$ (mT)	160.8 ± 0.3	27.0 ± 0.5	197.7 ± 0.3	16.0 ± 0.5
m_R $(\mu A \cdot m^2)$	118.5 ± 0.1	8.8 ± 0.1	106.7 ± 0.1	3.5 ± 0.1
m_S^* $(\mu A \cdot m^2)$	170.5 ± 0.1	183.4 ± 0.1	117.8 ± 0.1	122.7 ± 0.1
$\overline{m}_S^{**}(\mu A \cdot m^2)$	177 ± 15		120 ± 2	

[*] Note: m_S (saturation magnetic moment) is not equivalent to M_S (saturation magnetization).

[**] The reported error on the average m_S is standard error

of the small - and expected - Cu peaks in the seeded sample. Therefore, the spectra demonstrate that Co MNWs have similar structures regardless of the presence of a Cu seed layer during fabrication. Both HCP and FCC Co grains appear to be present, but the FCC pattern dominates at the 2θ range measured. Because the ratio of FCC to HCP grains is expected to be high due to the pH of the electrolyte used in fabrication [29, 97, 98], the majority FCC pattern in expected. Some crystal texture is indicated by the variation in the peak ratios from the powder diffraction patterns. Variations in the peak height and peak ratios indicate there is some difference in the relative amounts of FCC/HCP grains and difference in the crystal texture between the samples. While not definitive, the XRD results support the assumption used in FMR analysis that the crystalline anisotropy is negligible with respect to the shape anisotropy of these wires. For the crystalline anisotropy to be significant enough to break down that assumption, grains would need to be well-aligned and primarily HCP which is not the case.

Finally, we present the FMR measurements, which allow us to quantify both the FF and M_S, in contrast to all the methods presented previously. Here, FMR resonances were determined by the frequency at which the normalized S_{21} data hit a minimum that did not correspond to a system resonance. In Fig. 4.9a an example trial is shown for each sample, comparing the measured response to the expected response given from the Kittel eqauation if the FF is 12% and $M_S/4\pi$ is 1.7T. Generally, we found that this method has a low signal when a small or no magnetic field is applied. Therefore, the intercept of the f(H) relationship was determined using a linear regression instead

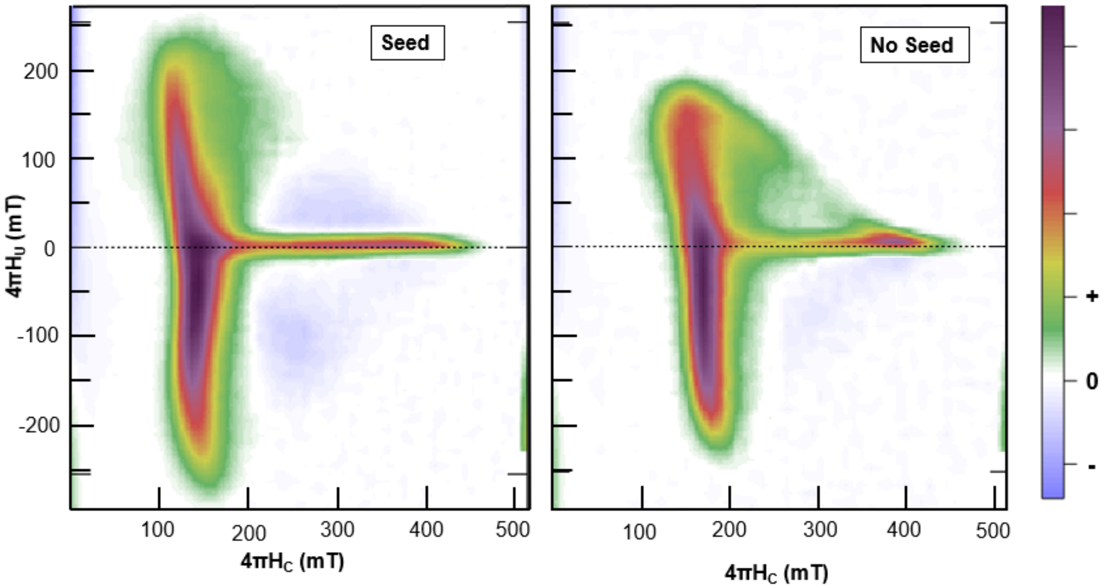

Figure 4.7: FORC plots for the seeded sample (left) and the sample with no seed (right) are given in arbitrary units on for the FORC parameter.

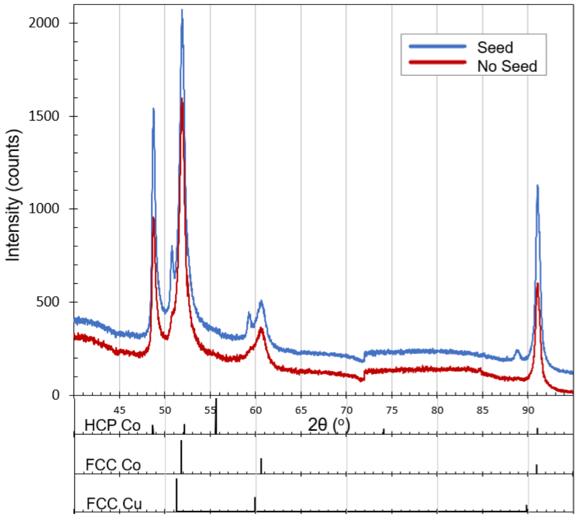

Figure 4.8: XRD spectra are given, with the seeded sample offset by +100 counts for clarity. For comparison, the powder diffraction spectra for HCP Co, FFC Co, and FCC Cu are plotted below.

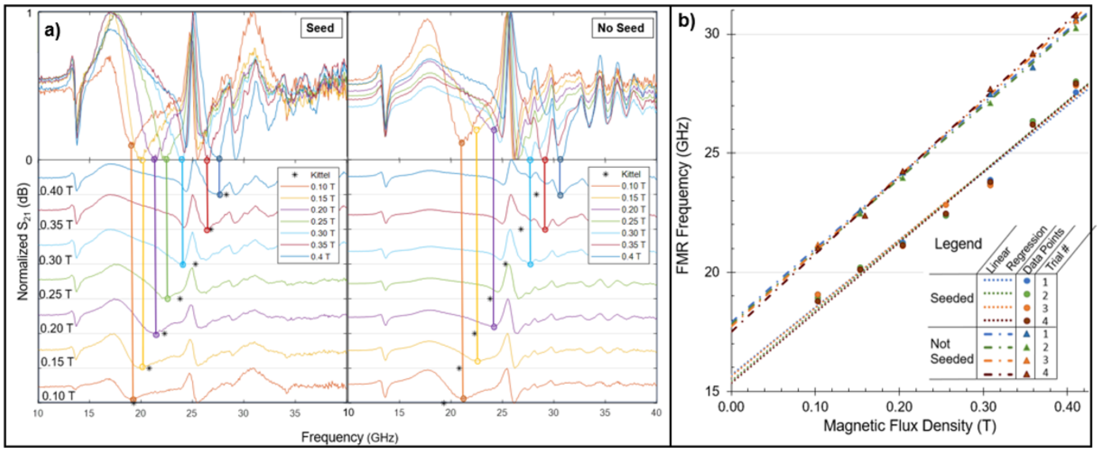

Figure 4.9: (a) normalized S_{21} curves are shown for each data point for trial 1 of the sample with the seed (left), and trial 4 for the sample without the seed (right). The bottom plots separate all the curves for clarity. Experimentally determined FMR frequencies are marked by the circles on each curve. Kittel predictions for the MNWs with a FF of 12% and $M_S/2\pi$ of 1.7 T are marked by black stars. (b) FMR frequency as a function of the applied field is shown with the linear regressions for each trial.

of directly measuring the FMR frequency at a applied field of 0 or near 0. The data with linear regressions are shown in Fig. 4.9b, and the slope and intercept of each trial is given in Table 4.2.

The slopes of the linear regressions can help confirm the validity of the measurements. There should not be significant variation of the slope from the theoretical value for Co (30.0 GHz/T), since we have confirmed that the samples consist of Co MNWs with little to no oxidation through XRD and EDX. For the seeded sample, the mean slope was 28.9 ± 0.3 and without the seed the slope was 31.3 ± 0.5 A slope lower than the expected value can be partially due to small angles in the field relative to the MNW axes. However, a slope larger than 30 is not physical if you only account for small angle field deviations, and is due to the pole gap being smaller than when the calibration curve was measured. The deviations from the theoretical value reported here is most likely due to discrepancies in the electromagnet's pole gap from the calibration curve. Since the pole gap was not significantly adjusted for different trials on the same sample, but was opened up between samples it makes sense that the slopes are more consistent

Table 4.2: FMR Results Summary

Sample	Seed				No Seed			
Trial	1	2	3	4	1	2	3	4
Slope (GHz/T)	28.2	29.3	28.6	29.5	30.6	30.6	31.6	32.5
Intercept (GHz)	15.7	15.4	15.6	15.4	17.9	17.8	17.7	17.5
Mean Slope (GHz/T)	28.9 ± 0.3				31.3 ± 0.5			
Mean Intercept (GHz)	15.54 ± 0.08				17.75 ± 0.09			
Measured $\overline{m}_S^{**}$ ($\mu A \cdot m^2$)	177 ± 15				120 ± 2			
Measured $\bar{l}$ (μm)	13.5 ± 0.1				12.6 ± 0.1			
Measured D (mm)	10.2 ± 0.2				10.2 ± 0.2			
Calculated FF (%)	12.3 ± 0.4				9.0 ± 0.4			
Calculated $\mathrm{M_S}/4\pi$ (T)	1.64 ± 0.10				1.62 ± 0.13			

in the same sample than between samples.

It is the y-intercept of the f(H) relationship that contains the physical information we care about for these samples. The mean intercept (b) was found to be 15.54 ± 0.08 and and 17.75 ± 0.09 for the samples with and without the seed, respectively. Along with the y-intercept of the f(H) relationship, the measured values for saturation magnetic moment, mean wire length, and deposition diameter were inserted into Eqs. 4.13, 4.12, and the equation for a circle to compute measured values for FF and M_S with propagated error. The values and errors used to compute FF and M_S are reported in Table 4.2, along with the computed values.

The FF of the seeded sample was determined to be $12.3 \pm 0.4\%$. This aligns with expectations for a sample fabricated using a seed layer, as it is within the error range of the nominal template porosity ($12 \pm 2\%$). The fill factor for the sample with no seed was determined to be $9.0 \pm 0.4\%$. The FF being a few percent lower than the seeded sample matches the qualitative observations from EDS (Fig. 4.5) and the lower interaction fields from the FORC plots (Fig. 4.7). The measured FF on the sample without a seed is also near, but below, the FF estimated from length efficiency, which was 9.8 % and expected to be high.

This method also produces a computed value for M_S, which serves as an additional way to confirm results or as the desired measured quantity itself. $M_S/4\pi$ calculated from the FMR measurements is $1.64 \pm 0.10T$ and $1.62 \pm 0.13T$ for the samples with and without a seed layer. The measured values are within error of the M_S reported for pure Co in literature, 1.68-1.73 T [93]. Additionally, both measured values are near each other, which should be the case as they are the same material. It is worth noting that the error is fairly high.The error propagation method has the advantage of telling you which contributing measured value is contributing the most error to the end result. A significant portion comes from the deposition diameter of the template. If a more precise method is used to measure the deposition area, such as image processing, this error will decrease, giving a more precise result. Additionally, the error in the magnetic moment at saturation is significant because the value used was the average of the IP and OP measurements. As the VSM was calibrated with a sphere, these measurements are expected to produce different results due to the difference in geometry - some of the material is closer to the pickup coils. This can be improved with a different calibration method.

Test Case: Composition

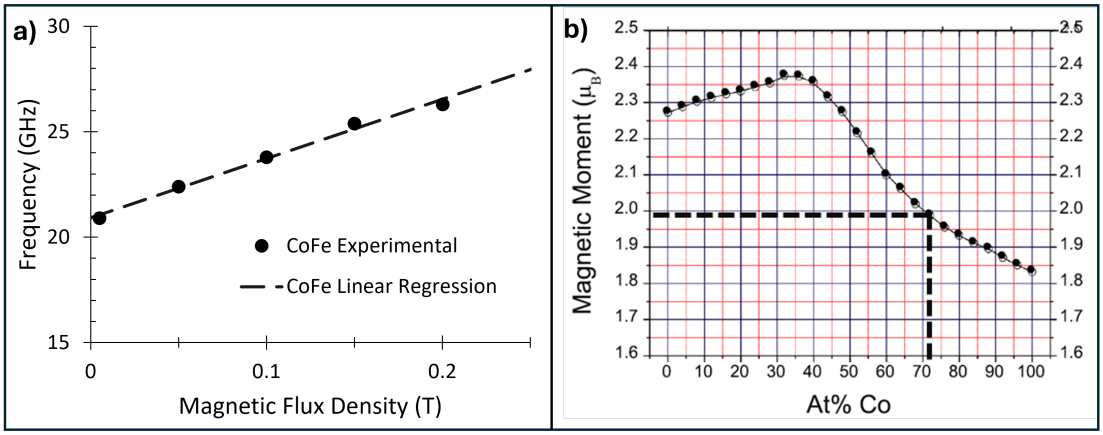

Figure 4.10: a) The experimental FMR peaks are plotted with the linear regression for the CoFe sample. b) The phase diagram (adapted from [2]) is marked to show the expected magnetic moment at the composition measured using EDS.

For this test, the sample measured was a chip containing an array of $\mathrm{Co}_{(1\text{-x})}\mathrm{Fe}_{\mathrm{x}}$

MNWs, where x was unknown. FMR results are shown in Fig. 4.10a. From the intercept of the linear regression, the $M_S/4\pi$ was found to be 2.18 ± 0.21 T. Using EDX, the relative composition of Co and Iron int the $\mathrm{Co_{(1\text{-}x)}Fe_x}$ alloy was found. x was determined to be 0.28 ± 0.04, making the alloy composition $\mathrm{Co_{0.72}Fe_{0.28}}$.The magnetic moment determined using the phase diagram in Fig. 4.10b. was about $2.0\mu_B$, which was converted to saturation magnetization by multiplying by the bohr magneton and estimated number of atoms per volume. The EDX results estimate gives $M_S = 2.15 \pm 0.04$ T. The results given by the FMR results and the composition results are within error of each other. This gives an additional confirmation of the FMR characterization method.

4.2.4 Conclusion

In this chapter, a method for characterizing the FF and M_S of MNW arrays was proposed, the theory presented, and the method experimentally validated. The method is nondestructive and uses FMR that does not require modification of the sample along with length and saturation magnetic moment measurements to calculate the FF and M_S simultaneously. Two routes were used to verify the method. First, two cobalt samples with the method varied to produce two different FFs were compared. The proposed non-destructive FMR method was used to determine quantitative values for the FF and M_S of each array, then compared with numerous qualitative and semi-quantitative methods. To provide an additional test of the characterization method, a MNW array of a CoFe alloy was used to validate the method through comparing the saturation magnetization determined by FMR with literature values for the alloy with the measured composition. Both tests indicate that the FMR method produces reliable, quantitative results for both FF and M_S.

Not only are the results reliable, but this method has significant advantages when compared to other methods of assessing sample quality. One of the major advantages of using FMR to evaluate the sample quality is that the M_S and FF measurements are decoupled. If you try to determine either the M_S or FF using hysteresis and mass measurements, a low saturation magnetic moment may mean either that the sample has a M_S or low FF. With the method reported here, you can extract one from the other. However, they are still inversely related such that the value of one provides a check for the reasonability of the other. If either M_S or FF have a physically unreasonable value, there is an immediate sign that the measurement should be reevaluated or that the assumptions surrounding the nanowire geometry and negligible magnetic crystalline anisotropy have been violated. An example of unreasonable values would be if M_S exceeds that of the pure metal or if the FF is higher than the template. The decoupling of M_S and FF, combined with the nondestructive nature and reasonably low cost needed for this method make it not just a viable method to quantitatively evaluate the quality of templated MNWs, but potentially the best method to quantitatively evaluate the quality of templated MNW arrays.

4.3 Future Work

4.3.1 Deviation from Theory in Nickel

The primary loose end in this work is the behavior of Nickel MNW arrays. Nickel is the only material tested where the FMR behavior does not agree with the Kittel prediction for a given fill factor, and it repeatably deviates from expectation. When 40 and 120 nm diameter wires were tested using the same procedure, the arrays behaved as if the magnetic moment was significantly higher or the fill factor was significantly lower than expected. Fig. 4.11 shows the data collected for Ni compared to the predicted trend. The differences are far larger than can be explained by a poor fill factor, especially for Ni which was deposited with a slow deposition rate. This significant of a deviation means that the Nickel is doing something interesting at the materials level, such as being uniformly strained such as to produce crystalline anisotropy or the formation of a phase not typically seen at room temperature such as HCP Ni. The difference from theory is much larger for the 40 nm diameter wire array, which indicates that this is likely a size-based effect.

The next steps to elucidate the cause of the increased apparent M_S are:

1. Compare the XRD data of the MNW arrays to other Nickel phases, including metastable ones.

2. If there are matches for alternative phases, compute the expected FMR behavior based on the saturation magnetization of that phase. Take into account potential

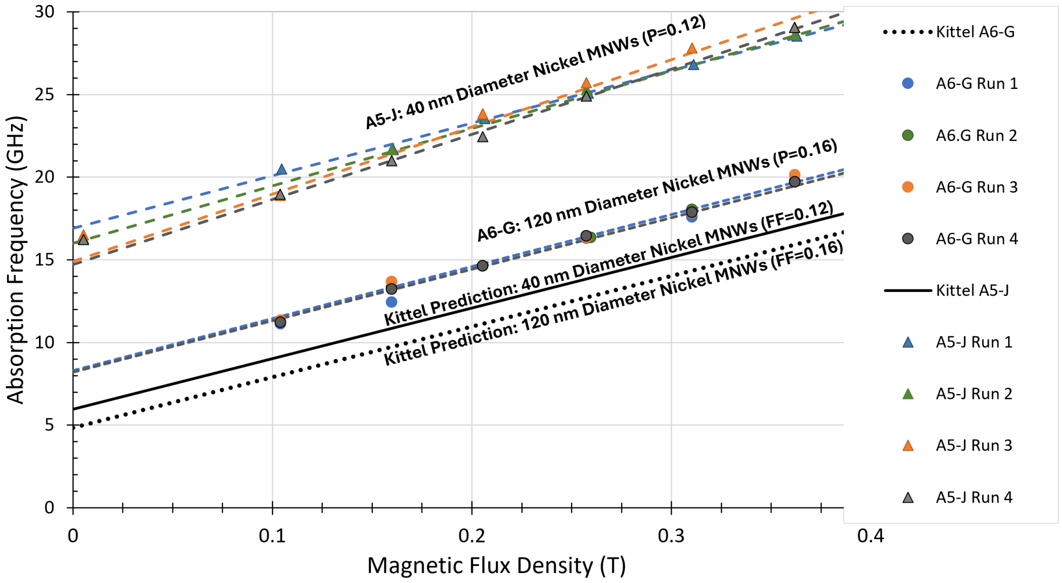

Figure 4.11: FMR response with applied field for Ni 40 nm diameter wires (triangles) and Ni 120 nm diamter wires (circles) in comparison to the trends predicted by the Kittel equation.

deviations from crystalline anisotropy if relevant.

3. Make and test 200 nm and 20 nm diameter nickel MNW arrays to see if the trend of increasing deviation with decreasing wire diameter continues or saturates, and if sufficiently large diameter wires will behave predictably.

Determining the source of the behavior is useful because the saturation magnetization is an important property to predict behavior in most applications and is used in determining how much magnetic material was deposited when FMR-based characterization is not performed. If the saturation magnetization is higher than the expected value, the amount and quality of the fabricated NWs may be over-estimated. Additionally, if the phase is metastable or in a strained state that changes phase or relaxes once the MNWs are no longer confined to the template, this will change the behavior of the nanowires when freed from their template compared to applications that keep the MNWs in-template.

4.3.2 Maturation of Technology

Lastly, if this method is to be used in industry, some further development would be needed. First, it would probably be cheaper and less noisy to modify the measurement setup to use one frequency or a small range of frequencies and vary the magnetic field to determine the resonance peak. Alternatively, instead of an electromagnet, a series of DC magnetics could be used to apply different DC magnetic fields which would ultimately save power. To save processing time, automation of the FMR procedure, analysis, and length estimation could be done using relatively simple scripts, depending on the software and measurement setup used. Lastly, in order to save time and increase reproducibility, better fixtures could be developed, both to place the MNW array and replaceable ground plane and to ensure the orientation and spacing of the electromagnet is consistent between measurements. However, these tasks are less well suited to a research lab scale operation. Most of these are apparatus-specific, and would largely be beneficial when scaling up this technology for use on a production line.

Chapter 5

Cryopreservation and Nanowarming

5.1 Cryopreservation Background

Cryopreservation is the preservation of biological tissues at cold temperatures in order to extend the viability outside of a living body. One of the primary goals in advancing cryopreservation technologies is to increase the amount of successful organ transplants each year. Viable organs for transplants are rare, and it is often difficult to prepare the patient and transport the organ within the 4–12 hour window that most organs remain viable using conventional preservation methods [99]. To extend this time, perfusing the tissue with a cryoprotective agent (CPA) and preserving it at much colder temperatures (at or below -135 °C) has been established for small sample tissues [100, 101], in a process called vitrification. Vitrification is cooling while maintaining an ice-free glassy state at low temperatures. Because water expands upon freezing, ice formation will damage or destroy the cells. Cryopreservation been successfully used to preserve single celled organisms, for which there are numerous established protocols, and small tissues such as pancreatic islets [102], liver slices [103], and coral larvae [104]. However, convective warming has challenges in bringing the tissue back to body temperature without damage, especially for samples larger than 2-3 ml [99]. There is ongoing work in expanding cryopreservation capabilities so that larger volumes on the scale of liters can be successfully cryopreserved and rewarmed [105].

One of the primary challenges in cryopreservation of complex systems and organs is rewarming or devitrification of the cryopreserved tissue from the cryopreservation temperature (at or below -135°C). To minimize tissue cracking and cell death, devitrification needs to be performed quickly, above the critical rewarming rate (CWR) for the cryoprotective agent [106]. The CWR is specific for each CPA, a selection of of which is shown in Table 5.1. These rates are high in order to prevent ice formation when warming the vitrified tissue. Typically there is a trade off between cytotoxicity and CWR: less cytotoxic CPAs or lower concentration CPAs tend to have a higher CWR [107]. Additionally, this heating needs to have minimal thermal gradients within the tissue to prevent cracking and breakage of the tissue. The need for fast and even heating becomes more difficult to meet as systems get larger due to heat transfer constraints. While there is ongoing work to improve the performance and decrease toxicity of CPAS [108, 109], if entire organs are to be rewarmed with minimal cell death, the reliability and heating uniformity of nanowarming technologies must be advanced.

Table 5.1: Critical Warming Rates

Cryoprotective Agent	Critical Warming Rate (°C/min)
Glycerol (6 M)	3200
DP6 (6 M)	189
VS55 (8.4 M)	50
M22 (9.3 M)	0.4

One method that has been proposed for achieving fast, even warming is nanowarming, where nanoparticles are suspended in the cryoprotective agent that is perfused into the tissue and used as nanoheaters [110]. These nanoparticles can be distributed throughout the organ, and having heat sources distributed throughout the tissue mitigates the issue of uneven heating compared to simple convective heating methods. The potential for heating rate depends on the mechanism used to heat the nanoparticles, which can generally be divided into plasmonic nanoparticles, super-paramagnetic ion oxide nanoparticles (SPIONs), and ferromagnetic nanoparticles. Plasmonic heating occurs when metallic nanoparticles (typically noble metals) are tuned so that when laser light in the biological transparency window ($\lambda = 700 - 1300nm$) is applied, surface plasmon resonances will absorb the light energy before subsequently releasing the energy as heat to the surroundings [111]. This is a viable warming method and has been shown to work for cryopreservation at small scales [112]. However, plasmonic heating is difficult to scale up, because lasers with appropriate light intensity typically have a small spot size. For both SPIONs and ferromagnetic nanoparticles, instead of laser light, an alternating magnetic field (AMF) is applied to the sample. The nanoparticles can heat the surrounding media either by Neel [113] or Brownian [114] relaxation mechanism. For a schematic of the heating mechanisms, see Fig. 5.1. With Neel heating, the applied field overcomes the energy barrier to switch or rotate the magnetization of the particle, which releases heat [115]. This can also be considered as hysteretic losses. Brownian relaxation occurs when the particle rotates in a fluid, and heating occurs due to viscous dissipation. These processes occur in parallel, and the mechanism with a lower energy barrier dominates. The larger the hydrodynamic radius r_H of the sample, which can be altered depending on the particle coating, and the more viscous the suspending fluid, the less dominant the Brownian heating mechanism will be. However, in order to activate Neel heating, applied fields must have a magnitude that will change the nanoparticle magnetization. When applied to cryopreservation, much of the heating occurs when the system is cold and the CPA is in a viscous, glassy state. This means that it is likely that rotation of the particle, and therefore Brownian relaxation, will be suppressed. As such, Neel relaxation is expected to dominate at low temperatures, and the particle design should take that into consideration.

While both SPIONs and ferromagnetic nanoparticles both rely on an applied AMF to induce heating, they behave differently. As discussed in Section 2.1, the area inside of the hysteresis loop represents the energy lost as the applied magnetic field is cycled. When measured using a static measurement such as using a standard VSM, superparamagnetic particles such as SPIONs have no area in a hysteresis loop. The magnetic field used to excite the system must be a high frequency (kHz-MHz) to expand the hysteresis loop. SPIONs have been used to successfully rewarm organs, such as rat livers [116] and kidneys [117], where the applied field was 180-360 kHz with a maximum applied field of 20-60 kA/m depending on the frequency. SPIONs have already been approved by the FDA for some applications [118], which eliminates a major hurdle to commercialization. However, because of the superparamagnetic nature of the particles, the maximum hysteretic heating is lower than a ferromagnetic particle and heating is

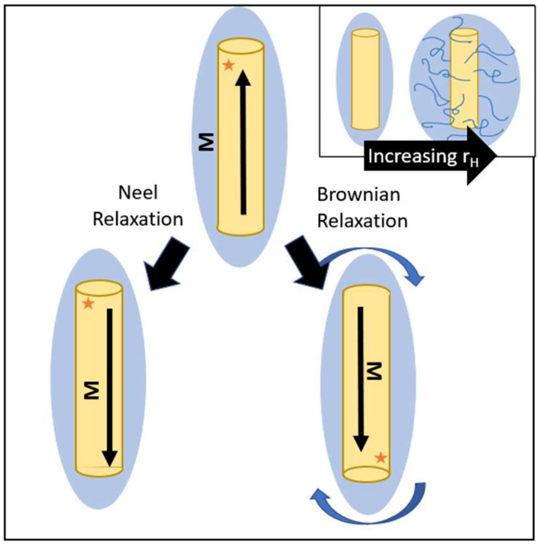

Figure 5.1: A schematic of Neel and Brownian relaxation mechanisms is shown for a nanowire. The inset schematic shows the increasing hydrodynamic radius (r_H) with functionalization of nanowires.

restricted to high frequencies. Dense particle loading and specific equipment is required to achieve the CWR needed with the CPA cocktails in use today. On the other hand, ferromagnetic particles have an area under the hysteresis loop even with measurements taken at DC fields. This area depends on the coercivity and saturation magnetization of the particles. For nanowires, these properties are tunable which makes for a great heating candidate, because the particles can be adapted to maximize the constraints of the available equipment. Initial results from FeCo MNWs in Glycerol show heating rates of up to 1610 ± 20 W/g [119], but exhibited significant stability issues. In order to improve the potential for MNWs to be used as nanoheater and expand the range heating rates available in cryopreservation applications, coatings to produce stable suspensions of ferromagnetic nanowires are explored.

5.2 Suspensions of MNWs

5.2.1 Introduction

Coatings can help stabilize a nanoparticle in solution by steric inhibition or electrostatic repulsion. Steric stabilization is when the bulky coating prevents nanoparticles from interacting and aggregating due to the coating physically inhibiting the particles from touching and the increased energy of the coating when coatings overlap[120]. In ferromagnetic particles, the thicker the layer, the better it is at minimizing interactions, because local magnetic fields from the neighboring nanowires decay proportionally to r^3, where r is the distance between the wires. Stabilization by electrostatic repulsion occurs when nanoparticle coatings have like charges, and the repulsion of these charges makes it energetically unfavorable for particles to interact and collect. In either case, the goal of the coating is to make the suspension of the nanoparticle more energetically stable than the process of aggregation and dropping out of solution.

Assessment of steric stabilization is typically done by measuring the size of the coated particle in solution, or hydrodynamic radius, using Dynamic Light Scattering (DLS). This method uses the fluctuation of scattered laser light to compute an estimate of the particle size distribution [121]. To correlate the light intensity with particle size, DLS relies on a number of assumptions. It is assumed that the particles are spherical and the motion is Brownian or random. This is important to understand when assessing the size of particles such as magnetic nanowires, because the assumptions are violated on multiple accounts. Because the nanowires are ferromagnetic, there are additional forces acting on the particles. The nanowires will likely move more quickly, and the calculated size will be smaller than the reality. As for the shape anisotropy, some work has been done to add in rotational as well as translational diffusion to account for the additional degree of freedom in the system [122]. This adjustment requires processing the raw scattered intensity data, which is not available on many commercial machines and has only been verified for particles with a much lower aspect ratios that the wires used here. Because of the large assumption violations MNWs, DLS is not chosen to characterize the particle coatings in this work.

The electrostatic stabilization is characterized using zeta potential (ζ). When a charged particle is in solution, a stationary layer of oppositely charged ions accumulate at the particle surface. The zeta potential is a measurement of this charge at the slip plane, and therefore is a measure of the potential difference between the bulk fluid and the stationary corona of charges around the particle [123] [124]. Generally, $\zeta \geq |30|\ mV$ is considered stable [46, 121], where the electrical charge on particles repel each other enough to prevent coagulation, aggregation, or flocculation. Two main methods of measuring zeta potential are the zeta streaming potential and by electrophoretic mobility. To measure the streaming potential, an oscillating piston is used to induce fluid flow, while charged particles are adsorbed to the surface of piston and cup. The fluid flow moves the ion cloud around the particles, and this current induces a voltage, which can be measured between electrodes on the side of the cup [124]. Electrophoretic mobility measurements are made by applying an oscillating potential to the suspension in a capillary cell. The velocity of the particles are measured using laser Doppler velocimetry and is sometimes combined with phase analysis light scattering. This velocity is measured per unit field strength and gives the electrophoretic mobility. This mobility (U_E) is then used to determine the zeta potential through the Henry equation (Eq. 5.1), which requires the dielectric constant (ϵ) and viscosity (η) of the suspending fluid to be known. $F(\kappa_a)$ is a value known as Henry's function, and is dependent of the Debye length (κ_a) of the fluid. The Huckel approximation for nonpolar media estimates $F(\kappa_a) \approx 1.0$ [123]. For polar media, the Smoluchowski approximation is used where $F(\kappa_a) \approx 1.5$ [123]. A notable difference is that the streaming potential measurements do not need input properties of the suspending fluid or the particles in order to take a measurement. This is useful when working with solvent cocktails such as CPAs. However, electrophoretic measurements require lower sample volumes and concentrations and typically have better control over the measurement temperature. In this section, the measurements made on the Stabino zeta potential analyzer are measured using the streaming potential, while the zetasizer measurements are based on electrophoretic mobility.

$$U_E = 2\epsilon\zeta F(\kappa_a)/3\eta \tag{5.1}$$

Coating and stabilizing nanoparticles in solution is not a new problem. However, most work has been done in aqueous solutions, and CPA cocktails contain solvents such as DMSO which can pose challenges to getting a coating to stably adsorb onto a particle. Previous work by this group has not yet reported a stable coating when functionalization processes used in normal, aqueous settings were applied [119]. Work by Pasek-Allen et. al. has used phosphate linkers to bind PEG (polyethylene glycol) to the particle surface [125]. However, this relies on a ligand exchange reaction and starts with a silica coating. Additionally, some research has done work on covalently bonding a coating to the surface, but this typically requires more hazardous, reactive materials [126]. When working with nanoparticles made using a reverse micelle reaction method, the nanoparticle is fabricated with its own coating which exchange reactions can be used to switch out the initial coating for a more desirable one. This is not generally the case for NWs fabricated using template-assisted electrodeposition. Upon release from the template, the NWs don't have a coating. However, if AAO is used as the template, etching away the template produces a metal hydroxide surface on the nanowires [127]. Depending on the pH of the suspending solution, the charge of the nanoparticle surface can vary. If the solution is acidic, a proton can be adsorbed and the surface charge becomes positive. If the solution is basic, a proton can be removed, and the surface charge will be negative. The point where the charge is zero is called the isoelectric point or the point of zero charge (PZC). The isoelectric point is different depending on the particle material and suspending fluid. Here, the isoelectric point of the MNWs in different solutions is measured in different coating solutions in order to determine the best pH for coating the particles.

One necessary piece of information to determine coating conditions when doing an electrostatic based coating is the pKa of the coating polymer. For the general acid dissociation reaction (Eq. 5.2), the Henderson-Hasselbalch equation (Eq. 5.3) allows for calculation of the relative concentrations of the conjugate base and the acid for a given pH at equilibrium [128]. If the pKa is known for the functional groups on the coatings, then the pH of the coating solution can be adjusted such that there is a significant concentration of the coating charged opposite to the NW surface. The pKa of the coatings can be determined by performing titrations in of the coating polymer in solution.

$$HA \rightleftharpoons A^- + H^+ \tag{5.2}$$

$$pH = pK_a + log_{10}([A^-]/[HA]) \tag{5.3}$$

Four different coatings were selected as coatings to test for this application: low molecular weight polyvinylpyrrolidone (PVP), high molecular weight PVP, branched polyethylenimine (PEI), and a PEI-PEG block copolymer. All options have molecular weights above 1000 kD, which was selected to ensure some steric inhibition is present for all coatings. PEI has been used for nanoparticle coatings that were found to be stable in water, DMSO and ethylene glycol [129], has multiple coordination sites which may add thermodynamic stability over single site coordinating compounds, has demonstrated coordination interactions with cobalt and nickel [130], and is large such that the buoyancy of the particle may increase. The PEI-PEG block copolymer has the advantage of the multiple coordination sites of PEI on one end, while the PEG end will not bond to the nanowire, but has been used as a stabilizer in other CPA-nanoparticle solutions. PVP also has multiple sites that may bind to the NW surface, and has demonstrated coordination reactions and particle stabilization with silver, nickel, and iron oxide particles [131, 132, 133, 134]. In addition to stabilizing the particle in solution, bio-compatibility must be taken into account for biological applications such as cryopreservation. All selected polymers have been used in biological settings. Many forms of both PVP and PEG are already approved by the FDA as a drug additive[135, 136]. PEI, while not broadly approved as an additive, is used in numerous biomedical applications [137]. While the selected coatings all hold some promise, the varied functional groups, structures, and molecular weights increase the possibility of finding a coating that works in these CPA cocktails.

In this section, in order to find a feasible way to stabilize MNWs in CPA cocktails four different particle coatings are explored. Iron and nickel nanowires are fabricated using template assisted electrodeposition before release from the templates. To determine a coating recipe, the isoelectric point of the free wires and the pKa of the potential coatings are experimentally determined. Finally, nanoparticle coatings are tested for stability in CPA cocktails using zeta-potential measurements.

5.2.2 Methods

CPA Mixing and Characterization

CPAs used in this study were made in-house. Recipes obtained are courtesy of Benjamin Fisher and Jaqueline Pasek-Allen, and are used in the Bischof and Finger labs. For the suspension studies, so far only DP6 and the Liver CPA are used, the compositions of which are found in Table 5.2. CPA cocktails were made with the final volume measurement in a volumetric flask before transferring to a storage container. In order to perform dynamic light scattering and some zeta potential measurements, the viscosity, index of refraction, and dielectric constant of the cryoprotective agents are required. While the dielectric constant was found in literature for DP6, the viscosity and index of refraction had to be measured for the CPA cocktails.

Table 5.2: CPA Compositions

Cryoprotective Agent	DP6	Liver CPA
DMSO	3 M	20 $v\%$
Ethylene Glycol	–	20 $v\%$
Propylene Glycol	3 M	5 $v\%$
HEPES Buffer	2.4 g/L	–
Sucrose	–	0.225 M
Water	*Remainder*	*Remainder*

The viscosity of DP6 and Liver Cryoprotectant was measured using a rotational rheometer (TA Instruments DHR-3, SN 5343-0716) with a double-wall concentric cylinder geometry (Stainless Steel, ARG2). Viscosity was measured as shear rate was changed from 0.01 to 1000 $1/s$ increased in 5 steps per order of magnitude. Data were collected for 60 s at each shear rate step. The measurements were made for each CPA at 20 ^oC and 30 ^oC, which was controlled by a Peltier-controlled concentric cylinder. The resulting plots were used to determine the viscosity to be used in the zeta-potential measurements.

The refractive index (RI) of each CPA was measured using a simple procedure that involves taking images of a beaker-fluid-graduated cylinder system and measuring the ratio of the graduated cylinder diameter above and below the liquid line [138]. Six images were taken of the beaker-CPA-graduated cylinder system. The refractive index was calculated for each photograph then the mean and standard error of the measurements was computed. All measurements were taken at room temperature. The resulting value was used to determine the refractive index of the CPAs to be used in zeta-potential measurements.

NW Fabrication and Suspension

MNWs were fabricated using the method described in Section 2.2.1. Iron and Nickel NWs were using AAO templates (Inredox) with 120 nm diameter pares and the fabrication time was calibrated to target a length of 2.5 μm. The deposition conditions are described in Table 5.3. For both wire compositions, a copper seed layer was used to encourage more even depositions, and was subsequently etched away. For the iron wires, a thin nickel etch stop was deposited before the iron to mitigate iron electrolyte etching of the back contact. Because the deposition time of iron is very short and the electrolyte etches away the iron quickly when not deposited, the time for iron deposition was determined by measuring the length of previously fabricated samples and determining a standard deposition time that would result in wires near 2.5 μm. On the other hand, Nickel deposition can be done slowly, so the current at 10 minutes (after the current had equilibrated) was used to calculate the total deposition time needed to deposit 2.5 μm long wires. A deposition efficiency of 0.5 was used, established from previous depositions under the same reaction conditions. Once deposited, the back contacts and copper seed layer were etched away. The saturation magnetic moment of the templates were measured to estimate the number of templates to use in the zeta-potential experiments.

Table 5.3: Deposition Conditions

NW	Layer	Electrolyte	Pulse Voltage (mV)		Pulse Length (s)		Cycles
			Low	*High*	*Low*	*High*	
Ni	1	Copper	−0.03	−0.08	1	1	90
	2	Nickel	−0.84	−0.89	1	1	$> 900^*$
Fe	1	Copper	−0.03	−0.08	1	1	105
	2	Nickel	−0.80	−0.85	1	1	90
	3	Iron	−0.72	−1.11	1	3	50

*Cycle number was calculated according to the current for each deposition.

Two different series of coating solutions were made, the initial tests having salt added and the latter solutions containing no salt. Later trials excluded salt, because while it helps dissolve the polymers, it may inhibit the ability adsorption of the polymers onto the wires. Before these solutions were made, the coatings were initially tested in propylene glycol (PG), but PG solutions were too viscous to effectively collect the MNWs from solution in a reasonable amount of time. Within each series, 50/50 v% EG/Water and PG/Water bases were made, and in each base 5 different coating solutions were made: a control (no additives), Polyvinylpyrrolidone or PVP ($\overline{MW}$: 8 kD), PVP ($\overline{MW}$: 58 kD), Branched PEI ($\overline{MW}$: 10 kD), and a linear PEI-PEG block copolymer (PEG $\overline{MW}$: 5 kD, PEI $\overline{MW}$: 5 kD). In each coating solution, 2 g of the coating polymer (i.e. PVP or PEI) were dissolved per 100 ml of base solution. For the initial solutions containing salt, 0.6 g NaCl were added per 100 ml of coating solution was added. The pH was then adjusted to values determined after measuring the isoelectric points of the NWs and the pKa of the coating polymer. For the initial tests containing salt, the PVP solutions had their pH adjusted to 7. The branched PEI and PEI block copolymer, were adjusted to a pH of 8 in the EG/Water solution and a pH of 10.5 in the PG/Water solution. The pH was adjusted using either HCl or NaOH as needed. Prepared coating solutions were stored in glass vials at room temperature.

In order to determine the coating pH, the pKa of the was found. More concentrated solutions of PVP and PEI were suspended in the 50/50 v% PG/Water coating bases. Titration curves were found by manually titrating in HCl via micropipette, while measuring the pH with a pH meter (Oaklon pH 5+ handheld meter). Before the pH was recorded it was allowed to equilibrate. After plotting, the pKa was determined by finding the pH at half the equivalence point. This pKa was used to evaluate the charge on the coating polymer at different pHs.

To coat the wires, wires first had to be released from the AAO templates. The number of templates per sample were determined by the saturation magnetic moment of the template as a proxy for the mass of the NWs, then the templates were placed in micro-centrifuge tubes, ground, and etched using 1 M NaOH. After the templates were sufficiently etched, the nanowires were collected using a magnet and the etchant was removed. 1 ml of coating solution was placed in each vial, and the samples were incubated in the refrigerator (4 ^{o}C) for 24 hours, sonicating and tapping the samples every few hours. After the incubation period, the MNWs were collected, the coating solution removed, and the measurement solution added. For the samples used to test the stability as different CPA components were added, 50/50 PG/Water or EG/Water was added initially. For the pH controlled samples (all done without salt), the appropriate CPA was added, then the pH adjusted to the initial testing pH of 9. The CPA to be added was DP6 for the PG/Water coating solution or the Liver CPA for the EG/water coating solutions. The sample stability was measured shortly after coating.

Zeta-Potential Analysis

Before coating procedures could be established, the isoelectric point of the was determined for Ni and Fe in both 50/50 v% EG/Water and PG/Water. These measurements, along with the initial coating measurements, were taken using the Stabino Zeta-Potential Analyzer, which measures the zeta-potential based on electrophoretic mobility The NW concentration in solution was estimated at about 0.002 wt% for each, in 10 ml of solution. The titration function on the Stabino zeta potential analyzer was used to titrate the coatings. The pH was first adjusted to 11 using 1 M NaOH, then the pH was titrated down to 2 using a M HCl. The isoelectric point was determined by the pH where the measured zeta potential changed from negative to positive. .

Initial measurements for the coatings were taken to evaluate if the samples were coated and how the sample stability changed with the addition of specific cryoprotectant coatings. These measurements were taken using samples prepared with salt-containing coating solutions, with different samples for each coating (including the control). CPA component additions were made to reflect the ratio of the components in the final CPA cocktail. For the samples coated in the PG/Water-based coating solutions, the samples were re-suspended in 560 μL of the 50/50 v% PG/Water solution. Then, the zeta potential of each sample was measured in the following solutions:

1. 0.560 mL of the sample in 50/50 v% PG/Water solution with 0.440 mL of DI water added
2. PG Solution 1 with 0.270 mL of DMSO added
3. PG Solution 2 with 0.003 g HEPES added.

The final solution was the NWs suspended in DP6. For the samples coated in the EG/Water-based coating solutions, the samples were re-suspended in 400 μL of 50/50 v% EG/Water solution. Then, the zeta potential of each sample was measured in the following solutions:

1. 0.400 mL NW in 50/50 v% EG/Water with 0.600 mL DI water added
2. EG Solution 1 with 0.250 mL DMSO added
3. EG Solution 2 with 0.066 mL of PG added
4. EG Solution 3 with 0.100 g sucrose added

The final solution here surmounted to NWs suspended in the Liver CPA. For all measurements, the sample was mixed and given time to equilibrate whenever a new solution component was added, and the temperature was the ambient lab temperature.

Later measurements were taken using the zetasizer (Malvern Zetasizer Nano ZS), which uses the electrophoretic mobility to measure the zeta potential. This change is due to equipment malfunction and down time. When the zetasizer is used, the refractive index, viscosity, and dielectric constant of the suspending fluid must be known. Due to these considerations, the stability was not tested stepwise as components were added. DP6 was the only CPA measured, as the dielectric constant of the Liver CPA is unknown. For these measurements, the parameters listed in Table 5.4 were used. For this set of measurements, one sample of nickel NWs was prepared in each of the PG-based coating solutions (including the control) without salt. After coating, the samples were re-suspended in DP6 and titrated to a pH of 9 using HCl or NaOH as needed. Zeta potential measurements were taken for each sample at a pH of 9, 7, and 5. The pH was adjusted between samples using 1 M HCl. Care was taken not to overshoot the pH when titrating downward to minimized the added salt in each sample. All zeta-potential measurements were taken at a controlled temperature of 20 ^oC using a polycarbonate cuvette. The zeta-potential was calculated using the Smoluchowski model for polar media. Because of the controlled conditions and batch, these measurements are likely more representative of the behavior expected in solution.

5.2.3 Results

CPA Characterization

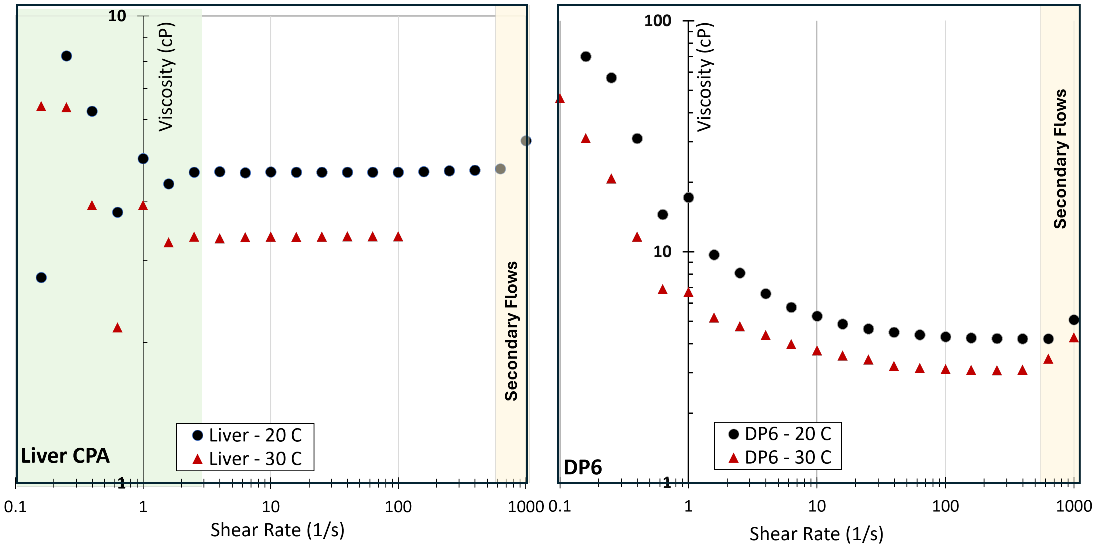

Figure 5.2: The viscosity is plotted as a function of shear rate for the liver CPA (left) and DP6 (right). Areas where the data are affected by secondary flows are denoted with yellow, and the area that is noisy due to low flow rates and viscosity is denoted with a green box.

The zetasizer uses the Henry Equation (Eq. 5.1) to relate the measured electrophoretic mobility to the zeta potential, and requires RI and viscosity values for the suspending fluid. Because the CPAs used for suspensions are not well-characterized in literature, the RI and viscosity of the CPAs were measured. The RI was found to be 1.41 ± 0.01 for DP6 and 1.38 ± 0.02 for the Liver CPA. The viscosity measurements are presented in Fig. 5.2. For both CPAs inaccuracies arose at shear rates above 500 1/s due to the presence of secondary flows, marked by the yellow boxes in Fig. 5.2. For low viscosity fluids the viscosity measurement tends to be noisy at low shear rates which is exhibited by the liver CPA. As a whole, the liver CPA exhibits Newtonian behavior, and the viscosity measurements between 2.5 and 650 1/s were averaged to determine a value for the viscosity, given in Table 5.4. DP6 did not have particularly noisy behavior at low shear rates, because the viscosity is much higher. DP6 behaves as a shear thinning fluid. Because of the shear-thinning behavior, the exact value that would be applicable during the zeta potential measurement, as the local viscosity around the particles would be unknown. Initially, during zeta potential testing, the lowest shear rate value was used. This produced unreasonable results ($> |200| mV$), so the same measurement regime as the liver CPA was used where the points in the linear regime were averaged. These values are reported, along with all the parameters used in the zetasizer measurements, in Table 5.4. Note that the non-Newtonian behavior contributes to orders of magnitude larger uncertainty compared to the liver CPA. Lastly, the real part of the dielectric constant for DP6 was estimated from work by Gangwar, et. al [139] characterizing the dielectric constant of some CPAs. All the material parameters measured for CPA needed for zeta potential (and dynamic light scattering) measurements were different than the sum of their components, and this indicates that further characterization of CPAs would enable further research into the stability of particle suspensions for cryopreservation applications.

Table 5.4: CPA Characterization Values Used in Analysis

CPA	Viscosity (cP)		RI	Dielectric Constant
	20 ^oC	30 ^oC		
DP6	5.1 ± 0.3	3.5 ± 0.2	1.41 ± 0.01	$60 + i20$
Liver CPA	4.646 ± 0.007	3.370 ± 0.003	1.38 ± 0.02	–

Coating Recipe Development

In order to develop the coating recipe, the pKa of the coatings and the isoelectric point or PZC of the nanowires were found. The pKa of PEI was found to be 8.5 in the PG/Water mixture, which matched expectations from literature [140, 141]. The pKa of the PVP was found to be 4.4. The PZT results of the NWs in solution are shown in Fig. 5.3 as the black line on the pH scale dividing the maroon (negatively charged wires) and the green (positively charged wires) bars. The difference between the PZC for the wires in the EG/Water solution (marked as "EG") was suprisingly signficantly different compared to the wires in the PG/Water solution (marked as "PG"). The

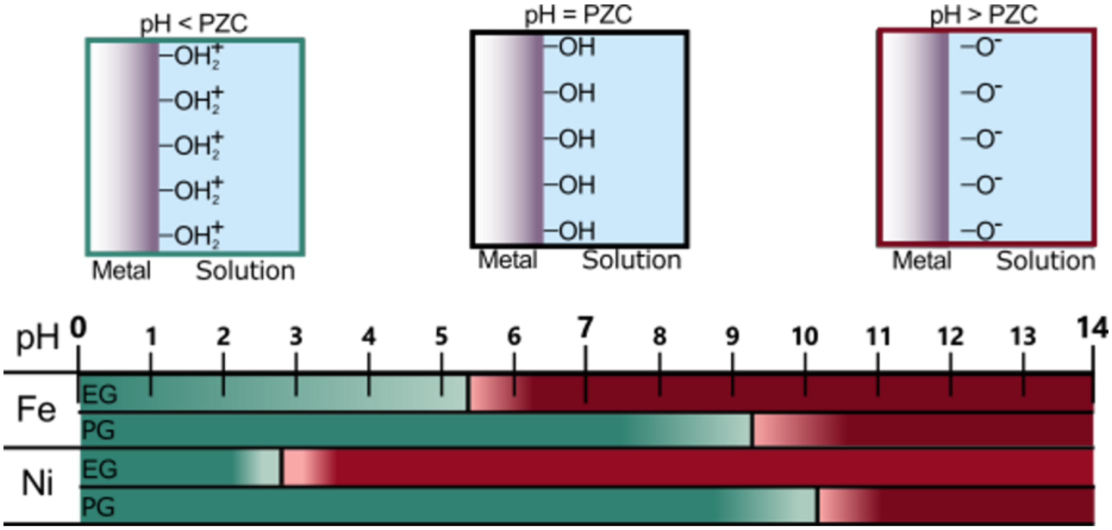

Figure 5.3: (Top) Schematics of the surface charge is shown for different pH values. (Bottom) The point of zero charge for each NW material-coating base solution combination is shown on a pH scale, with the PZC indicated by the black line.

experimental values were used, along with the Henderson-Hasselbach equation (Eq. 5.3), in an attempt to maximize the number of opposite charges of the wires compared to the coatings. Salt was initially included in the recipe to help solvate the coating polymers. However, the salt was excluded in later attempts, as it was expected the presence of significant quantities of salt was inhibiting some coating. The procedure in Section 5.2.2 is the result of these measurements.

Suspensions

Initial results on particle stability measure the zeta-potential for different coatings as the CPA components were added and compared to a control consisting of uncoated wires in solution. This measurement assesses the electrostatic or charge stabilization of the coated particles, and a zeta potential (ζ) of $\geq\ |30|\ mV$ is considered to be stable. Results for this set of experiments are shown in Fig. 5.4. Here, the only coating that could be considered stable was the branched PEI in the DP6 solution, but only once the HEPES buffer was added. There is a trend in the results for the DP6 solutions, where the zeta potential changed significantly once HEPES -a pH buffer- was added.

This indicates that the stability results are highly pH sensitive, and that this must be well controlled in further trials. These initial results showed a promising start, especially considering that all these coating solutions contained salt, which was expected to inhibit the degree to which the NWs were coated.

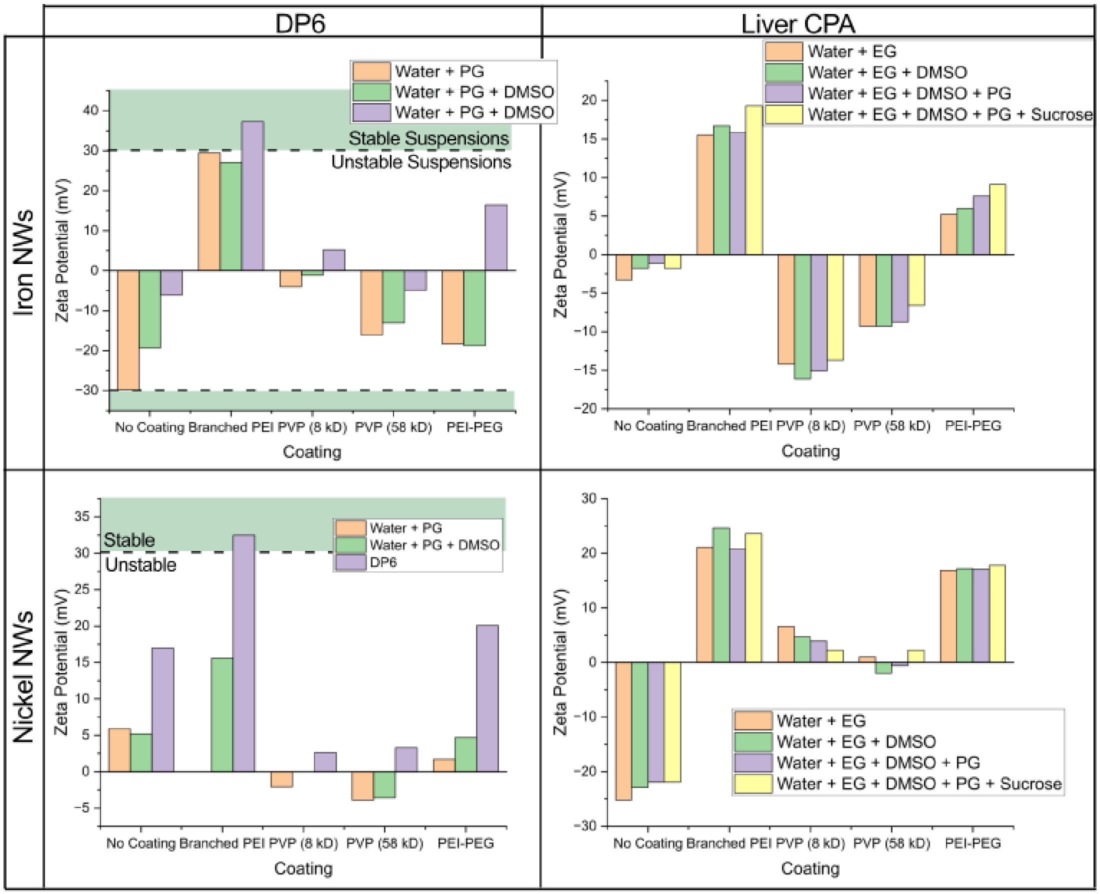

Figure 5.4: Initial stability data for iron (top) and nickel (bottom) NWs in DP6 (left) and Liver CPA (right) for each tested coating as components are added.

While the first set of results did not have many electrostatically stable suspensions, the results can tell us something. First, while all of the coated wires in the liver cryoprotectant are under the threshold of $\zeta \geq |30| mV$, all of the potentials are significantly different than the control, which indicates that the wires were successfully coated. While charge stabilization might not be enough to stabilize the particles alone, steric hindrance from the coatings may contribute to stabilizing these particles. In both solutions, the PVP coated particles produce similar results, which is expected. When you compare branched PEI and the PEI-PEG block copolymer, you can see that generally, the block copolymer has less of a charge than the branched PEI, but more than the PVP. This is to be expected, as the portion of the coating that should be adsorbed to the particle surface is the PEI, while PEG -typically uncharged in solution - is facing the solution to provide more steric hindrance. The fact that the block copolymer has some charge in the same direction shows that the portion that is made of PEI is contributing some electrostatic stabilization. Additionally, there are no significant trends when DMSO is added to the DP6 solutions or when DMSO or PG was added to the liver CPA, except in the control wires. In the control sample, the addition of DMSO or PG reduced the stability of the particle in every combination of CPA and NW material. However, for the coated particles, this was not the case. Even when the coating does not significantly improve the charge stability of the particles, they seem to improve the sensitivity of the particle charge to some of the CPA components.

The zeta potential was measured for nickel nanowires with different coatings, all in DP6, with coating solutions that did not contain added salt. While the composition of the solvent was kept constant, the pH was controlled and the stability was tested at three different pH values: 5, 7, and 9. These measurements were performed using the zetasizer, which uses laser doppler electrophoresis to determine the zeta potential and required additional parameters regarding the solvent to be input, given in Table 5.4. Results are shown in Fig. 5.5. Each data point is the average of three measured values, which are each composed of 10-100 individual measurements depending on the stability of the measured value. Error bars are present when visible. The wires measured without a coating generally had the largest error bars, and this is expected to be due to some particles falling out of solution or aggregating. For this coating process in DP6, all coatings had regions of charge stability, depending on the pH. PVP coated wires had more stability at higher pH values, although not significantly more that the wires without any coatings. At a pH of 5 and 7 Branched PEI and the PEI-PEG block copolymer had zeta-potential values of more than double that required to be considered stable, and is above or only sightly below 30 mV at a pH of 9. Since a pH slightly above 7 is typically needed for biological applications, this demonstrates that either Branched

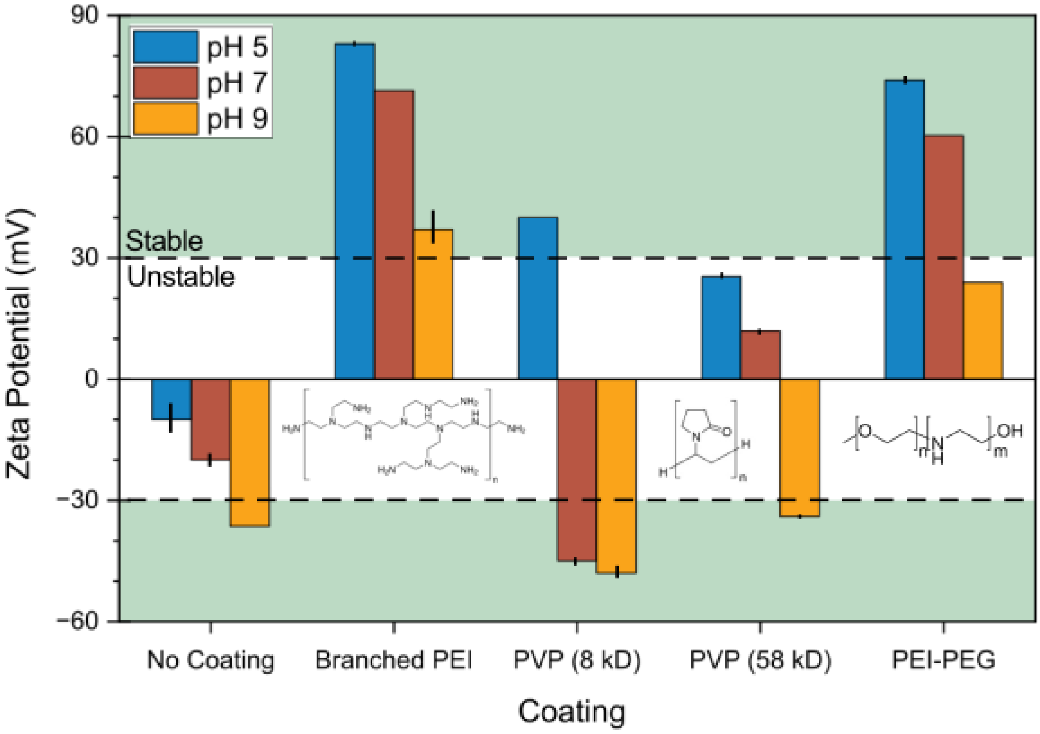

Figure 5.5: The zeta potential of nickel nanowires in suspended in DP6 is plotted for each coating at a pH of 5, 7, and 9. Error bars are present when visible.

PEI or the PEI-PEG block copolymer are feasible coatings for cryopreservation. PVP may be a feasible coating for cryopreservation, but the isoelectric point seems to be near seven, which would make the stability sensitive to fluctuations in pH. However, all of the coatings may contribute to steric hindrance, reducing aggregation of particles.

5.2.4 Summary and Conclusion

Coating processes were developed and electrostatic stability tested for nanowires in two different CPAs. Four different coatings were tested: PVP (MW: 8 kD), PVP (MW: 58 kD), Branched PEI, and PEI-PEG block copolymer. To develop coating recipes, the isoelectric points for the wires in EG/Water and PG/Water solutions were found, and the pKa of the potential coating polymers were measured. Based on the measurements performed here, when the solutions without salt were used, both branched PEI and PEI-PEG block copolymer are produced charge-stabilized suspensions in DP6 cryoprotectant at relevant pH values. MNWs with these coatings are a viable option for future nanowarming studies. However, rewarming for cryopreservation is not the only application the coating studies performed here can support. The application space for suspended nanoparticles is broad, and these coatings are not specific to nanowires or CPA cocktails.

5.3 Future Work

Here the electrostatic contribution to stability is measured, but it would be useful to have some measure of the contribution of steric hindrance to the stability of the nanowires in solution. While DLS is not an accurate quantitative technique due to the high shape anisotropy and ferromagnetic nature of the particles invalidating the assumptions integral to the measurement technique, it may be useful as a comparative measurement for the same sample at different pH values or to compare different coatings. Additionally, UV-Vis spectrometry may give a more complete picture of the stability by linking the change in light absorbance over time to the settling of particles out of solution. These measurements would give a more complete understanding of the particle stability when these coatings are used.

In future work, it would be useful to repeat the coating work with other NW and CPQ systems. For NWS, MWs with a composition of $Fe_{65}Co_{35}$ are expected to be the most efficient heaters due to their high saturation magnetization and resistance to corrosion. It is expected that coatings would behave similarly on $Fe_{65}Co_{35}$ NWs compared to the iron NWs tested here, which provides a starting point. Additionally, larger diameter MNWs may need to be explored. Here 120 nm diameter wires were explored for the coating work. However, when released and coated, the wire diameter is effectively shrunk by oxidation. Depending on the heating equipment used, it may be useful to expand this work to larger diameter wires in order to achieve lower coercivities. Lastly, there is ongoing research into effective CPA cocktails. While the two CPAs studied here, DP6 and the Liver CPA, contain many common components, coating results will vary depending on the contents and ratios of components in a CPA. As new CPAs are developed, the characterization of the CPAs and the stability of particles in CPAs will need to be explored if nanowarming with NWs is to be achieved.

The next essential step in continuing this work is to study the heating behavior of these stabilized nanowires. For this, batches of these nanowires solutions will need to be made then concentrated down. Controlled scale up of the electrodepositon process would aid in enabling these studies. A priority would be testing different types and concentrations of stabilized MNWs to determine their heating rate in solution. Depending on the heating equipment available, multiple frequencies and field strengths should be tested. Additional testing would need to be done to see if the the particle coatings are stable with and after heating and to determine how much of an effect the coatings have on heating and heat transfer.

Some feasibility should be on considered for the application. While all the coatings used were selected because they have been used in biological systems, the biocompatibility of these coating would need to be verified. Additional work would need to be done to evaluate if these coatings can protect from the potentially harmful effects of metals such as nickel and cobalt. If these coated particles are to be tested for whole organ rewarming tests on the particles recovery from the vasculature would also be needed to assess safety. Organ is not the only system that would benefit from rapid rewarming, and further development may be able to meet the needs of other systems.

Chapter 6

Conclusion and Discussion

The work presented in this thesis focused on narrowing knowledge gaps needed to implement templated nanowires into three different proposed applications. Chapter 2 introduced the properties unique to nanowires along with relevant fabrication and characterization techniques. The unique properties of nanowires result from a high surface area to volume ratio, the high shape anisotropy, and for the lowest diameter nanowires, quantum confinement effects. The electronic and magnetic properties especially are sensitive to the diameter and surface of the NW, and this sensitivity is useful for applications that benefit from the ability to tune the electro-magnetic behavior. All wires in this thesis were made using template assisted electrodeposition. Template assisted electrodepositon is advantageous because it has strong control over the two parameters to which the NW properties are most sensitive - diameter and wall smoothness- while being versatile and allowing for high shape anisotropies. The methods broadly used to characterize the nanowires produced were SEM/EDX, x-ray diffraction, and magnetometry. The applications addressed in this thesis all could benefit from the use of well-designed nanowires, but significant work needs to be done in order to improve the feasibility.

Chapter 3 addresses the need for a stable way to integrate vertically oriented nanowires onto silicon substrates. Integration into silicon allows for incorporation into a broad range of electronic and magnetic devices, as most of the electronic and nanofabrication processes are designed to be used and interface with silicon wafers. Starting with an aluminum anodization process developed by a previous student, the process control over the pore sizes and anodized aluminum oxide (AAO) layer thickness were assessed for both process variations, along with the AAO mechanical and thermal stability on the wafer. Nanowires were deposited into the templates. The resistivity of copper nanowires and the magnetic properties of nickel nanowires were assessed in the templates. Additionally, integrated copper nanowires were incorporated into a coplanar waveguide device, and the capabilities of the wires as grounding vias were assessed at high frequencies. As a whole, the integrated AAO was mechanically and thermally stable up to 350 °C, and the device made with the templated MNWs was functional.

Chapter 4 addresses not one specific application, but the manufacturability of devices that use magnetic nanowires fabricated in templates. In order to understand the fabrication yield and quality, fill factor and saturation magnetization should be known. There are few accurate and quantitative methods that measure these values with a high degree of uncertainty. In this work, a method for the nondestructive measurement of both values centered around ferromagnetic resonance was proposed and experimentally validated. The first test of the method used cobalt magnetic nanowire arrays fabrication to have two different fill factors. The results were confirmed by comparison to qualitative and semi-quantitative methods for evaluating fill factor such as FORC and EDS. The second test used CoFe alloyed nanowire sample and compared the FMR results to what would be expected based on the measured composition. Both tests confirmed the viability of the proposed method to accurately quantify the saturation magnetization and fill factor of a magnetic nanowire array. Additionally, while being nondestructive, it is sensitive enough to capture small changes in either and decouples the saturation magnetization measurement from the fill factor. The method proposed here was shown to not only be a viable method to evaluate the quality of a nanowire sample, but potentially the best available today.

In Chapter 5, magnetic nanowires are coated to enable nanowarming for cryopreservation applications. To develop coating recipes, the isoelectric points of nickel and iron MNWs and the pKa of coatings in two different coating bases were determined. To measure the stability of the nanoparticles in solution, the viscosity and refractive index of cryoprotective agent cocktails were measured. Lastly, the zeta potential was measured to evaluate the stabilization of the wires in cryoprotective by electrostatic repulsions. For nickel nanowires suspended in DP6 cryoprotective agent, stable suspensions were found for PEI, PVP, and PEI-PEG coatings. Of the coatings explored, PEI and PEI-PEG showed were likely the best suited for cryopreservation applications, because they had the highest zeta potentials near neutral pH. This work enables further study of magnetic nanowires for use as nanoheaters, which has the potential to allow for faster heating with lower particle loading needed.

For all applications studies here, there more work to be done. For the vertically integrated nanowires, further improvements in controlling the pattern and regularity of the pores is needed. In order for the nondestructive FMR characterization method to be fully understood, irregularities with nickel sample need to be studied. Lastly, the stabilization of nanowires in cryoprotective agents is just the start of the work for heating, as the heating ability in solution for these wires has not yet been studies. While the work documented here has narrowed the gap to application, the gap is not entirely bridged.

References

[1] Aditya Dave, Yali Zhang, Nikita Mahjabeen, Allison Harpel, Rashaunda Henderson, Bethanie Stadler, and Rhonda R. Franklin. 180 GHz low-loss copper nanowire CPW interconnects. In *2022 IEEE/MTT-S International Microwave Symposium - IMS 2022*, pages 1034–1036. IEEE, 2022.

[2] Girfan Shamsutdinov, Peng Zhao, Sreenivas Bhattiprolu, Ji-Cheng Zhao, and Boris Nadgorny. Magnetization–structure–composition phase diagram mapping in co-fe-ni alloys using diffusion multiples and scanning hall probe microscopy. *Scientific Reports*, 12(1):1957, 2022.

[3] Yu P Ivanov, M Vázquez, and O Chubykalo-Fesenko. Magnetic reversal modes in cylindrical nanowires. *Journal of Physics D: Applied Physics*, 46(48):485001, 2013.

[4] Cristina Bran, M. Vazquez, E. Berzanga, M. Jaafar, E. Snoeck, and A. Asenjo. Chapter 16: Magnetic imaging of individual modulated cylindrical nanowires. In *Magnetic Nano- and Microwires: Design, Synthesis, Properties and Applications*, pages 455–482. Elsevier, 2 edition, 2020.

[5] M. Vázquez, K. R Pirota, Manuel Hernández-Vélez, Victor Prida, David Navas, Ruy Sanz, Francisco Batallan, and Julián Velázquez. Magnetic properties of densely packed arrays of ni nanowires as a function of their diameter and lattice parameter. *Journal of Applied Physics*, 95:6642, 2004.

[6] J. Escrig, D. Altbir, M. Jaafar, D. Navas, A. Asenjo, and M. Vazquez. Remanence of ni nanowire arrays: Influence of size and labyrinth magnetic structure. *Physical Review B*, 75(18):184429, 2007, 0710.5757 [cond-mat].

[7] Manuel Vasquez. *Magnetic Nano- and Microwires: Design, Synthesis, Properties and Applications*. Elsevier, 2 edition, 2020.

[8] Julian A. Moreno, Cristina Bran, Manuel Vazquez, and Jurgen Kosel. Cylindrical magnetic nanowires applications. *IEEE Transactions on Magnetics*, 57(4):1–17, 2021.

[9] M Almasi Kashi and A H Montazer. Template-based electrodeposited nonmagnetic and magnetic metal nanowire arrays as building blocks of future nanoscale applications. *Journal of Physics D: Applied Physics*, 55(23):233002, 2022.

[10] Mohammad Reza Zamani Kouhpanji, Ali Ghoreyshi, P. B. Visscher, and Bethanie J. H. Stadler. Facile decoding of quantitative signatures from magnetic nanowire arrays. *Scientific Reports*, 10(1):15482, 2020.

[11] Allison Harpel, Joseph Um, Aditya Dave, Yali Zhang, Nikita Mahjabeen, Yicong Chen, Rashaunda Henderson, Rhonda Franklin, and Bethanie J. H. Stadler. Vertically integrated nanowires on si wafers and into circuits. *IEEE Transactions on Magnetics*, pages 1–1, 2022.

[12] Allison Harpel, Md Toaha Anas, Alex Wege, Rhonda R. Franklin, and Bethanie J. H. Stadler. Nondestructive ferromagnetic resonance measurements validate the efficacy of a seed layer in cobalt magnetic nanowire fabrication. *IEEE Transactions on Magnetics*, 61(3):1–9, 2025.

[13] Md Toaha Anas, Allison Harpel, Bethanie J.H. Stadler, and Rhonda R. Franklin. Characterization of ferromagnetic resonance identification (fmr-id) tag in semi-wireless configuration. In *2025 IEEE Wireless and Microwave Technology Conference (WAMICON)*, pages 1–4. IEEE, 2025.

[14] Y. Unutulmazsoy, R. Merkle, D. Fischer, J. Mannhart, and J. Maier. The oxidation kinetics of thin nickel films between 250 and 500 °c. *Physical Chemistry Chemical Physics*, 19(13):9045–9052, 2017.

[15] Anirudh Sharma. *Multi-segmented magnetic nanowires as multifunctional theranostic tools in nanomedicine*. Doctor of philosophy, Univeristy of Minnesota, 2015.

[16] Shiliang Wang, Zhiwei Shan, and Han Huang. The mechanical properties of nanowires. *Advanced Science*, 4(4):1600332, 2017.

[17] Soumen Kar, N. K. Kishore, V. Srinivas, Amitabha Ghoshray, and Bilwadal Bandyopadhyay. Effect of surface oxidation on magnetic and electrical properties of nc-ni particles. In *AIP Conference Proceedings*, volume 1003, pages 70–72. AIP, 2008.

[18] Kseniya Tsysar, Ekaterina Smelova, and Dmitry Bazhanov. Magneto-optical properties of oxidized co nanowires on pt substrate. *physica status solidi (b)*, 259(8):2200018, 2022.

[19] Oleksandr Pastukh, Dominika Kuźma, and Piotr Zieliński. Surface roughness effects on magnetic properties and switching mechanism in iron nanowires. *Crystals*, 13(12):1617, 2023.

[20] Xi Chen and R. H. Victora. Surface scattering in metallic nanowires. *Applied Physics Letters*, 93(16):162105, 2008.

[21] B.D. Cullity and C.D. Graham. *Introduction to Magnetic Materials*, chapter Chapter 13.3.1 Losses in Electrical Machines. John Wiley & Sons, Inc, second edition edition, 2009.

[22] K. Fuchs. The conductivity of thin metallic films according to the electron theory of metals. *Mathematical Proceedings of the Cambridge Philosophical Society*, 34(1):100–108, 1938.

[23] H. Sondheimer. The mean free path of electrons in metals. *Advances in Physics*, 1(1):1–42, 1952.

[24] T. M. Whitney, P. C. Searson, J. S. Jiang, and C. L. Chien. Fabrication and magnetic properties of arrays of metallic nanowires. *Science*, 261(5126):1316–1319, 1993.

[25] Yicong Chen and Bethanie J.H. Stadler. Predictions of optimal heating by magnetic reversal behavior of magnetic nanowires (MNWs) with different materials. *International Journal of Hyperthermia*, 40(1):2223371, 2023.

[26] Mariana P. Proenca, Javier Rial, Joao P. Araujo, and Celia T. Sousa. Magnetic reversal modes in cylindrical nanostructures: from disks to wires. *Scientific Reports*, 11(1):10100, 2021.

[27] L Sun and Y Hao. Tuning the properties of magnetic nanowires. *IBM Journal of Research and Development*, 49(1), 2005.

[28] R. Moreno, V.L. Carvalho-Santos, D. Altbir, and O. Chubykalo-Fesenko. Detailed examination of domain wall types, their widths and critical diameters in cylindrical magnetic nanowires. *Journal of Magnetism and Magnetic Materials*, 542:168495, 2022.

[29] V.R. Caffarena, A.P. Guimarães, W.S.D. Folly, E.M. Silva, and J.L. Capitaneo. Magnetic behavior of electrodeposited cobalt nanowires using different electrolytic bath acidities. *Materials Chemistry and Physics*, 107(2):297–304, 2008.

[30] Orhan Yalçın. *Chapter 1: Ferromagnetic Resonance*, pages 1–46. InTech, 2014.

[31] J. M. D. Coey. *Magnetism and Magnetic Materials*, chapter Magnetostatics. Cambridge University Press, 2009.

[32] Aurelian Rotaru, Jin-Hee Lim, Denny Lenormand, Andrei Diaconu, John. B. Wiley, Petronel Postolache, Alexandru Stancu, and Leonard Spinu. Interactions and reversal-field memory in complex magnetic nanowire arrays. *Physical Review B*, 84(13):134431, 2011.

[33] C.L. Chien, L. Sun., M. Tanase, L.A. Bauer, A. Hultgren, D.M. Silevitch, G.J. Meyer, P.C. Searson, and D. H. Reich. Electrodeposited magnetic nanowires: arrays, field-induced assembly, and surface functionalization. *Journal of Magnetism and Magnetic Materials*, 249(1):146–155, 2022.

[34] Sarah J. Hurst, Emma Kathryn Payne, Lidong Qin, and Chad A. Mirkin. Multisegmented one-dimensional nanorods prepared by hard-template synthetic methods. *Angewandte Chemie International Edition*, 45(17):2672–2692, 2006.

[35] Woo Lee and Sang-Joon Park. Porous anodic aluminum oxide: Anodization and templated synthesis of functional nanostructures. *Chemical Reviews*, 114(15):7487–7556, 2014.

[36] Boor Singh Lalia, Victor Kochkodan, Raed Hashaikeh, and Nidal Hilal. A review on membrane fabrication: Structure, properties and performance relationship. *Desalination*, 326:77–95, 2013.

[37] Anodic aluminum oxide, inredox, 2026.

[38] Masanobu Izaki. *Modern Electroplating*, chapter Electrodeposition of Iron and Iron Alloys, pages 309–326. Wiley, 1 edition, 2010.

[39] Jiaqi Shen, Paul T. Griffiths, Steven J. Campbell, Battist Utinger, Markus Kalberer, and Suzanne E. Paulson. Ascorbate oxidation by iron, copper and reactive oxygen species: review, model development, and derivation of key rate constants. *Scientific Reports*, 11(1):7417, 2021.

[40] P. Martinez and D. Uribe. Study of the complexes of the ascorbic acid-iron(III) system. *Zeitschrift für Naturforschung B*, 37(11):1446–1449, 1982.

[41] Alexander J. Grutter, Kathryn L. Krycka, Elena V. Tartakovskaya, Julie A. Borchers, K. Sai Madhukar Reddy, Eduardo Ortega, Arturo Ponce, and Bethanie J. H. Stadler. Complex three-dimensional magnetic ordering in segmented nanowire arrays. *ACS Nano*, 11(8):8311–8319, 2017.

[42] Joseph Um, Mohammad Reza Zamani Kouhpanji, Samuel Liu, Zohreh Nemati Porshokouh, Sang-Yeob Sung, Jurgen Kosel, and Bethanie Stadler. Fabrication of long-range ordered aluminum oxide and fe/au multilayered nanowires for 3-d magnetic memory. *IEEE Transactions on Magnetics*, 56(2):1–6, 2020.

[43] M Susano, M P Proenca, S Moraes, C T Sousa, and J P Araújo. Tuning the magnetic properties of multisegmented ni/cu electrodeposited nanowires with controllable ni lengths. *Nanotechnology*, 27(33):335301, 2016.

[44] D. A. Bograchev, T. B. Kabanova, and A. D. Davydov. Electrodeposition of metals into nano/micropores of templates: a type of electrochemistry under confinement (review). *Journal of Solid State Electrochemistry*, 29(4):1309–1340, 2025.

[45] Adrian Ghemes, Oana Dragos-Pinzaru, Horia Chiriac, Nicoleta Lupu, Marian Grigoras, Daniel Shore, Bethanie Stadler, and Ibro Tabakovic. Controlled electrodeposition and magnetic properties of co_{35} fe_{65} nanowires with high saturation magnetization. *Journal of The Electrochemical Society*, 164(2):D13–D22, 2017.

[46] Shweta Sharma, Prashant Shukla, Amit Misra, and Prabhat R. Mishra. Interfacial and colloidal properties of emulsified systems: Pharmaceutical and biological perspective. In *Colloid and Interface Science in Pharmaceutical Research and Development*, pages 149–168. Elesvier, 2014.

[47] Julian Eastoe, Martin J. Hollamby, and Laura Hudson. Recent advances in nanoparticle synthesis with reversed micelles. *Advances in Colloid and Interface Science*, 128-130:5–15, 2006.

[48] Maria Velinova, Durba Sengupta, Alia V. Tadjer, and Siewert-Jan Marrink. Sphere-to-rod transitions of nonionic surfactant micelles in aqueous solution modeled by molecular dynamics simulations. *Langmuir*, 27(23):14071–14077, 2011.

[49] Joseph I. Goldstein, Dale E. Newbury, Patrick Echlin, David C. Joy, Charles E. Lyman, Eric Lifshin, Linda Sawyer, and Joesph R. Michael. *Scanning Electron Microscopy and X-Ray Microanalysis.* Plenum Press, 3rd edition, 2003.

[50] Dale E. Newbury and Nicholas W. M. Ritchie. Performing elemental microanalysis with high accuracy and high precision by scanning electron microscopy/silicon drift detector energy-dispersive x-ray spectrometry (SEM/SDD-EDS). *Journal of Materials Science*, 50(2):493–518, 2015.

[51] Katherine E. MacArthur, Andrew B. Yankovich, Armand Béché, Martina Luysberg, Hamish G. Brown, Scott D. Findlay, Marc Heggen, and Leslie J. Allen. Optimizing experimental conditions for accurate quantitative energy-dispersive x-ray analysis of interfaces at the atomic scale. *Microscopy and Microanalysis*, 27(3):528–542, 2021.

[52] B. D. Cullity. *Elements of X-Ray Diffraction.* Addison-Wesley Publishing Company, 2nd edition, 1978.

[53] P. Scherrer. Bestimmung der grösse und der inneren struktur von kolloidteilchen mittels röntgenstrahlen. *Nachr. Ges. Wiss.*, pages 98–100, 1918.

[54] J. I. Langford and A.J.C. Wilson. Scherrer after sixty years: A survey and some new results in the determination of crystallite size. *Journal of Applied Crystallography*, 11:102–113, 1978.

[55] Lawrence H. Bennett and Edward Della Torre. Analysis of wasp-waist hysteresis loops. *Journal of Applied Physics*, 97(10):10E502, 2005.

[56] Sergiu Ruta, Ondrej Hovorka, Pin-Wei Huang, Kangkang Wang, Ganping Ju, and Roy Chantrell. First order reversal curves and intrinsic parameter determination for magnetic materials; limitations of hysteron-based approaches in correlated systems. *Scientific Reports*, 7(1):45218, 2017.

[57] Costin-Ionut Dobrota and Alexandru Stancu. Tracking the individual magnetic wires' switchings in ferromagnetic nanowire arrays using the first-order reversal curves (FORC) diagram method. *Physica B: Condensed Matter*, 457:280–286, 2015.

[58] Bethanie J. H. Stadler, Mohammad Reza Zamani Kouhpanji, and Andrzej Stankiewicz. Irreversible and reversible switching in nanomagnet arrays and hard drive media. *IEEE Transactions on Magnetics*, 59(3):1–4, 2023.

[59] Jeffrey P. Gambino, Shawn A. Adderly, and John U. Knickerbocker. An overview of through-silicon-via technology and manufacturing challenges. *Microelectronic Engineering*, 135:73–106, 2015.

[60] Makoto Motoyoshi. Through-silicon via (TSV). *Proceedings of the IEEE*, 97(1):43–48, 2009.

[61] Wen-Wei Shen and Kuan-Neng Chen. Three-dimensional integrated circuit (3d IC) key technology: Through-silicon via (TSV). *Nanoscale Research Letters*, 12(1):56, 2017.

[62] Simone Frasca, Rebecca C. Leghziel, Ivo N. Arabadzhiev, Benoît Pasquier, Grégoire F. M. Tomassi, Sandro Carrara, and Edoardo Charbon. The michelangelo step: removing scalloping and tapering effects in high aspect ratio through silicon vias. *Scientific Reports*, 11(1):3997, 2021.

[63] Hideki Masuda and Kenji Fukuda. Ordered metal nanohole arrays made by a two-step replication of honeycomb structures of anodic alumina. *Science*, 268(5216):1466–1468, 1995.

[64] Woo Lee, Ran Ji, Ulrich Gösele, and Kornelius Nielsch. Fast fabrication of long-range ordered porous alumina membranes by hard anodization. *Nature Materials*, 5(9):741–747, 2006.

[65] Yang Yang, Huilan Chen, Yongfeng Mei, Jianbin Chen, Xinglong Wu, and Ximao Bao. Anodic alumina template on au/si substrate and preparation of CdS nanowires. *Solid State Communications*, 123(6):279–282, 2002.

[66] Nicolas E. Holubowitch, Lorraine C. Nagle, and James F. Rohan. Porous alumina thin films on conductive substrates for templated 1-dimensional nanostructuring. *Solid State Ionics*, 216:110–113, 2012.

[67] Joseph Um, Bethanie J.H. Stadler, Rhonda Franklin, Yali Zhang, and Rashaunda Henderson. Adhesion layer for forming nanowires in anodic aluminum oxide.

[68] Yali Zhang, Joseph Um, Bethanie Stadler, Rashaunda Henderson, and Rhonda Franklin. Study of nanowire-based integrated via technology for CMOS application in millimeter-wave frequencies. *IEEE Microwave and Wireless Components Letters*, 31(6):693–696, 2021.

[69] Standard test methods for rating adhesion by tape test.

[70] Caroline A Schneider, Wayne S Rasband, and Kevin W Eliceiri. NIH image to ImageJ: 25 years of image analysis. *Nature Methods*, 9(7):671–675, 2012.

[71] Joseph Um. *Template-Assisted Electrodeposited Nanowires and Their Applications.* Doctor of philosophy, Univeristy of Minnesota - Twin Cities, 2021.

[72] M. J. Donahue and D.J. Porter. *OOMMF user's guide.*

[73] Daniel Gall. Electron mean free path in elemental metals. *Journal of Applied Physics*, 119(8):085101, 2016.

[74] Shao-Kuan Lee, Hsiu-Ching Hsu, and Wei-Hsing Tuan. Oxidation behavior of copper at a temperature below 300 °c and the methodology for passivation. *Materials Research*, 19(1):51–56, 2016.

[75] B.D. Cullity and C.D Graham. *Introduction to Magnetic Materials*, chapter Magnetic Resonance. John Wiley & Sons, Inc, second edition, 2009.

[76] A. Encinas-Oropesa, M. Demand, L. Piraux, I. Huynen, and U. Ebels. Dipolar interactions in arrays of nickel nanowires studied by ferromagnetic resonance. *Physical Review B*, 63(10):104415, 2001.

[77] G. Goglio, S. Pignard, A. Radulescu, L. Piraux, I. Huynen, D. Vanhoenacker, and A. Vander Vorst. Microwave properties of metallic nanowires. *Applied Physics Letters*, 75(12):1769–1771, 1999.

[78] Joseph Um, Yali Zhang, Wen Zhou, Mohammad R. Zamani Kouhpanji, Cosmin Radu, Rhonda R. Franklin, and Bethanie J. H. Stadler. Magnetic nanowire biolabels using ferromagnetic resonance identification. *ACS Applied Nano Materials*, 4(4):3557–3564, 2021.

[79] Manish Sharma, Sachin Pathak, and Monika Sharma. *Ferromagnetic Resonance - Theory and Applications*, chapter Chapter 4: FMR Measurements of Magnetic Nanostructures. InTech, 2013.

[80] Justin M. Shaw, Hans T. Nembach, T. J. Silva, and Carl T. Boone. Precise determination of the spectroscopic g -factor by use of broadband ferromagnetic resonance spectroscopy. *Journal of Applied Physics*, 114(24):243906, 2013.

[81] I. Dumitru, Feng Li, J.B. Wiley, D. Cimpoesu, A. Stancu, and L. Spinu. Study of magnetic interactions in metallic nanowire networks. *IEEE Transactions on Magnetics*, 41(10):3361–3363, 2005.

[82] G. Kartopu, O. Yalçın, S. Kazan, and B. Aktaş. Preparation and FMR analysis of co nanowires in alumina templates. *Journal of Magnetism and Magnetic Materials*, 321(9):1142–1147, 2009.

[83] O.C. Trusca, D. Cimpoesu, Jin-Hee Lim, Xiequn Zhang, J.B. Wiley, A. Diaconu, I. Dumitru, A. Stancu, and L. Spinu. Interaction effects in ni nanowire arrays. *IEEE Transactions on Magnetics*, 44(11):2730–2733, 2008.

[84] B. Ye, F. Li, D. Cimpoesu, J.B. Wiley, J.-S. Jung, A. Stancu, and L. Spinu. Passive high-frequency devices based on superlattice ferromagnetic nanowires. *Journal of Magnetism and Magnetic Materials*, 316(2):e56–e58, 2007.

[85] M Demand, A Encinas-Oropesa, S Kenane, U Ebels, I Huynen, and L Piraux. Ferromagnetic resonance studies of nickel and permalloy nanowire arrays. *Journal of Magnetism and Magnetic Materials*, 249(1):228–233, 2002.

[86] Yuxiong Lei, Liangliang Li, Lixin Yuan, and Zhenxing Yue. Tunable high-frequency properties of co–ni ferromagnetic nanowires through composition modulation. *IEEE Transactions on Magnetics*, 51(11):1–6, 2015.

[87] Monika Sharma and Bijoy K Kuanr. Microwave devices based on template-assisted NiFe nanowires: fabrication and characterization. *Journal of Physics D: Applied Physics*, 53(6):065001, 2020.

[88] Sangita S. Kalarickal, Pavol Krivosik, Mingzhong Wu, Carl E. Patton, Michael L. Schneider, Pavel Kabos, T. J. Silva, and John P. Nibarger. Ferromagnetic resonance linewidth in metallic thin films: Comparison of measurement methods. *Journal of Applied Physics*, 99(9):093909, 2006.

[89] Yali Zhang, Joseph Um, Wen Zhou, Bethanie Stadler, and Rhonda Franklin. Magnetic nanowires for RF applications: Ferromagnetic resonance and permeability characterization. In *2019 IEEE MTT-S International Microwave Symposium (IMS)*, pages 1100–1103. IEEE, 2019.

[90] Wen Zhou, Joseph Um, Bethanie Stadler, and Rhonda Franklin. Design of self-biased coplanar circulator with ferromagnetic nanowires. In *2018 IEEE Radio and Wireless Symposium (RWS)*, pages 240–242. IEEE, 2018.

[91] Richard J. Harrison and Joshua M. Feinberg. FORCinel: An improved algorithm for calculating first-order reversal curve distributions using locally weighted regression smoothing. *Geochemistry Geophysics Geosystems*, 9(5), 2008.

[92] Antanas Vaitkus, Andrius Merkys, and Saulius Gražulis. Validation of the crystallography open database using the crystallographic information framework. *Journal of Applied Crystallography*, 54(2):661–672, 2021.

[93] U. Erb. Corrosion behavior of electrodeposited nanocrystals. In *Uhlig's Corrosion Handbook*, pages 517–528. John Wiley & Sons, Inc, third edition edition, 2011.

[94] Costin-Ionuţ Dobrotă and Alexandru Stancu. What does a first-order reversal curve diagram really mean? a study case: Array of ferromagnetic nanowires. *Journal of Applied Physics*, 113(4):043928, 2013.

[95] Mohammad Reza Zamani Kouhpanji, P.B. Visscher, and Bethanie J.H. Stadler. Fast and universal approach for quantitative measurements of bistable hysteretic systems. *Journal of Magnetism and Magnetic Materials*, 537:168170, 2021.

[96] Dustin A. Gilbert, Peyton D. Murray, Julius De Rojas, Randy K. Dumas, Joseph E. Davies, and Kai Liu. Reconstructing phase-resolved hysteresis loops from first-order reversal curves. *Scientific Reports*, 11(1):4018, 2021.

[97] Xuetian Ma, Adelaide M. Nolan, Shuo Zhang, Jianming Bai, Wenqian Xu, Lijun Wu, Yifei Mo, and Hailong Chen. Guiding synthesis of polymorphs of materials using nanometric phase diagrams. *Journal of the American Chemical Society*, 140(49):17290–17296, 2018.

[98] Michaël Darques, Armando Encinas, Laurent Vila, and Luc Piraux. Controlled changes in the microstructure and magnetic anisotropy in arrays of electrodeposited co nanowires induced by the solution pH. *Journal of Physics D: Applied Physics*, 37(10):1411–1416, 2004.

[99] Jedediah K. Lewis, John C. Bischof, Ido Braslavsky, Kelvin G.M. Brockbank, Gregory M. Fahy, Barry J. Fuller, Yoed Rabin, Alessandro Tocchio, Erik J. Woods, Brian G. Wowk, Jason P. Acker, and Sebastian Giwa. The grand challenges

of organ banking: Proceedings from the first global summit on complex tissue cryopreservation. *Cryobiology*, 72(2):169–182, 2016.

[100] W. F. Rall and G. M. Fahy. Ice-free cryopreservation of mouse embryos at 196 °c by vitrification. *Nature*, 313(6003):573–575, 1985.

[101] Kelvin G. M. Brockbank, Zhenzhen Chen, Elizabeth D. Greene, and Lia H. Campbell. Vitrification of heart valve tissues. In Willem F. Wolkers and Harriëtte Oldenhof, editors, *Cryopreservation and Freeze-Drying Protocols*, volume 1257, pages 399–421. Springer New York, 2015. Series Title: Methods in Molecular Biology.

[102] Li Zhan, Joseph Sushil Rao, Nikhil Sethia, Michael Q. Slama, Zonghu Han, Diane Tobolt, Michael Etheridge, Quinn P. Peterson, Cari S. Dutcher, John C. Bischof, and Erik B. Finger. Pancreatic islet cryopreservation by vitrification achieves high viability, function, recovery and clinical scalability for transplantation. *Nature Medicine*, 28(4):798–808, 2022.

[103] Srivasupradha Ramesh, Joseph Sushil Rao, Bat-Erdene Namsrai, Benjamin Fisher, Diane K. Tobolt, Michael Megaly, Michael L. Etheridge, Timothy L. Pruett, Davis Seelig, Paari Murugan, Bashar Aldaraiseh, Erik B. Finger, and John C. Bischof. Vitrification and rapid rewarming of precision-cut liver slices for pharmacological and biomedical research.

[104] Jonathan Daly, Nikolas Zuchowicz, C. Isabel Nuñez Lendo, Kanav Khosla, Claire Lager, E. Michael Henley, John Bischof, F. W. Kleinhans, Chiahsin Lin, Esther C. Peters, and Mary Hagedorn. Successful cryopreservation of coral larvae using vitrification and laser warming. *Scientific Reports*, 8(1):15714, 2018.

[105] Lakshya Gangwar, Zonghu Han, Cameron Scheithauer, Bat-Erdene Namsrai, Saurin Kantesaria, Rob Goldstein, Michael L. Etheridge, Erik B. Finger, and John C. Bischof. Physical vitrification and nanowarming at liter-scale CPA volumes: toward organ cryopreservation. *Nature Communications*, 16(1):8511, 2025.

[106] Z. Han, L. Gangwar, E. Magnuson, M.L. Etheridge, C.O. Pringle, J.C. Bischof, and J. Choi. Supplemented phase diagrams for vitrification CPA cocktails: DP6, VS55 and m22. *Cryobiology*, 106:113–121, 2022.

[107] Zonghu Han and John C Bischof. CRITICAL COOLING AND WARMING RATES AS a FUNCTION OF CPA CONCENTRATION. *Cryo Letters*, 2023.

[108] Nima Ahmadkhani, James D. Benson, Ali Eroglu, and Adam Z. Higgins. High throughput method for simultaneous screening of membrane permeability and toxicity for discovery of new cryoprotective agents. *Scientific Reports*, 15(1):1862, 2025.

[109] Justyna J Jaskiewicz, Abby Callahan-Muller, Nora Gaby-Biegel, Zachary Glover, and Rebecca D Sandlin. Validation of a high-throughput screening assay for the characterization of cryoprotective agent toxicity. *preprint*, 2025.

[110] Navid Manuchehrabadi, Zhe Gao, Jinjin Zhang, Hattie L. Ring, Qi Shao, Feng Liu, Michael McDermott, Alex Fok, Yoed Rabin, Kelvin G. M. Brockbank, Michael Garwood, Christy L. Haynes, and John C. Bischof. Improved tissue cryopreservation using inductive heating of magnetic nanoparticles. *Science Translational Medicine*, 9(379):eaah4586, 2017.

[111] Liselotte Jauffred, Akbar Samadi, Henrik Klingberg, Poul Martin Bendix, and Lene B. Oddershede. Plasmonic heating of nanostructures. *Chemical Reviews*, 119(13):8087–8130, 2019.

[112] Li Zhan, Shuang-Zhuang Guo, Joseph Kangas, Qi Shao, Maple Shiao, Kanav Khosla, Walter C. Low, Michael C. McAlpine, and John Bischof. Conduction cooling and plasmonic heating dramatically increase droplet vitrification volumes for cell cryopreservation. *Advanced Science*, 8(11):2004605, 2021.

[113] R.E. Rosensweig. Heating magnetic fluid with alternating magnetic field. *Journal of Magnetism and Magnetic Materials*, 252:370–374, 2002.

[114] Peter Debye. *Polar Molecules.* The Chemical Catalouge Company, 1929.

[115] Louis Néel. Théorie du traînage magnétique des ferromagnétiques en grains fins avec application aux terres cuites. *Annales de géophysique*, 5:99–136, 1949.

[116] Anirudh Sharma, Charles Y. Lee, Bat-Erdene Namsrai, Zonghu Han, Diane Tobolt, Joseph Sushil Rao, Zhe Gao, Michael L. Etheridge, Michael Garwood,

Mark G. Clemens, John C. Bischof, and Erik B. Finger. Cryopreservation of whole rat livers by vitrification and nanowarming. *Annals of Biomedical Engineering*, 51(3):566–577, 2023.

[117] Zonghu Han, Joseph Sushil Rao, Lakshya Gangwar, Bat-Erdene Namsrai, Jacqueline L. Pasek-Allen, Michael L. Etheridge, Susan M. Wolf, Timothy L. Pruett, John C. Bischof, and Erik B. Finger. Vitrification and nanowarming enable long-term organ cryopreservation and life-sustaining kidney transplantation in a rat model. *Nature Communications*, 14(1):3407, 2023.

[118] Paul L. McCormack. Ferumoxytol: In iron deficiency anaemia in adults with chronic kidney disease. *Drugs*, 72(15):2013–2022, 2012.

[119] Daniel Shore, Adrian Ghemes, Oana Dragos-Pinzaru, Zhe Gao, Qi Shao, Anirudh Sharma, Joseph Um, Ibro Tabakovic, John C. Bischof, and Bethanie J. H. Stadler. Nanowarming using au-tipped co $_{35}$ fe $_{65}$ ferromagnetic nanowires. *Nanoscale*, 11(31):14607–14615, 2019.

[120] Tharwat Tadros. *Steric Stabilization*, pages 1048–1049. Springer, Berlin, Heidelberg, 2013.

[121] Kim E. Sapsford, Katherine M. Tyner, Benita J. Dair, Jeffrey R. Deschamps, and Igor L. Medintz. Analyzing nanomaterial bioconjugates: A review of current and emerging purification and characterization techniques. *Analytical Chemistry*, 83(12):4453–4488, 2011.

[122] Jessica Rodríguez-Fernández, Jorge PérezJuste, Luis M. LizMarzán, and Peter R. Lang. Dynamic light scattering of short au rods with low aspect ratios. *The Journal of Physical Chemistry C*, 111(13):5020–5025, 2007.

[123] Measuring zeta potential - laser doppler electrophoresis explained, 2015. Technical Note.

[124] Robert J. Hunter. *Zeta Potential in Colloid Science*. Academic Press, 1 edition, 1981.

[125] Jacqueline L. Pasek-Allen, Randall K. Wilharm, Zhe Gao, Valerie C. Pierre, and John C. Bischof. Phosphonate coating of commercial iron oxide nanoparticles for nanowarming cryopreserved samples. *Journal of Materials Chemistry B*, 10(19):3734–3746, 2022.

[126] Ming Li and Jonathan A. Brant. Dispersing surface-modified imogolite nanotubes in polar and non-polar solvents. *Journal of Nanoparticle Research*, 20(2):19, 2018.

[127] C.J. Brinker and G.W. Scherer. *Sol-gel Science: The Physics and Chemistry of Sol-gel Processing*. Gulf Professional Publishing, 1990.

[128] Henry N Po and N M Senozan. The henderson–hasselbalch equation: Its history and limitations. *Journal of Chemical Education*, 78(11), 2001.

[129] Feng Wang and Xiaogang Liu. Upconversion multicolor fine-tuning: Visible to near-infrared emission from lanthanide-doped $NaYF_4$ nanoparticles. *Journal of the American Chemical Society*, 130(17):5642–5643, 2008.

[130] V. N. Kislenko and L. P. Oliynyk. Complex formation of polyethyleneimine with copper(II), nickel(II), and cobalt(II) ions. *Journal of Polymer Science Part A: Polymer Chemistry*, 40(7):914–922, 2002.

[131] Ha-Young Lee, Sang-Hoon Lee, Chenjie Xu, Jin Xie, Jin-Hyung Lee, Bing Wu, Ai Leen Koh, Xiaoying Wang, Robert Sinclair, Shan X Wang, Dwight G Nishimura, Sandip Biswal, Shouheng Sun, Sun Hang Cho, and Xiaoyuan Chen. Synthesis and characterization of PVP-coated large core iron oxide nanoparticles as an MRI contrast agent. *Nanotechnology*, 19(16):165101, 2008.

[132] Francisco N. Souza Neto, Leonardo A. Morais, Luiz F. Gorup, Lucas S. Ribeiro, Tassia J. Martins, Thayse Y. Hosida, Patricia Francatto, Debora B. Barbosa, Emerson R. Camargo, and Alberto C. B. Delbem. Facile synthesis of PVP-coated silver nanoparticles and evaluation of their physicochemical, antimicrobial and toxic activity. *Colloids and Interfaces*, 7(4):66, 2023.

[133] Mandeep Singh, Manish Kumar, Frantisek Stipanek, Pavel Ulbrich, Pavel Svoboda, Eva Santava, and M.L. Singla. Liquid-phase synthesis of nickel nanoparticles stabilized by PVP and study of their structural and magnetic properties. *Advanced Materials Letters*, 2(6):409–414, 2011.

[134] Andrea Rónavári, Péter Bélteky, Eszter Boka, Dalma Zakupszky, Nóra Igaz, Bettina Szerencsés, Ilona Pfeiffer, Zoltán Kónya, and Mónika Kiricsi. Polyvinyl-pyrrolidone-coated silver nanoparticles—the colloidal, chemical, and biological consequences of steric stabilization under biorelevant conditions. *International Journal of Molecular Sciences*, 22(16):8673, 2021.

[135] Inactive ingredient search for approved drug products, povidone.

[136] Inactive ingredient search for approved drug products, polyethylene glycol.

[137] Zhonghui Chen, Ziyu Lv, Yifeng Sun, Zhenguo Chi, and Guangyan Qing. Recent advancements in polyethyleneimine-based materials and their biomedical, biotechnology, and biomaterial applications. *Journal of Materials Chemistry B*, 8(15):2951–2973, 2020.

[138] Yu-Kuan An. Simple method to measure the refractive index of liquid with graduated cylinder and beaker. *Review of Scientific Instruments*, 88(12):125105, 2017.

[139] Lakshya Gangwar, Yicheng Jiang, Dametre Thunberg, Cameron Scheithauer, Michael L. Etheridge, John C. Bischof, and Rhonda R. Franklin. Dielectric properties of individual cryoprotective agents and cocktails VS55, m22, DP6 at subzero temperatures for cryopreservation. *Scientific Reports*, 15(1):20734, 2025.

[140] Chongbo Sun, Tian Tang, Hasan Uludağ, and Javier E. Cuervo. Molecular dynamics simulations of DNA/PEI complexes: Effect of PEI branching and protonation state. *Biophysical Journal*, 100(11):2754–2763, 2011.

[141] Caleb E. Gallops, Chang Yu, Jesse D. Ziebarth, and Yongmei Wang. Effect of the protonation level and ionic strength on the structure of linear polyethyleneimine. *ACS Omega*, 4(4):7255–7264, 2019.

Appendix A

Acronyms

Care has been taken in this thesis to minimize the use of acronyms, but this cannot always be achieved. This appendix contains a table of acronyms and their meaning.

A.1 Acronyms

Table A.1: Acronyms

Acronym	Meaning
AA	Ascorbic Acid
AAO	Anodized Aluminum Oxide
AMF	Alternating Magnetic Field
BSE	Back-Scattered Electron
CPA	Cryo-Protective Agent
DI	De-Ionized
DLS	Dynamic Light Scattering
EDX or EDS	Energy-Dispersive X-Ray Spectroscopy
EG	Ethylene Glycol
FCC	Face-Centered Cubic
FF	Fill Factor

Continued on next page

Table A.1 – continued from previous page

Acronym	Meaning
FORC(s)	First-Order Reversal Curve(s)
FMR	Ferromagnetic Resonance
HCP	Hexagonal Close Packed
IP	In-Plane
MA	Malonic Acid
MNW(s)	Magnetic Nanowire(s)
MW	Molecular Weight
OP	Out-of-Plane
PG	Propylene Glycol
PZC	Point of Zero Charge
RF	Radio Frequency
SDS	Sodium Docecyl Sulfate
SE	Secondary Electron
VNA	Vector Network Analyzer
VSM	Vibrating Sample Magnetometer
XRD	X-Ray Diffraction

Appendix B

Standard Procedure for Etching AAO Templates

This is the standard procedure used to etch AAO templates and free magnetic nanowires from the template.

Written: 5/13/2025 (Alli Harpel)
Last Updated: 5/14/2025
Adapted from: Joseph Um

B.1 Safety Guidelines

Standard procedures for Acid/Base safety. Make sure to dispose of the acids and bases in hazardous waste.

B.2 Equipment and Materials

Equipment

- Ultrasonicator
- Magnetic Stand
- Micropipettes

Materials

- Clean, [1] NaOH
- DI Water
- Pipette Tips
- Microcentrifuge tubes

B.3 Sample Needs

Samples must be magnetic nanowires in templated anodized aluminum oxide. The samples must have the copper back contact completely etched (or as much as feasible), and must be clean and free from any adhesive or vacuum grease that may be on the surface after fabrication and/or characterization. Note that a maximum of 6 microcentrifuge tubes can sit on the magnetic stand to collect at a time, so keep that in mind when designing your experiments.

B.4 Procedure

1. Ensure that AAO template has the copper contact completely etched and that the template has been cleaned of all adhesive or vacuum grease. (Use a kimwipe and acetone, then kimwipe and isopropyl alcohol to clean the templates before etching)
2. Place AAO Template in a microcentrifuge tube. Typically only about half will fit in at a time, so you might need to break it a bit.
3. Place on magnetic stand.
4. Break template into tiny fragments by grinding with tweezers.
5. Add 750 μL [1] NaOH (use micropipette)
6. Sonicate for 15 min. at $\approx 35^o C$

   Note: During all sonication steps, move the float once or twice with tweezers

Sonication Settings Frequency: 37 kHz (or nearest available), Power: 100 %, Mode: Sweep

7. Let sit in warm bath for about a half hour.
8. Check nanowires, tapping the tubes so that the clump at the bottom disperses once more.
9. Repeat steps 6-8 until mostly dissolved.

   Note: Ni will only take $\tilde{1}$ hour, but for the Fe NWs I've been having it take ¿ 24 hours sometimes. In those cases, slowly add in 10 w% NaOH solution dropwise if it is taking more than 6 hours.

10. Remove from bath, and let sit on magnetic stand to collect for 40-60 min (60 recommended)
11. Remove 700 μL of the NaOH, take care not to pick up NWs as well
12. Add 700 μL of DI Water
13. Sonicate for 15 min
14. Place on magnetic stand to collect for 40-60 min,
15. Remove water/NaOH (as much as possible, but take care not to pick up NWs as well) before adding your desired solvent. Agitate or sonicate to disperse

    Note: For storage, ethanol or propylene glycol work well as a solvent if you don't have anything specific you need to suspend the wires in immediately.

Appendix C

Code for Resistivity Estimate

```
%%%%%%%%%%%%%%%%%%%%%%%%%%%%%%%%%%%%%%%%%%%%
%DC_Resistance_Area.m
%
%Inputs: - Average System Resistance
% -File containing resistance measurements (in Ohms) and Area measurements (in nm^2)
%
%Outputs: -Raw Resistance Histogram
% -Raw and Fitted Histograms for Area Measured and Computed from Resistance
% -Estimated resistivity of the nanowires from fitting the mean measured and computed resistance with resistivity as the fit parameter.
%
%Written by Allison Harpel
%Last Edited: 01/21/2021
%%%%%%%%%%%%%%%%%%%%%%%%%%%%%%%%%%%%%%%%%%%%
clc
clear variables
close all
%Input Information %%%%%%%%%%%%%%%%%%%
Rsys=2.5; %Average DC resistance of system in ohms
L=1030; %Length of template/wires in nm
```

```
%Filename of spreadsheet containing resistance and area information
Filename=’CuResistance_ 20 nm _113021_forprocessing’;
%%%%%%%%%%%%%%%%%%%%%%%%%%%%%%%%%%%
%Read file and put into matrix form, separating out resistance and area
R=readmatrix(Filename,”sheet”,’DC’); %Resistance
PA=readmatrix(Filename,”sheet”,’Pore’);
PA=PA(:,2); %Pore Area
[n m]=size(R);
R=R(1:n,1)-Rsys; %Subtract out average system resistance
Ro=R;
%Loop to remove resistances under 100 ohms. These are probably 3+ nanowires
%and skew the data significantly if left in.
for i=1:n
if R(i,1)¡100
R(i,1)=NaN;
end
end
%Remove skewing area (points over 1000 Ohms above the rest)
p=length(PA);
for i=1:p
if PA(i,1)¿3500
PA(i,1)=NaN;
end
end
%Calculate the Area from Resistance; Assumes constant resistivity
rhoA=35$*(10^{-6})$; % in ohm-cm, initial guess resistivity
%FIT PARAMETER for AREA
CalcA=$(10^7*L*rhoA)./R$; %nm$^2$ calculated area
%Fit normal distributions to each
CalcAfit=fitdist(CalcA,’normal’);
MeasAfit=fitdist(PA,’normal’);
%establish tolerance values for when the means are considered matching up
```

```
tol=0.1;
param=abs(CalcAfit.mu-MeasAfit.mu);
%Fit the histograms, recalculate the calculated area fit with new rhoA %until
while param > tol
if CalcAfit.mu > MeasAfit.mu
rhoA=rhoA-(0.01*(10^(-6)));
elseif CalcAfit.mu < MeasAfit.mu
rhoA=rhoA+(0.005*(10^(-6)));
end
CalcA=(10^7*L*rhoA)./R; %nm^2
CalcAfit=fitdist(CalcA,'normal');
param=abs(CalcAfit.mu-MeasAfit.mu);
end
%Result Reporting %%%%%%%%%%%%%%%%%%
fprintf('Fitted resistivity: %3.2s micro-Ohms-cm.\n',rhoA)
fprintf('Normal curve parameters, Calculated Area: mean %3.2f stdev. %3.2 nm^2. \n',CalcAfit.mu,CalcAfit.sigma)
fprintf('Normal curve parameters, Measured Area: mean %3.2f stdev. %3.2f nm^2. \n',MeasAfit.mu,MeasAfit.sigma)
%
%Plot and fit the Measured Area
figure
histogram(PA,'BinWidth',100,'BinLimits',[0,2500]);
xlabel('Area (nm^2)')
title('Measured Area')
figure
histfit(PA',20,'normal');
xlabel('Area (nm^2)');
title('Measured Area');
axis([-100,2000,0,60]);
%
%Plot and Fit the Calc Area
```

```
figure
histogram(CalcA','BinWidth',100,'BinLimits',[0,2500]);
xlabel('Area (nm^2)')
title('Calculated Area')
figure
histfit(CalcA,20,'normal');
xlabel('Area (nm^2)');
title('Calculated Area');
axis([-100,2000,0,60]);
%
%plot Raw Resistance
figure
histogram(Ro,'BinWidth',20,'BinLimits',[0,1000]);
xlabel('R (ohms)');
title('Raw Resistance Histogram')
```

Appendix D

Error Propagation Sample Calculation

Uncertainty calculation was used to determine which variables where contributing most to the error in the resistivity estimate in each estimation. Resistivity was calculated using Eq. D.1, where A is the mean area from the area fit, R is the mean resistance, and l is the length of the wires as measured by the length of the template. This computation assumes that resistivity is constant for the material. However, it must be considered when analyzing the data that this is likely not so for all the nanowires measured, as at small size scales resistivity increases as discussed in preliminary results.

$$\rho = A \cdot R/l \tag{D.1}$$

The linear form of uncertainty propagation was used, as shown in Eq. D.2. where S_ρ, s_A, s_R, and S_l are the errors for resistivity, area, resistance, and length respectively. Computations of the partial derivatives and substitution into Eq. D.2 are shown in Eqs. D.3-D.6. Note that the first, second, and third terms under the root (before the square is taken) are measures of the uncertainty contribution of area, resistance, and length measurements to the resistivity uncertainty. Once the values shown in Table 3.3 are input into Eq. D.6, the results summarized in table 3.4 were obtained. These are the uncertainty contributions discussed in Section 3.3.3.

$$s_\rho = \sqrt{(s_A \partial\rho/\partial A)^2 + (s_R \partial\rho/\partial R)^2 + (s_l \partial\rho/\partial l)^2} \tag{D.2}$$

$$\partial\rho/\partial A = \partial(A \cdot R/l)/\partial A = R/l \tag{D.3}$$

$$\partial\rho/\partial A = \partial(A \cdot R/l)/\partial R = A/l \tag{D.4}$$

$$\partial\rho/\partial l = \partial(A \cdot R/l)/\partial l = -A \cdot R/l^2 \tag{D.5}$$

$$s_\rho = \sqrt{(s_A \cdot R/l)^2 + (s_R \cdot A/l)^2 + (s_l \cdot -AR/l^2)^2} \tag{D.6}$$

Some observations to note are that area and most importantly resistivity are the greatest contributors to the uncertainty, which matches expectations. The length term was one to two orders of magnitude smaller than either resistance or error uncertainty contributions. The decrease in resistance contribution from 1x to 2x anodization methods is likely due to the smaller average area to length ratio found in the partial derivative term, because the resistance and error in resistance was similar between the two samples. This indicates in future studies, smaller diameter or longer nanowires may reduce this term. Additional considerations with attempting to reduce resistance error are in being able to filter out when more than one nanowire is being measured in parallel, as discussed in preliminary results. The reduction in uncertainty in the area term from the 1x to 2x anodization is mostly due to the four-fold decrease in the area uncertainty value in the area between methods.